LOW VOLTAGE BLUE PHASE LIQUID CRYSTAL DISPLAYS

by

LINGHUI RAO
B.S. Huazhong University of Science and Technology, 2007
M.S. University of Central Florida, 2010

A dissertation submitted in partial fulfillment of the requirements
for the degree of Doctor of Philosophy
in the College of Optics and Photonics
at the University of Central Florida
Orlando, Florida

Summer Term
2012

Major Professor: Shin-Tson Wu

ABSTRACT

From cell phones, laptops, desktops, TVs, to projectors, high reliability LCDs have become indispensable in our daily life. Tremendous progress in liquid crystal displays (LCDs) has been made after decades of extensive research and development in materials, device configurations and manufacturing technology.

Nowadays, the most critical issue on viewing angle has been solved using multidomain structures and optical film compensation. Slow response time has been improved to 2-5 ms with low viscosity LC material, overdrive and undershoot voltage, and thin cell gap approach. Moving image blur has been significantly reduced by impulse driving and frame insertion. Contrast ratio in excess of one million-to-1 has been achieved through local dimming of the segmented LED backlight. The color gamut would exceed 100% of the NTSC (National Television System Committee), if RGB LEDs are used. Besides these technological advances, the cost has been reduced dramatically by investing in advanced manufacturing technologies.

Polymer-stabilized blue phase liquid crystal displays (BPLCDs) based on Kerr effect is emerging as a potential next-generation display technology. In comparison to conventional nematic devices, the polymer-stabilized BPLCDs exhibit following attractive features: (1) submillisecond response time, (2) no need for molecular alignment layers, (3) optically isotropic dark state when sandwiched between crossed polarizers, and (4) transmittance is insensitive to cell gap when the in-plane electrodes are employed.

However, aside from these great potentials, there are still some tough technical issues remain to be addressed. The major challenges are: 1) the operating voltage is still too high (~50 Volts vs. 5 Volts for conventional nematic LCDs), and the transmittance is relatively low (~65%

vs. 85% for nematic LCDs), 2) the hysteresis effect and residual birefringence effect are still noticeable, 3) the mesogenic temperature range is still not wide enough for practical applications (–40 ^{o}C to 80 ^{o}C), and 4) the ionic impurities in these polymer-stabilized nano-structured LC composites could degrade the voltage holding ratio, which causes image sticking.

In this dissertation, the BPLC materials are studied and the new BPLC device structures are designed to optimize display performances.

From material aspect, the electro-optical properties of blue phase liquid crystals are studied based on Kerr effect. Temperature effects on polymer-stabilized blue phase or optically isotropic liquid crystal displays are investigated through the measurement of voltage dependent transmittance under different temperatures. The physical models for the temperature dependency of Kerr constant, induced birefringence and response time in BPLCs are first proposed and experimentally validated. In addition, we have demonstrated a polymer-stabilized BPLC mixture with a large Kerr constant K~13.7 nm/V^2 at 20 ^{o}C and λ=633 nm. These models would set useful guidelines for optimizing material performances.

From devices side, the basic operation principle of blue phase LCD is introduced. A numerical model is developed to simulate the electro-optic properties of blue phase LCDs based on in-plane-switching (IPS) structure. Detailed electrode dimension effect, distribution of induced birefringence, cell gap effect, correlation between operation voltage and Kerr constant, and wavelength dispersion are investigated. Viewing angle is another important parameter. We have optimized the device configurations according to the device physics studied. With proper new device designs, the operating voltage is decreased dramatically from around 50 Volts to below 10 Volts with a reasonably high transmittance (~70%) which enables the BPLCDs to be addressed by amorphous silicon thin-film transistors (TFTs). Moreover, weak wavelength

dispersion, samll color shift, and low hysteresis BPLCDs are achieved after their root causes being unveiled. Optimization of device configurations plays a critical role to the widespread applications of BPLCDs.

In addition to displays, blue phase liquid crystals can also be used for photonic applications, such as light modulator, phase grating, adaptive lens and photonic crystals. We will introduce the application of blue phase liquid crystal as a modulator to realize a viewing angle controllable display. The viewing angle can be tuned continuously and precisely with a fast response time. The detailed design and performance are also presented in this dissertation.

To my beloved family and dear friends

ACKNOWLEDGMENTS

The research work presented here would have never been possible without the guidance and patience of my advisor Prof. Shin-Tson Wu. Prof. Wu has been not only an advisor in my academic career, but also a mentor in my scientific development. I would also like to thank my committee members, Prof. Eric Van Stryland, Prof. Boris Zeldovich, and Prof. Thomas Wu for their enduring support and help.

During the course of this research, many people have assisted or contributed to my work in various ways. Thanks to Dr. Zhibing Ge, thanks to all the current and previous members of the photonics and display group for the valuable discussions and inspirations.

I would also like to thank my dear friends, for their caring and support along the way.

Last but not least, my greatest gratitude goes to my parents, for their unconditional love, support, and encouragement.

TABLE OF CONTENTS

LIST OF FIGURES

LIST OF TABLES

CHAPTER 1: INTRODUCTION

1.1 Background and Motivation

Liquid crystal (LC) was first discovered in 1888 by an Austrian botanist Friedrich Reinitzer and the name was coined in 1904 by a German physicist Otto Lehmann. Liquid crystal is an intermediate state of matter between isotropic fluids and crystalline solids. It can be also viewed as a liquid in which an ordered arrangement of molecules exists. Based on the different orderings of molecules and their optical properties, liquid crystals can be divided into thermotropic, lyotropic and polymeric phases, among which a lot of research work has been done towards the thermotropic phase [1, 2]. Many thermotropic LCs exhibit a variety of states as temperature increases: from solid to anisotropic liquid crystal, to isotropic liquid when thermal energy deteriorates the delicate cooperative ordering of the LCs, and finally to vapor state [3, 4].

After decades of active research, device development, and massive investment in manufacturing technology, liquid crystals have been extensively used in display applications and liquid crystal display (LCD) industry has dominated flat panel display market. Nowadays, LCDs have become indispensable in our daily life, ranging from cell phones, computers, TVs, to data projectors [5].

Figure 1.1 depicts the basic structure of a transmissive LCD. A LCD panel usually consists of a backlight unit, polarizers, driving circuits, a liquid crystal layer and color filters. Liquid crystal is non-emissive; therefore a backlight is needed to illuminate the LC panel. The backlight films, such as light guide plate, diffuser, and brightness enhancement films, are employed in the backlight unit to make the light distribution more uniform. The LC layer is

sandwiched between two crossed linear polarizers. Thin-film-transistor (TFT) arrays are usually used to drive the pixels. The RGB color filters are fabricated on the top substrate to make a full-color display.

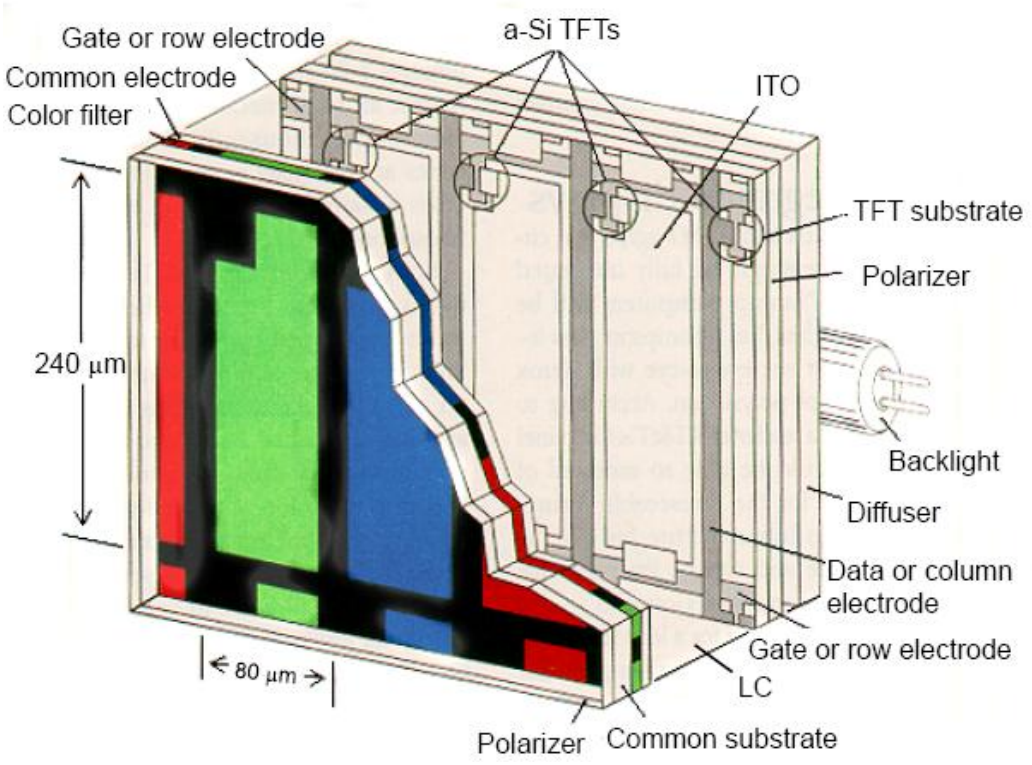

Figure 1.1 Device structure of a tranmissive TFT-LCD

The first liquid crystal display device was developed in the mid-1960s with dynamic scattering mode (DSM) [6]. To address the stability issue of DSM mode, the twisted nematic (TN) LCD mode was proposed in the 1970s [7, 8]; to improve the resolution, the super twisted nematic LCD mode were invented [9]; to widen the viewing angle and increase the contrast ratio, in-plane switching (IPS) mode [10] and vertical alignment (VA) mode were developed in the 1990s and then implemented in the 2000s [11]. The LCD industry has been continuingly advanced by the development of new technology. The most critical issue on viewing angle has

been further addressed by using multidomain structures and optical film compensation. The motion image blur has been significantly reduced by impulse driving and frame insertion. The color shift at oblique viewing angle has been dramatically reduced by eight domain approach via two transistors. The contrast ratio has exceeded one million-to-1 through local dimming of the LED backlight. The color gamut would exceed 100% NTSC, if RGB LEDs are used. Besides these technological advances, the cost is also reduced dramatically by investing in advanced manufacturing lines. However, there's still an urgent need for fast response time.

Fast response time not only reduces the undesirable motion picture image blurs but also enables color sequential liquid crystal displays (LCDs) using RGB (red, green, blue) LED backlight [12, 13]. The latter is particularly attractive because it eliminates spatial color filters, which in turn triples the optical efficiency and resolution density. Higher optical efficiency leads to lower power consumption which implies to energy saving and longer battery life. However, in order to minimize color breakup in color sequential displays, the LC response time should be less than one millisecond which imposes a big challenge to nematic LCDs [14, 15]. Various approaches for reducing LC response time have been developed, such as thin cell gap [16, 17], overdrive and undershoot voltage [18, 19], bend cell [20-22], and low viscosity LC materials [23]. However, the state-of-the-art LC response time is around 2-3 ms. Therefore, developing LCDs with submillisecond response time is in need.

1.2 Introduction to Blue Phase Liquid Crystals

Recently, a promising new technology involving blue phase liquid crystal (BPLC) is emerging [24]. BPLC was first discovered by Reinitzer in 1888 on the melting behavior of cholesteryl benzoate. It turned blue as it changed from clear state to cloudy upon cooling. This is

also the origin of the name of blue phase LC. Blue phase is a distinct thermodynamic phase that appears over a narrow temperature range (1–2^{o}C) between the chiral-nematic/cholesteric (CH) and isotropic phases. Figure 1.2 shows the schematic plot of the phases between nematic and isotropic phases. The top part shows that non-chiral molecules having only nematic and isotropic phases, as the temperature increases, the liquid crystals will directly transform to isotropic phase; the bottom part depicts that for chiral molecules, as the temperature increases, three stages of blue phases (BP-I, BP-II and BP-III) would appear between chiral-nematic (i.e., cholesteric) phase and isotropic phase [25].

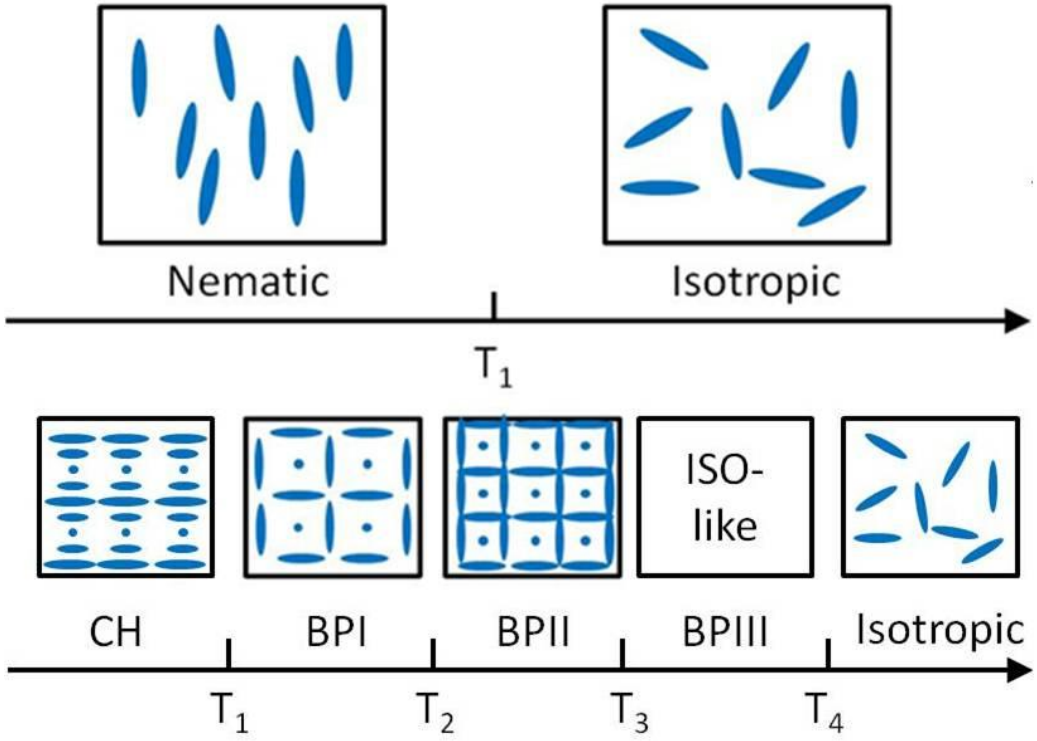

Figure 1.2 Schematic picture of the temperature region near the nematic-to-isotropic phase transition. Top: nonchiral molecules have only nematic and isotropic phases; Bottom: three stages of blue phases appear between chiral nematic/cholesteric (CH) phase and isotropic phase.

BP-I and BP-II exhibit three-dimensional periodic structures in the director field as shown in Figure 1.3. They have body-centered and simple cubic symmetry, respectively. BP-III is seemingly amorphous; it has a same symmetry as the isotropic phase.

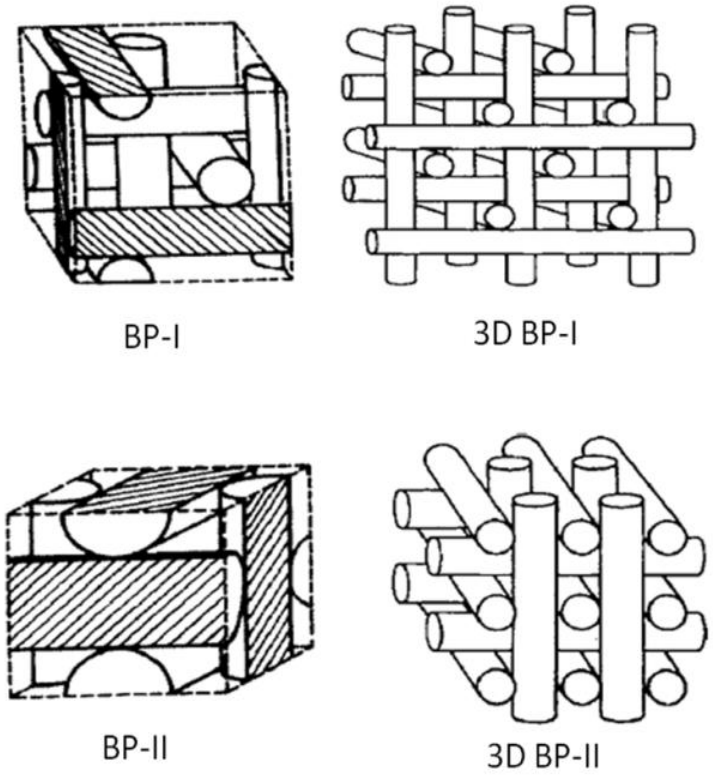

Figure 1.3 Cubic structures of BP-I and BP-II.

Figure 1.4 is the molecular structure of blue phase LC with cubic structure. The liquid crystal molecules have a double-twist alignment filled up in a cylinder. There is in fact unlimited number of helical axes presented; however the structure was named double-twist. The LC directors perform a 45 degree rotation from the center line. Due to the orientation of the LC molecules, microscopically, blue phase is optically anisotropic. The diameter of the cylinder is in the range the pitch length of the chiral nematic LC of ~100 nm. Because of this small range local reorientation, blue phase has a very fast response. So far, a microsecond-response BPLC with 39

μs decay time at room temperature has been demonstrated [26]. The double-twist cylinders further form the cubic symmetry, therefore, blue phase is optically isotropic macroscopically. The double-twist alignment is more stable than the single-twist structure such as the chiral nematics with normal helical structure. However, the double-twist cylinders cannot fill the cubic space completely uniformly to allow the directors to be matched everywhere. Meiboom has introduced the defect theory that defects occur at the intersections between the double-twist cylinders in the cubic structure [27]. The cubic structure of blue phase is stabilized by the lattice defects. The disclination lines in Figure 1.4 (d) are the defect lines.

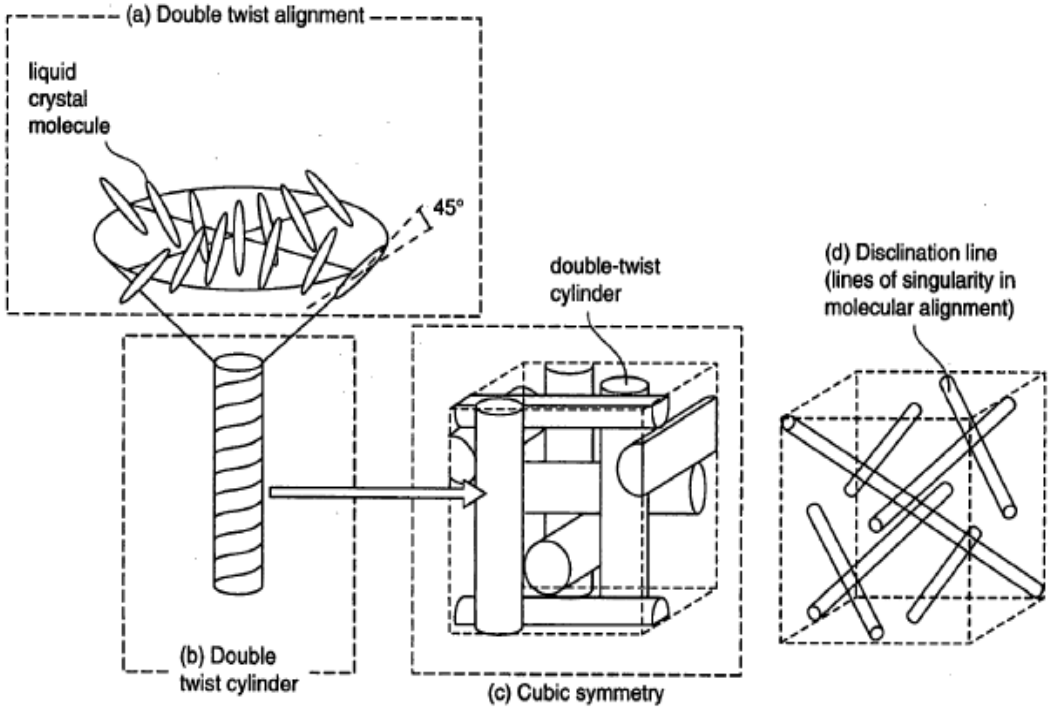

Figure 1.4 Blue phase LC structure at the microscopic level: (a) double-twist alignment of LC molecules; (b) double-twist cylinder; (c) lattice cubic symmetry formed by double-twist cylinders and (d) disclination lines of singularity in molecular alignment.

The temperature range in which the defect structure exists is very narrow (around 1-2 ^{o}C) and is a problem from the viewpoint of practical applications. In 2002, Kikuchi proposed a polymer stabilization method in which an equilibrium phase is thermodynamically stabilized by the coexistence of a polymer. Polymer chains are formed selectively in the dislination core, and therefore the blue phase composite does not require a thermal energy to keep the disclination core isotropic at a temperature below isotropic phase. Through this method, the temperature range is reported to be expanded to more than 60 degree including room temperature.[28]

In a cholesteric (chiral nematic) liquid crystal, the selective reflection wavelength is $\lambda=n\cdot P$, where n is the average refractive index and P is the pitch length. The reflection band has a bandwidth $\Delta\lambda=\Delta n\cdot P$, where Δn is the LC birefringence and $\Delta\lambda$ is relatively broad. For BP-I and BP-II, because of the cubic symmetry, there are several selective reflections of incident light corresponding to different crystal planes, known as the Bragg diffractions. However, the color being reflected is not always blue as it's been first discovered by Reinitzer, the reflection wavelength is affected by the chirality, the lattice parameter (a), and the direction and Miller indices (h, k, l) of the Bragg plane. The reflection wavelength can be expressed as:

$$\lambda = \frac{2na}{\sqrt{h^2 + k^2 + l^2}} \tag{1.1}$$

For BP-I, the lattice constant corresponds to one pitch length (P) and diffraction peaks appear when the sum of the Miller indices (h+k+l) is equal to an even number, such as (110), (200), and (211). For BP-II, the lattice constant corresponds to half a pitch length (P/2). The diffraction peaks of BP-II could appear no matter the sum of the Miller indices (h+k+l) is even or odd, such as (100) and (110) . The pitch length of a BPLC is slightly different from that of chiral nematic phase. The reflection bandwidth is also much narrower than that of chiral nematic phase

[29]. Figure 1.5 shows the platelet textures of two BPLCs under crossed polarizers [30]. The different colors of the left and right pictures are from different pitch lengths. The multiple colors in each picture correspond to different crystal planes (Miller indices). For display applications, by adjusting the chirality in the BPLC, the reflection band can be shifted outside the visible spectral region.

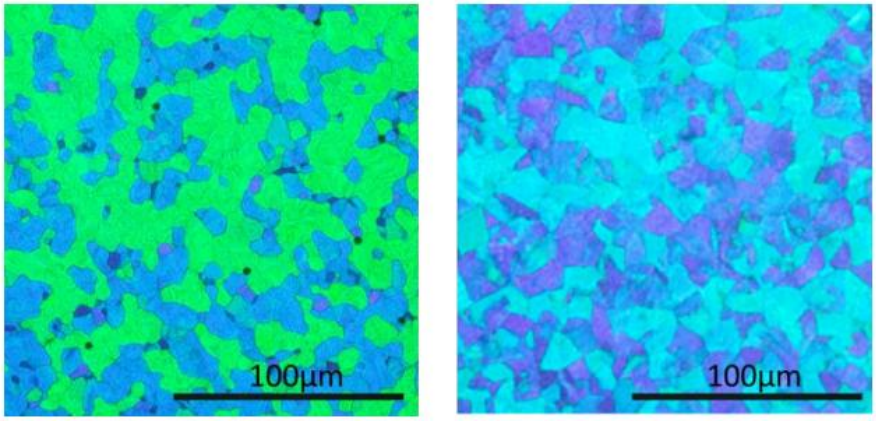

Figure 1.5 BPLC platelet textures under polarizing optical microscope with different chiral concentrations.

As introduced before, macroscopically, BPLC appears optically isotropic. According to Kerr effect [31], if an electric field is applied to the BPLC, birefringence will be induced and the LC refractive-index distribution becomes anisotropic. When the BPLC device is sandwiched between two crossed polarizers, the transmittance gradually increases as the voltage increases. Therefore, from application viewpoint, blue phase LCs with fast response are of interest for high speed light modulators, tunable photonic crystals, as well as displays.

In comparison to conventional nematic LCDs, polymer-stabilized blue phase exhibits some very attractive features: 1) It does not require any alignment layer, such as polyimide, which not only simplifies the manufacturing processes but also reduces the cost. 2) Its response

time is in the submillisecond range, which helps to minimize the motion-image blur and, more importantly, enables color-sequential displays without pigment color filters if an RGB LED backlight is used. The major impacts of eliminating color filters are threefold: (i) it enhances optical efficiency by ~3X, resulting in lower power consumption if the same display brightness is compared; (ii) it increases device resolution by 3X (*i.e.*, crisper images); and (iii) it reduces production cost. 3) The dark state of a blue phase LCD is optically isotropic so that its viewing angle is wide and symmetric. Optical compensation films may or may not be needed, depending on the actual applications. 4) The transmittance is insensitive to the cell gap, as long as the cell gap exceeds about 3 μm depending on the IPS electrodes employed. This cell-gap insensitivity is particularly attractive for fabricating large-screen or single-substrate LCDs, in which cell-gap uniformity is a big concern, or for single substrate LCDs for slimness and light weight.

Although polymer-stabilized blue phase LCDs hold so many promises, some tough technical issues remain to be overcome before the widespread applications. The major challenges are: (1) The operation voltage is still too high (~50 V_{rms} *vs.* 5 V_{rms} for conventional nematic LCDs), (2) the transmittance is relatively low (~65% *vs.* 85% for nematic LCDs), (3) the mesogenic temperature range is still not wide enough for practical display applications (from –40^{o}C to 80^{o}C), and (4) other challenges such as hysteresis, long term stability and residual birefringence. The operating voltage of a blue phase LCD is primarily governed by the induced birefringence which in turn is dependent on the Kerr constant (K) of the LC composite and the electric-field strength. Therefore, developing new blue phase LC materials with a large Kerr constant and new device structures for enhancing the effective electric-field intensity are urgently needed.

In this dissertation, electro-optic properties of blue phase LCs are studied. A computation

numerical model is developed to understand the underlying device physics of BPLCDs. Parameters affecting the device performance with an in-plane-switching (IPS) structure, such as electrode dimension, induced birefringence distribution, cell gap, the relationship of Kerr constant and voltage are investigated. Viewing angles are also studied. The device physics study provides guidance to the optimization of blue phase liquid crystal devices. New configurations are proposed to achieve low operating voltage, low color shift, hysteresis-free and wavelength-dispersion-free BPLCDs. Those approaches will undoubtedly accelerate the emergence of BPLC as next-generation display and photonic devices.

CHAPTER 2: ELECTRO-OPTICS OF POLYMER-STABILIZED BLUE PHASE LIQUID CRYSTALS

2.1 Kerr Effect

Kerr effect is a type of quadratic electro-optic effect caused by an electric-field-induced ordering of polar molecules in an optically isotropic medium. It usually exists in crystals with centro-symmetric point groups. If an electric field E is applied to a Kerr medium, such as polymer-stabilized BPLC or optically isotropic LC composite, birefringence will be induced which is related to E as:[31]

$$\Delta n_{ind} = \lambda K E^2 \tag{2.1}$$

where λ is the wavelength and K is the Kerr constant. From Eq. (2.1), the induced birefringence is linearly proportional to E^2.

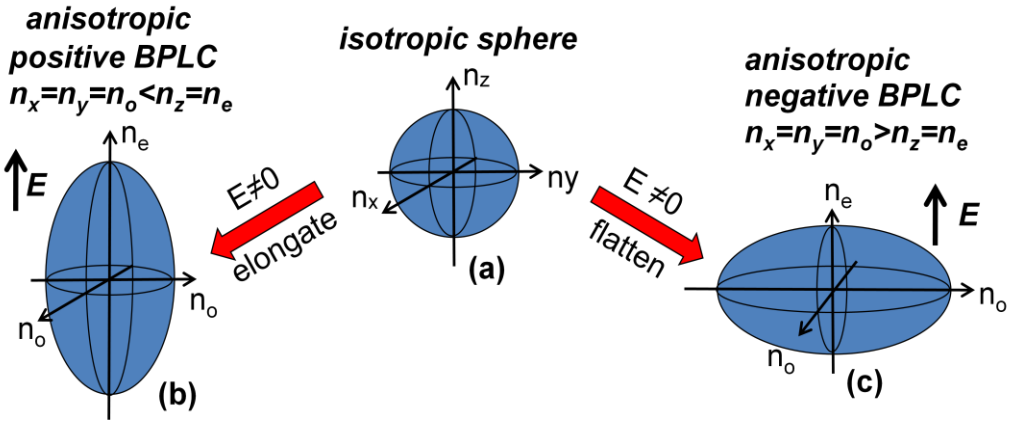

Figure 2.1 Electro-optic effect on BPLC refractive index ellipsoid: (a) BPLC without an electric field, (b) positive $\Delta\varepsilon$ BPLC with an electric field, and (c) negative $\Delta\varepsilon$ BPLC with an electric field.

The induced anisotropy will be along the direction of the electric field. Consequently, the isotropic sphere will appear as an elongated (Figure 2.1(b)) or a flattened (Figure 2.1(c)) ellipsoid, depending on whether the host LC has a positive or negative dielectric anisotropy ($\Delta\varepsilon$) [32]. Eq. (2.1) is valid only when the electric field is weak. As E keeps increasing, the induced birefringence will gradually saturate, as clearly described by the following extended Kerr effect:[33]

$$\Delta n_{ind} = \Delta n_s (1 - \exp[-(E / E_s)^2]) \tag{2.2}$$

where Δn_s denotes the saturated induced birefringence and E_s is the saturation electric field. In the weak field region ($E << E_s$), we can expand Eq. (2.2) and deduce the Kerr constant as:

$$K \approx \Delta n_s / (\lambda E_s^2) \tag{2.3}$$

From Eq. (2.3), a BPLC material with high Δn_s and low E_s will result in a large Kerr constant. Roughly speaking, Δn_s governs the optical property (e.g., maximum phase change) and E_s determines the electric property (operating voltage) of a BPLC material. As will be discussed in detail later, Kerr constant plays a key role on the operating voltage of the BPLC devices. A typical Kerr constant of BPLC composite is around 1 nm/V^2. In 2009, Kikcuhi et al.[34] reported a polymer-stabilized isotropic phase (PSIP) composite with K~10 nm/V^2 and its operating voltage in an IPS cell (5 μm electrode width and 10 μm electrode gap) is ~50 V_{rms}.

2.2 Temperature Effect

Although Kerr constant plays a crucial role on the performance of a PSBP or PSIP BPLC composite, only scattered data are available in literatures discussing about its temperature effect

[35]. Moreover, the response time of these LC composites are highly sensitive to the operating temperature. In this section, the temperature dependent Kerr constant and response time will be presented, as well as the correlation between these experimental results with physical models [36]. Very good agreement between experiment and theory is found.

We have set up an experiment using UCF BPLC material, the host nematic LC has a birefringence of 0.17 (λ=589nm, T=20 ^{o}C) and clearing temperature of 94 ^{o}C. It was mixed with chiral dopants (22.7% Merck CB15 and 4.7% ZLI-4572), monomers (3.9% RM257, 4.6% Aldrich M1, and 7.7% EHA) and photoinitiator (1.5% darocur). The reason that we mixed some M1 is to lower the operating voltage [37]. Usually, the blue phase temperature range is rather narrow (~3-5^{o}C) and we need to control the temperature uniformly across the cell. To overcome this problem, we could conduct UV curing in an isotropic state. Similar to that cured at a blue phase, the curing in an isotropic phase also produces nanostructured optically isotropic composite and its electro-optic properties still follow Kerr effect. In our experiment, we filled the BPLC mixture into an IPS cell with a cell gap of 7.5 μm. The ITO (indium tin oxide) electrode width is 10 μm and electrode gap is 10 μm. UV curing process was performed at 70 ^{o}C (isotropic state) for 30 min. After polymerization, the clearing temperature of the PSIP composite was measured to be T_c~54 ^{o}C, which was only ~5^{o}C below that of the host LC/chiral mixture (before mixing with the monomers).

We first measured the voltage-dependent transmittance (VT) of our IPS cell by placing it between two crossed polarizers. A CW He-Cd laser (λ=441.8 nm) was used as the light source. The main reason that we chose a shorter wavelength rather than a He-Ne laser (λ=633 nm) was to obtain a transmission peak at a lower voltage.

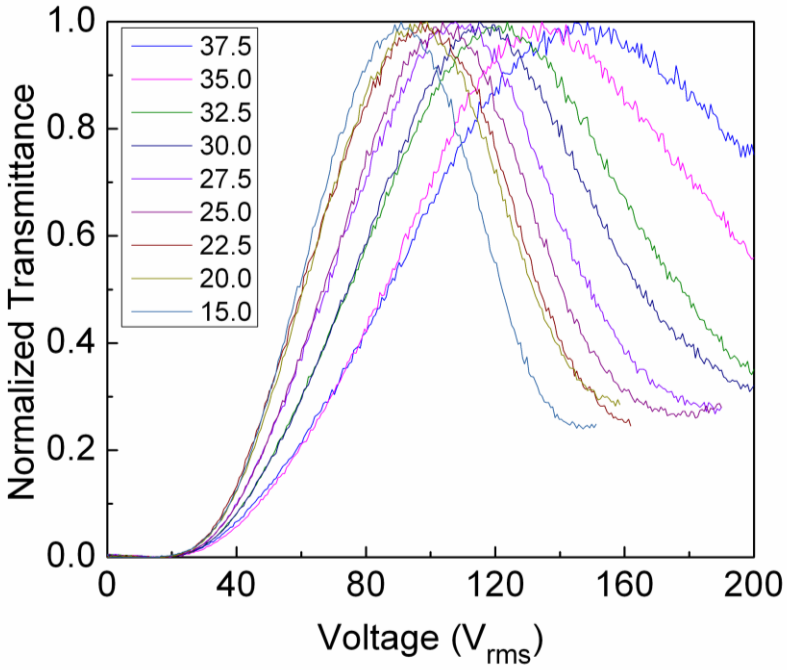

Figure 2.2 Voltage dependent normalized transmittance curves of the IPS PSIP composite cell measured from 15 ^{o}C to 37.5 ^{o}C. Electrode width=10 μm, electrode gap=10 μm and cell gap=7.5 μm. λ=441.8 nm.

Figure 2.2 shows the normalized VT curves measured from 15 ^{o}C to 37.5 ^{o}C (where the total phase retardation is still larger than 1π). As the temperature increases, the on-state voltage (V_{on}; corresponding to the peak transmittance) shifts to the right, indicating that Kerr constant decreases with the temperature. From Figure 2.2, the on-state voltage of our PSIP sample occurs at V_{on} ~90 V_{rms} at 15^{o}C. A high V_{on} implies a relatively small Kerr constant. We fitted the VT curves shown in Figure 2.2 with the extended Kerr effect model [Eq. (2.2)] at each temperature. The obtained *K* values are plotted in Figure 2.3. As the temperature increases, the Kerr constant decreases gradually.

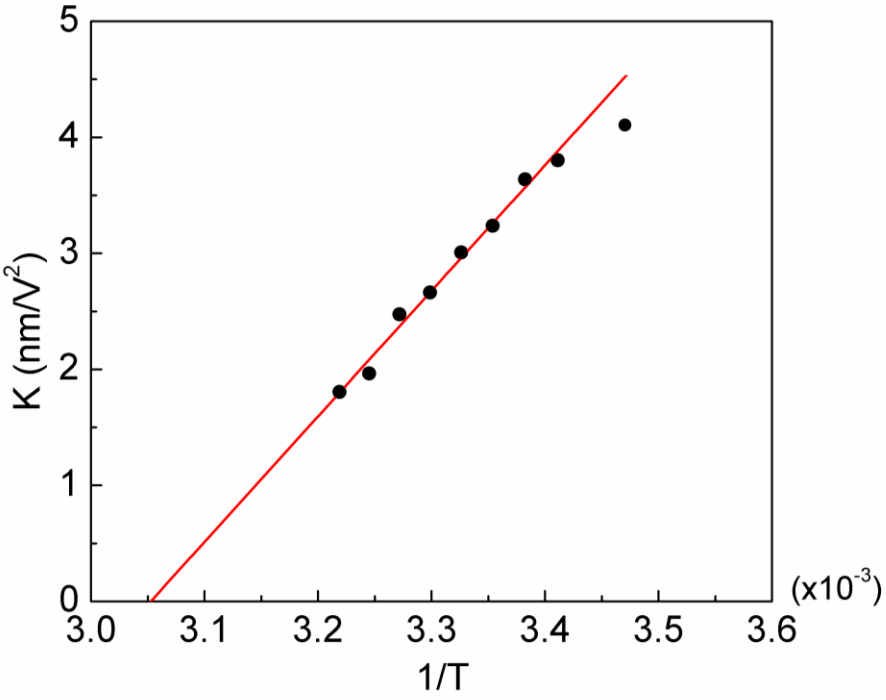

Figure 2.3 Kerr constant with the reciprocal of temperature (red line: linear fit of the Kerr constant with the reciprocal of temperature according to Eq. (2.8). T: Kelvin temperature. The fitting parameter is $\alpha = 1.08 \times 10^{-5}\, m \cdot K / V^2$).

To explain this trend, we need to derive the temperature dependent Kerr constant. It has been reported by Gerber that the Kerr constant can be approximated by the following equation [38]:

$$K \sim \frac{\Delta n_{ind}}{\lambda E^2} \approx \Delta n \cdot \Delta\varepsilon \frac{\varepsilon_o P^2}{k\lambda(2\pi)^2}. \qquad (2.4)$$

where Δn_{ind} is the induced birefringence, Δn, $\Delta\varepsilon$ and k are the intrinsic birefringence, dielectric anisotropy, and elastic constant of the host LC material, and P is the pitch length. Furthermore, we know that Δn, $\Delta\varepsilon$ and k are related to the nematic order parameter (S) as $\Delta n \sim \Delta n_o S$ [39],

$\Delta\varepsilon \sim S/T$, and $k \sim S^2$ [40].

Next, we should consider the temperature dependent pitch length. If a cholesteric LC exhibits a pre-transitional phenomenon, like the Smectic-A phase, then its temperature-dependent pitch length can be expressed as [41]:

$$P = P_o + P_1(\frac{T - T^*}{T^*})^{-\alpha'} \tag{2.5}$$

where P_o is the cholesteric LC pitch length, T^* is the Sm-A phase transition temperature, and P_1 and α' are fitting parameters. In the example shown in Ref. 41, T^*~297.5 K, $P_1 \cdot (1/T^*)^{-\alpha'}$ =230 nm, and α'~0.78. In the vicinity of T^*, P is indeed sensitive to the temperature. However, if the temperature is far away from T^*, which is, $T >> T^*$, then Eq. (2.5) can be simplified to:

$$P \approx P_o + 230nm \cdot T^{-\alpha'}. \tag{2.6}$$

Under such condition, the second term in Eq. (2.6) is much smaller (<1%) than the first term (P_o is usually ~350 nm) and can be neglected. In our BPLC composite, although there is no Sm-A phase we can still treat T^* as a virtual transition temperature with $T >> T^*$. Thus, we can ignore the temperature effect of pitch length in Eq. (2.5).

Plugging these parameters into Eq. (2.4), we find the temperature dependent Kerr constant has following simple form:

$$K \approx \Delta n \cdot \Delta\varepsilon \frac{\varepsilon_o P^2}{k\lambda(2\pi)^2} \sim \Delta n_o S \cdot S/T \cdot \frac{1}{S^2} \cdot \frac{\varepsilon_o P^2}{\lambda(2\pi)^2} \sim \alpha \cdot \frac{1}{T}. \tag{2.7}$$

Thus, in theory the Kerr constant is linearly proportional to the reciprocal temperature, and α is the proportionality constant. However, as the temperature approaches the clearing point (T_c) of the LC composite, Kerr constant should vanish (or at least dramatically decreased)

because both Δn and $\Delta\varepsilon$ are approaching zero. To satisfy this boundary condition, we rewrite Eq. (2.7) as follows:

$$K = \alpha \cdot (\frac{1}{T} - \frac{1}{T_c}) . \qquad (2.8)$$

Eq. (2.8) predicts that Kerr constant decreases linearly with reciprocal of temperature (*1/T*) and eventually vanishes as the temperature reaches clearing point.

In experiment, we could treat the linear coefficient α and clearing temperature T_c as fitting parameters. Results are depicted in Figure 2.2. From fittings, we find $\alpha = 1.08 \times 10^{-5} m \cdot K / V^2$ and T_c=327.58 K (54.43 ^{o}C). The fitted T_c matches very well with the measured clearing temperature (54 ^{o}C) of the LC composite. Thus, Eq. (2.8) actually has only one adjustable parameter which is α.

In Figure 2.2, as the temperature decreases (or *1/T* increases) the Kerr constant gradually deviates from the linear extrapolation. This is because in the low temperature region the higher order term of the elastic constant becomes increasingly important and should be included: [42]

$$k = a_1 S^2 + a_2 S \overline{P}_4 \qquad (2.9)$$

where a_1 and a_2 are coefficients, and $\overline{P}_4$ is the fourth rank of the order parameter. From previous experimental results, in the low temperature region the second term in Eq. (2.9) makes ~30-40% contribution to enhance the elastic constant [43]. Thus, the Kerr constant in the lower temperature region may not increase as rapidly as the fitting line shows.

From Eq. (2.1) and the VT curves shown in Figure 2.1, we could also extrapolate the data of the saturated induced birefringence Δn_s under different temperatures. Results are depicted in Figure. 2.4. As the temperature increases, Δn_s decreases gradually. To understand the responsible

physical mechanisms, we need to know the temperature dependent birefringence of the BPLC composite system.

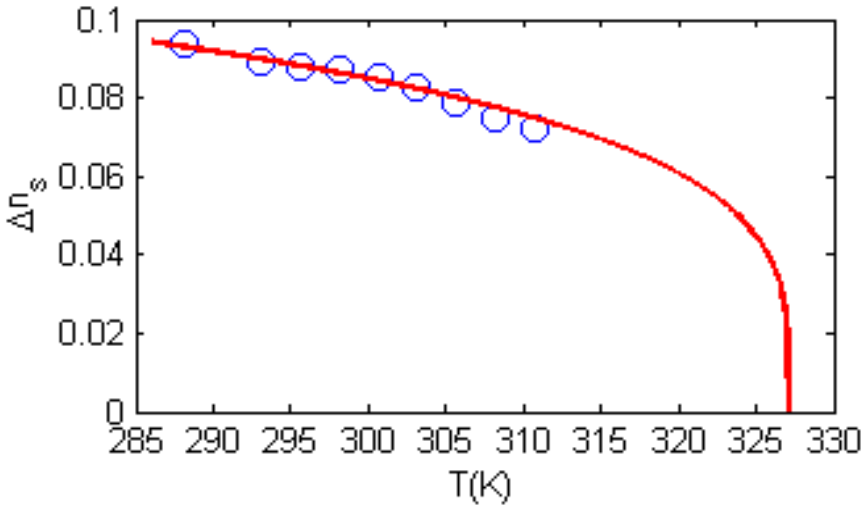

Figure 2.4 Temperature dependent saturated induced birefringence. Open circles are experimental data and line represents fitting using Eq. (2.10) with $(\Delta n_s)_o$=0.159 and β=0.25.

Temperature dependent Δn_s is proportional to order parameter (S) which in turn can be approximated by Haller's semi-empirical equation [44]:

$$\Delta n_s = (\Delta n_s)_o S , \tag{2.10}$$

and $$S = (1 - T/T_c)^{\beta} . \tag{2.11}$$

Here, $(\Delta n_s)_o$ is the extrapolated birefringence at T=0 K, T_c is the clearing temperature of our LC composite (~54°C), and the exponent β is a material constant. For many nematic LC materials studied, β is ~0.21±0.06 [45, 46]. Eq. (2.10) works well as long as the temperature is not too close (within 1°C) to the clearing point. As shown in Eqs. (2.10) and (2.11), there are two

fitting parameters: $(\Delta n_s)_o$ and β. From the fitting curve shown in Figure 2.4, we find $(\Delta n_s)_o$=0.159 and β=0.25. We also measured the temperature dependent birefringence of our nematic host and found $(\Delta n_s)_{o\text{-}host}$ =0.275 and β_{host}=0.245. The material constant β of the PSIP composite keeps almost the same as that of the host LC material. It means that the polymer only helps to stabilize the molecular arrangement in the LC composite but does not affect the intrinsic material property of the host LC too noticeably. On the other hand, knowing $(\Delta n_s)_{o\text{-}host}$ =0.275 and LC concentration (~54.8%) in our LC/polymer composite we estimate that $(\Delta n_s)_o$~0.151. In comparison, through fitting our obtained $(\Delta n_s)_o$ is 0.159. The difference is less than 5%. This is another success between our experimental results and physical models.

To further verify the model, we have done another experiment with Chisso's BPLC material designated as JC-BP01M [47]. We injected JC-BP01M into an IPS cell with cell gap d=7.5 μm, ITO (indium tin oxide) electrode width w=10 μm and electrode gap l=10 μm. We then heated the cell from chiral nematic phase to blue phase with the temperature slightly higher than the BP-I transition temperature. We held the temperature for 1 min and then conducted UV curing (intensity ~20 mW/cm^2 and λ~365 nm). After polymerization, the clearing temperature of the PSBP composite was measured to be T_c~70 ^{o}C. We measured the VT curve of our IPS cell with a He-Ne laser (λ=633 nm).

Figure 2.5 is the normalized VT curves from 15 ^{o}C to 65 ^{o}C. Figure 2.6 shows the linear fit of the Kerr constant with the reciprocal temperature according to Eq. (2.8). Different from the UCF BPLC material, the fitting parameter is $\alpha = 2.644\times10^{-5}\, m\cdot K/V^2$. Here, we have for the first time demonstrated a polymer-stabilized BPLC mixture with a large Kerr constant K~13.7 nm/V^2 at 20^{o}C and λ=633 nm. The corresponding on-state voltage is ~48V_{rms} in an IPS cell with

10-μm electrode width and 10-μm electrode gap. By fitting the VT curves shown in Figure 2.5 with extended Kerr effect model, we also obtained Δn_s at different temperatures in Figure 2.7. From the fitting curve shown in Figure 2.7, we find $(\Delta n_s)_o$=0.232 and β=0.25. From the two sets of experiments with UCF PSIP material and Chisso PSBP (JC-BP01M), our proposed physical model between Kerr constant and temperature has been substantially validated.

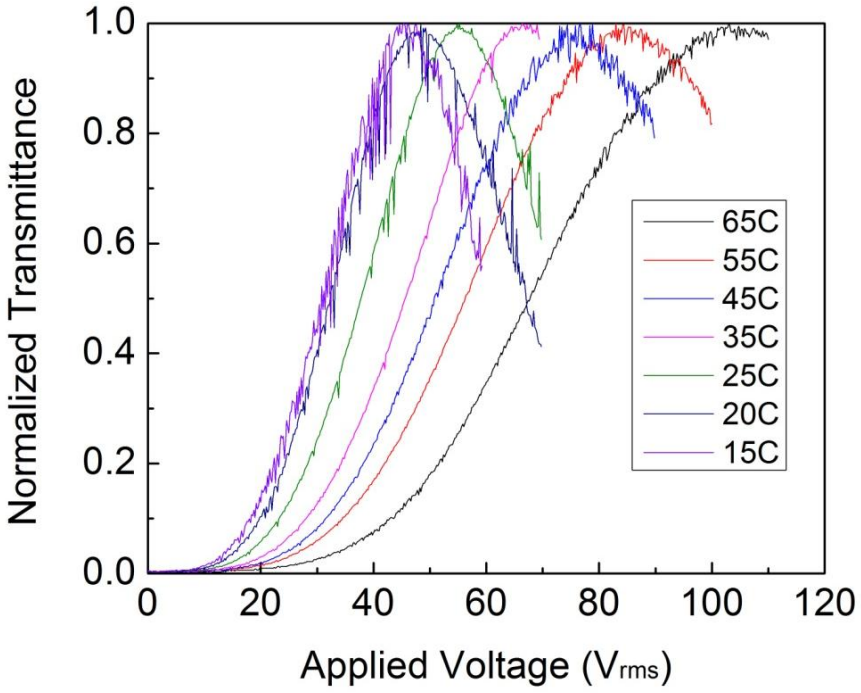

Figure 2.5 Measured VT curves of the IPS PSBP cell (Chissco JC-BP01M) at elevated temperatures. Electrode width=10 μm, electrode gap=10 μm, and cell gap=7.5 μm. λ=633 nm.

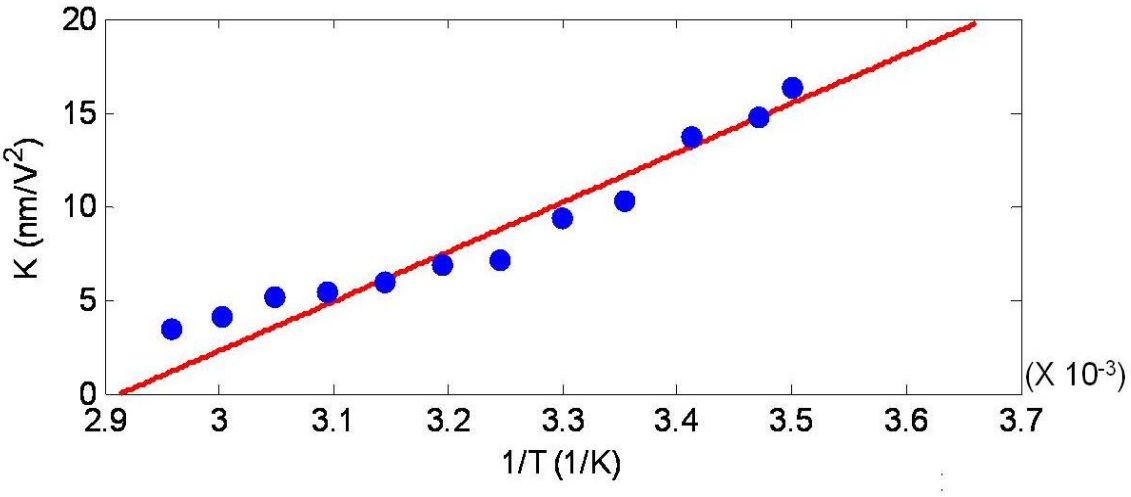

Figure 2.6 Linear fit of Kerr constant with reciprocal temperature according to Eq. (2.8). T: Kelvin temperature. The fitting parameter is $\alpha = 2.644 \times 10^{-5}\, m \cdot K / V^2$.

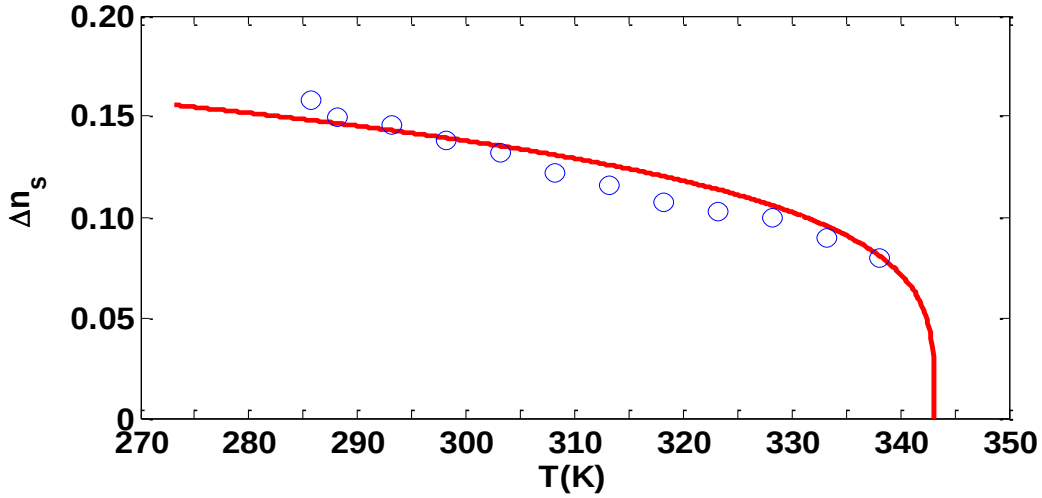

Figure 2.7 Temperature dependent saturated induced birefringence. Open circles are experimental data and solid line represents fitting using Eq. (2.10) with $(\Delta n_s)_o$=0.232 and β=0.25.

2.3 Optical Response Time

Fast response time is one of the most attractive features of PSBP or PSIP LCDs since it helps to reduce motion blur and enable color-sequential display while minimizing color breakup. For the experiment in Sec. 2.2 with UCF PSIP material, besides the VT curves, we also measured the decay time of our LC composite from 22.5 ^{o}C to 40 ^{o}C. We did not measure the rise time because it depends on the applied voltage [48]. The decay time is defined as 100%-10% transmittance change. The measured data are plotted in Figure 2.8.

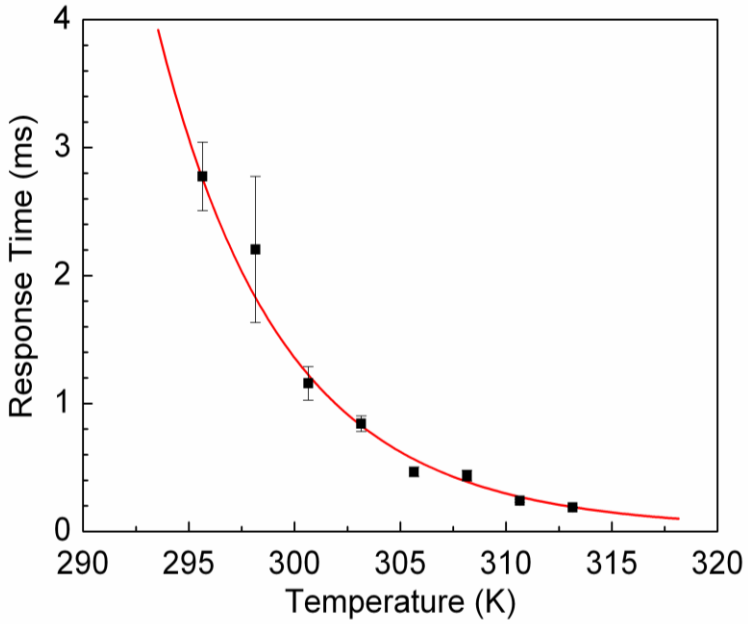

Figure 2.8 Temperature dependent decay time. Dots are experimental data and line represents fitting using Eq. (2.14) with B=7.16·10^{-23} ms and E_a=1.31 eV

As the temperature increases, the decay time decreases rapidly. At room temperature, the response time of BPLC is indeed experimentally shown being submillisecond. For example, we note from Figure 2.8 that the response time is decreased by 2X when the temperature is increased by merely 4-5 degrees. This changing rate is ~3X more sensitive than that of most nematic LCs.

To understand this phenomenon, we need to develop a physical model to explicitly correlate the temperature dependent response time with LC parameters. The free relaxation time of a polymer-stabilized blue phase or optically isotropic LC composite can be approximated by [5, 49]:

$$\tau \approx \frac{\gamma_1 P^2}{k(2\pi)^2}, \tag{2.12}$$

with γ_1 being the rotational viscosity, P the pitch length, and k the elastic constant. As discussed in Eq. (2.6), the pitch length is insensitive to the temperature and can be treated as a constant.

From mean field theory [40], elastic constant is related to the nematic order parameter (S) as $k \sim S^2$. With regard to rotational viscosity, the following modified Arrhenius model works well to describe the temperature dependent rotational viscosity of nematic LCs [50, 51]:

$$\gamma_1 \sim S \cdot \exp(E_a / K_B T), \tag{2.13}$$

where E_a is the activation energy of molecular rotation and K_B is the Boltzmann constant. With Eq. (2.13) and treating P as a constant, we can rewrite Eq. (2.12) as:

$$\tau \approx \frac{\gamma_1 P^2}{k(2\pi)^2} \sim \frac{S \cdot \exp(E_a / K_B T) \cdot P^2}{S^2 \cdot (2\pi)^2} \approx B \cdot \frac{\exp(E_a / K_B T)}{(1 - T/T_c)^\beta}. \tag{2.14}$$

Eq. (2.14) has two unknowns: B and E_a. As shown in Figure 2.8, Eq. (2.14) fits quite well with our measured response time data. Through fitting, we obtain B=7.16·10^{-23} ms and E_a=1.31 eV. The obtained activation energy is ~3X higher than that of E7 [50, 52]. Our host nematic LC has a similar viscosity and E_a as E7. The increased E_a is believed to originate from the viscous chiral dopants (22.7% Merck CB15 and 4.7% ZLI-4572).

From Eq. (2.14), we can check how much temperature change is needed in order to result in a 2X reduction in response time. To do so, we set $\tau=\tau_1$ when $T=T_1$ and $\tau=\tau_2$ when $T=T_2$, assuming $T_2>T_1$. Our objective is to find (T_2-T_1) which will make $\tau_2=0.5\tau_1$. With some algebra and assuming $\beta=0.25$, we derive following equation:

$$T_2 - T_1 \approx 0.693 K_B T_1 T_2 / E_a. \quad (2.15)$$

Substituting $T_2=T_1+(T_2-T_1)$ to the right side of Eq. (2.15) and assuming $(T_2-T_1)<< T_1$, we find:

$$T_2 - T_1 \approx 0.693 K_B T_1^2 / E_a. \quad (2.16)$$

Let us assume T_1 is around room temperature (~300K) and use E_a ~1.31 eV, we find T_2-T_1 ~ 4K. That is to say, the response time will decrease by 2X as the operating temperature increases by merely ~4 ^{o}C. This change rate is ~3X more sensitive than E7 and MLC-6608 because our LC composite has 3X higher E_a than E7 and MLC-6608 [43].

From Eq. (2.14), a low viscosity host (smaller activation energy) is always in favor for achieving fast response time. However, there are tradeoffs between response time and Kerr constant. For example, from Eq. (2.4) a smaller elastic constant k and a larger pitch length P leads to a larger Kerr constant, but from Eq. (2.14) the response time will be slower. Similarly, a larger dielectric anisotropy helps to enhance Kerr constant, but it could dramatically increase viscosity and thus slow down the response time. The polymer-stabilized blue phase or optically isotropic liquid crystal composite is a complex system, as it consists of nematic liquid crystal host, chiral agents, and two types of monomers. Both material optimization and UV curing process need to be optimized.

2.4 Summary

In this chapter, we studied the basic electro-optic properties of blue phase liquid crystal materials. We have introduced Kerr model and extended Kerr model. Temperature effects on polymer-stabilized blue phase or optically isotropic liquid crystal displays are also investigated. Through the measurement of voltage dependent transmittance under different temperatures, an analytical approximation between Kerr constant and temperature is proposed for the first time. In addition, we have demonstrated a polymer-stabilized BPLC mixture with a large Kerr constant K~13.7 nm/V^2 at 20 ^{o}C and λ=633 nm. Finally, the optical response time and its temperature dependency is discussed and validated through experiment and model. In all aspects, good agreement between experiment and physical model is obtained. These models will undoubtedly benefit us with more understanding of the material performance. The study of basic electro-optic properties of blue phase liquid crystals will provide useful guidelines to the optimizations of BPLC materials for practical applications.

CHAPTER 3: DEVICE PHYSICS OF BLUE PHASE LIQUID CRYSTAL DISPLAYS

As above mentioned, polymer-stabilized blue phase liquid crystals exhibit several attractive features for display and photonic applications but also have some technical challenges. In this chapter, to better understand the underlying operation mechanisms, we will explore the device physics.

3.1 Blue Phase Liquid Crystal Displays with In-Plane-Switching Fields

Typically, for display applications, the LC layer is sandwiched between two crossed linear polarizers. The operation mechanism of a polymer-stabilized blue phase liquid crystal display (BPLCD) is drastically different from conventional nematic LCDs in that the former is based on Kerr effect-induced isotropic-to-anisotropic transition while the latter relies on the anisotropic-to-anisotropic LC director reorientation. Moreover, the optic axis of the induced birefringence in BPLC is along the direction of the electric field. To achieve effective phase retardation, the induced birefringence should be parallel to the BPLC cell substrates, that is, a lateral electric field is desired. Among the present LCD modes, in-plane-switching (IPS) LCD can effectively generate horizontal electric fields; therefore, in blue phase LCD devices, IPS electrodes are commonly employed.

Figure 3.1 illustrates the basic operation principles of a BPLCD in a planar in-plane-switching (IPS) cell, where *w* is the electrode width and *l* is the electrode gap. When there's no electric field applied, the symmetric cubic structure in a polymer-stabilized BPLC appears to be optically isotropic. Therefore, the linearly polarized light passing the bottom polarizer experiences no phase retardation in the BPLC layer, thus it cannot pass the crossed analyzer.

When an electric field is applied, the BPLC becomes anisotropic according to the Kerr effect, thus, the linearly polarized light passing the bottom polarizer can pass the analyzer on the top.

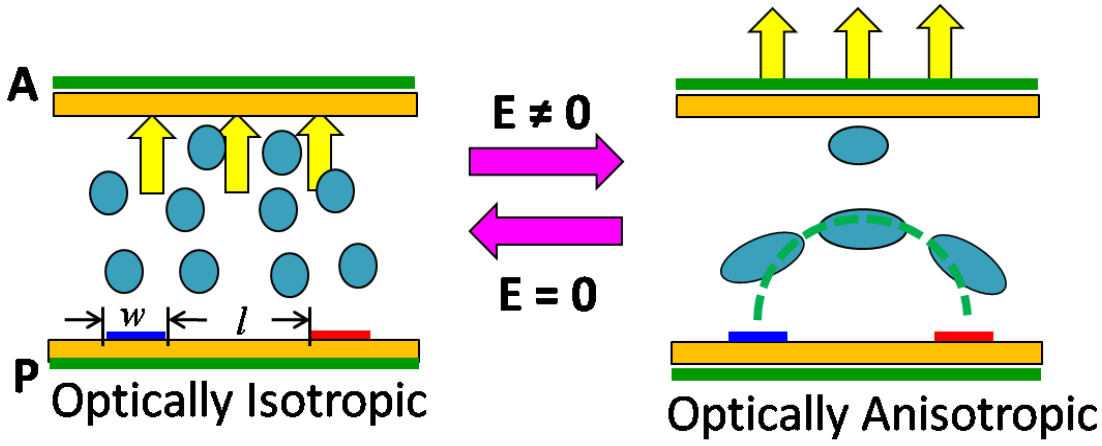

Figure 3.1 Operation principle of a BPLCD. Left: without electric field, BPLC appears to be optically isotropic; right: with electric field, BPLC becomes optically anisotropic.

The output transmittance of a uniaxial medium placed between two crossed linear polarizers is $T = T_0 \sin(2\phi)^2 \sin(\delta/2)^2$, where ϕ is the angle between optic axis of the uniaxial media and the absorption axis of the polarizer, $\delta = 2\pi d\Delta n/\lambda$ is the phase retardation of the uniaxial medium. The angle ϕ needs to be 45^o away from the linear polarizer absorption axis in order to obtain maximum transmittance. In other words, the induced Δn also needs to be along that direction to have a maximum transmittance. Moreover, to get the maximum phase retardation δ, the induced birefringence should also be along the horizontal direction parallel to the substrate surface. Therefore, the stronger horizontal fields will benefit.

3.2 Computational Analysis of IPS-BPLCDs

In this section we will introduce the computational model developed [53, 54] for characterizing the electro-optic properties of the BPLC materials with in-plane switching (IPS) cells [55]. Also will be investigated here are the dependence of BPLCD electro-optics on different parameters such as electrode configuration, LC birefringence, cell gap, Kerr constant and wavelength dispersion. The viewing angle performance will also be looked into.

Strictly speaking, to accurately compute the detailed molecular distribution of BPLCs in response to an external field, both Landau free energy and electric energy need to be considered, which turn out to be quite complicated [3, 27]. However, macroscopically the isotropic to anisotropic transition of BPLC can be described by Kerr effect. Thus, the electro-optic properties of a BPLCD can be simulated by computing the induced birefringence profile based on Kerr effect. The amplitude of the induced birefringence (Δn) can be characterized by Eq. (2.1), or to be more accurate, by the extended Kerr model in Eq. (2.2). For display applications, a BPLC cell is placed between two crossed linear polarizers. Without the applied voltage, each small blue phase unit is optically isotropic, having refractive indices identical along its principal coordinates. This leads to a very good dark state. When an electric field $\boldsymbol{E}$ is applied, birefringence will be induced by the electric fields and the refractive index ellipsoid will have its optic axis aligned along the direction of the $\boldsymbol{E}$ vector. The horizontal electric fields are in favor because they will induce phase retardation for the incident light.

Figure 3.2 shows the proposed flow chart of the numerical model for the BPLCD calculation. First, we compute the potential distribution Φ from solving the Poisson equation $\nabla(\nabla\cdot\varepsilon\Phi) = 0$ and then calculate the distribution of electric field $\boldsymbol{E}$ in the media. Based on the

obtained electric field, we calculate the induced birefringence distribution Δn from Eq. (2.1) and assign the local optic axis direction of each unit along the $\boldsymbol{E}$ vector. After obtaining the birefringence and optic axis distribution, we adopt the extended Jones matrix [56] to compute the related electro-optic properties, such as voltage-dependent transmittance curve (VT), viewing angle, and color shift, etc.

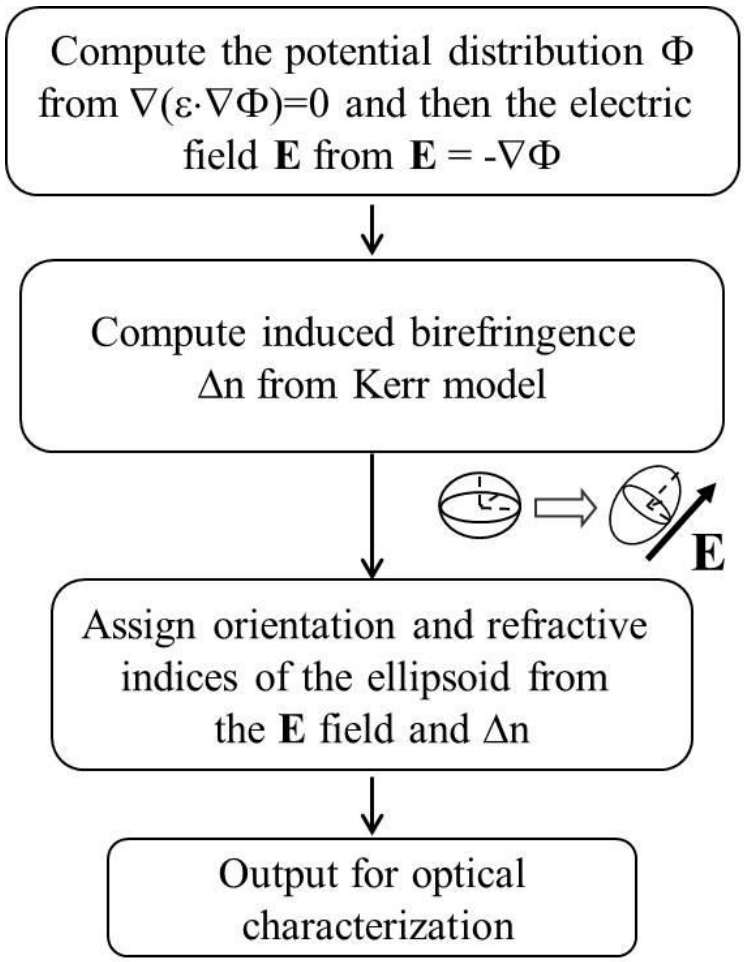

Figure 3.2 The flow chart of the BPLCD modeling based on Kerr effect.

3.2.1 Electric Field Effect

Electrode structure affects the driving voltage and peak transmittance of an IPS BPLC cell. The induced birefringence of BPLC is proportional to E^2, and is influenced by both amplitude and direction of the electric field. Since the induced refractive index ellipsoid is along the electric field direction, for the BPLC cell at 45^o away from the polarizer's transmission axis, a horizontal electric field is needed to provide phase retardation for intensity modulation. Thus, in an IPS cell the transmittance is mainly contributed from the spacing area where the electric field is more horizontally distributed. There is only a tiny and negligible contribution on top of the pixel and common electrodes where the electric field is mostly in vertical direction.

Figure 3.3 depicts the transmittance curves at different voltages of the IPS BPLC cell at different positions. The high transmittance occurs mainly at the spacing area between electrodes. The incident wavelength is 550 nm and Kerr constant is K~12.68 nm/V^2. In the IPS BPLC cell, even at a high voltage (V~52 V_{rms}) the transmittance above electrodes is still negligible. This is because the optic axis of the refractive index ellipsoid on top of the electrodes is almost perpendicular to the electrodes and thus parallel to the normal incident light. Different from the IPS BPLC cell, in a conventional nematic IPS cell, the horizontal rotation of LC molecules between the pixel and common electrodes will produce a weak in-plane LC rotation above the electrode surfaces because the LC is a continuum material. This in-plane LC rotation will also contribute to a weak transmittance above electrodes that adds to the overall transmittance. Nevertheless, in the IPS BPLC cell the induced Δn above the electrode surfaces will only act on the oblique incident light to make the viewing angle more symmetric.

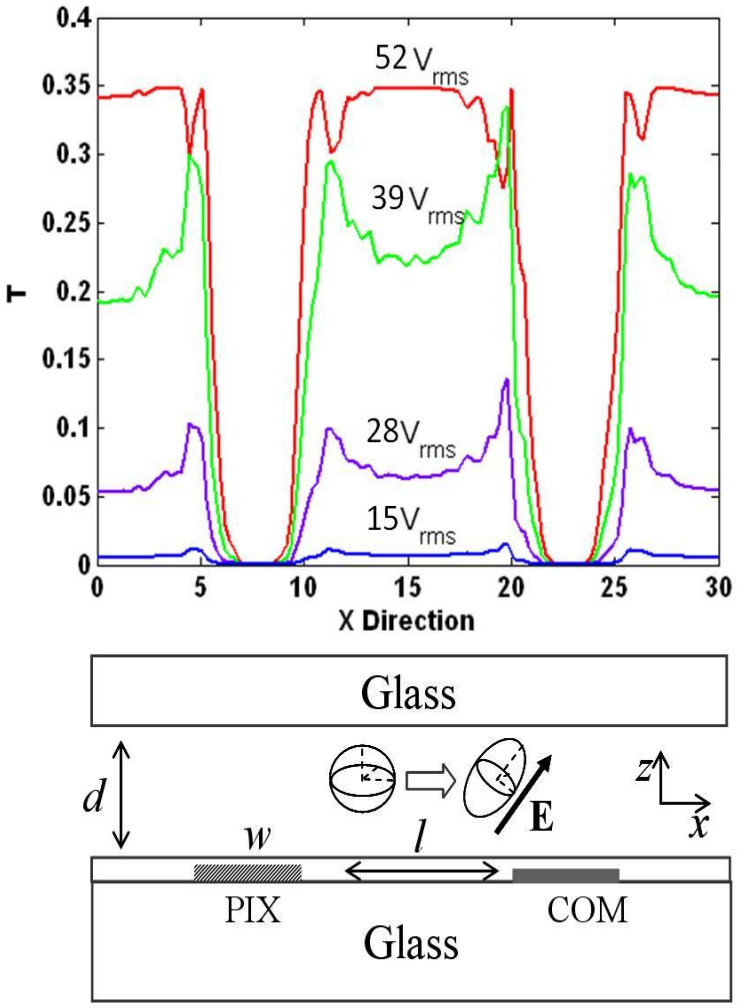

Figure 3.3 Transmittance curves at different voltages of the BPLCD in a 10-μm IPS cell (w=5 μm and l=10 μm) at λ=550 nm (the maximum transmittance from parallel polarizers is 34.83%).

The electrode dimensions affect the electro-optic properties of the blue phase LC device. Figure 3.4 shows the voltage-dependent transmittance curves of IPS BPLC cells with different electrode width w and spacing width l [24]. The Kerr constant employed in the simulation is K=12.68 nm/V^2.

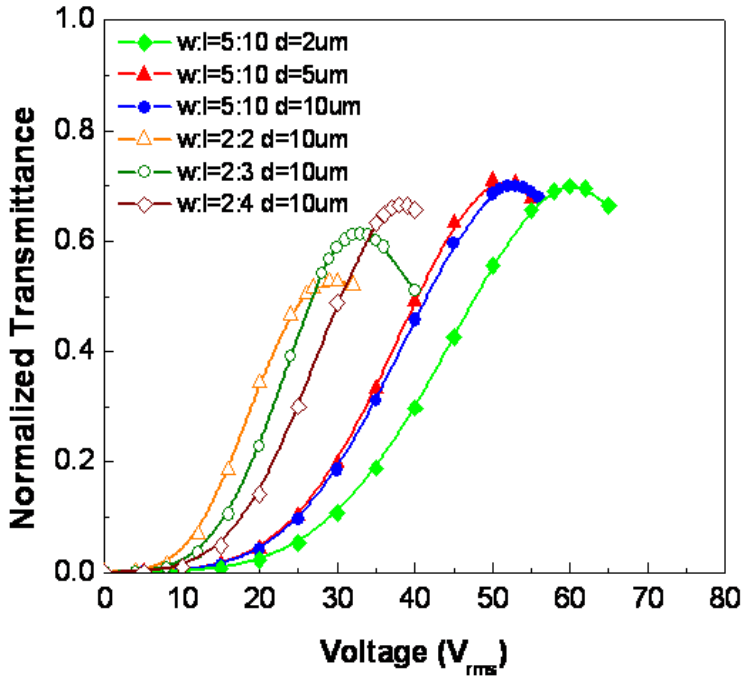

Figure 3.4 Voltage-dependent transmittance of BP IPS cells with different w-*l* ratios and cell gaps.

First, let us compare the three 10-μm thick IPS cells with electrode width *w*=2 μm and spacing *l* varying from 2 μm to 4 μm (open squares, triangles, and circles). Both on-state voltage and peak transmittance decrease as the electrode spacing decreases. For the same electrode width, a smaller electrode spacing *l* results in a stronger horizontal electric field, so the driving voltage is lower. However, the smaller electrode spacing reduces the effective area of the horizontal field from which the transmittance is gained; therefore the optical efficiency is also lower. We further compare the 10-μm IPS cell with electrode width *w*=5 μm and spacing *l*=10 μm (IPS 5-10, blue filled circles) with the 10-μm thick IPS cell with electrode width *w*=2 μm and spacing *l*=4 μm (IPS 2-4, dark red open squares). They have the same *w*-*l* ratio. The lower driving voltage results from a stronger electric field due to a smaller electrode spacing (*l*=4 μm). IPS 5-10 has a slightly higher peak transmittance than IPS 2-4. This can be explained by the depth of the electric field

penetrating from the bottom electrodes to the LC layer. According to the Poisson equation $\nabla^2\Phi=0$, the penetrating depth is proportional to the dimensional size ($w+l$). Thus, the electric field penetrates deeper into the LC layer in the IPS 5-10 cell than IPS 2-4, resulting in a higher induced birefringence and peak transmittance. As described earlier, the area on top of the electrodes in BPLC cells do not contribute to the transmittance because the electric field is primarily longitudinal. However the conventional nematic IPS cell, unlike the BPLC, has a weak in-plane LC rotation above the electrodes that enhances the optical efficiency. As a result, the overall optical transmittance of BP LCDs is slightly lower than that of conventional IPS LCDs

3.2.2 Induced Birefringence Distribution and Cell Gap Effect

The transmittance of a nematic IPS cell is largely affected by the cell gap, since the phase is continuously accumulated along the cell gap. However, in an IPS BPLC cell the transmittance is quite insensitive to the cell gap. As illustrated in Figure 3.4, for the electrode dimensions w=5 μm and l=10 μm (IPS 5-10), the transmittance remains almost the same for cell gap d=5 μm and d=10 μm.

To better understand the transmittance and electric field distribution, we plot the induced birefringence distribution at on-state voltage (where maximum transmittance occurs) in Figure 3.5 and Figure 3.6 for IPS 5-10 and IPS 2-4 (both of them have a cell gap of 10 μm), respectively. Two different Kerr constants are employed for comparison: K_a=1.268 nm/V^2 and K_b=12.68 nm/V^2. Here Δn denotes the overall induced birefringence by the applied electric field, regardless of the field direction; Δn_{eff} is the effective birefringence for the normal incident light that contributes to the phase change. For IPS 5-10, the on-state voltage (V_{on}) is 167 V_{rms} at K_a and 53 V_{rms} at K_b; while for IPS 2-4, the on-state voltage is 121 V_{rms} at K_a and 38 V_{rms} at K_b. We can see

from the plot that with the same electrode dimension, the Kerr constants do not affect the on-state induced birefringence.

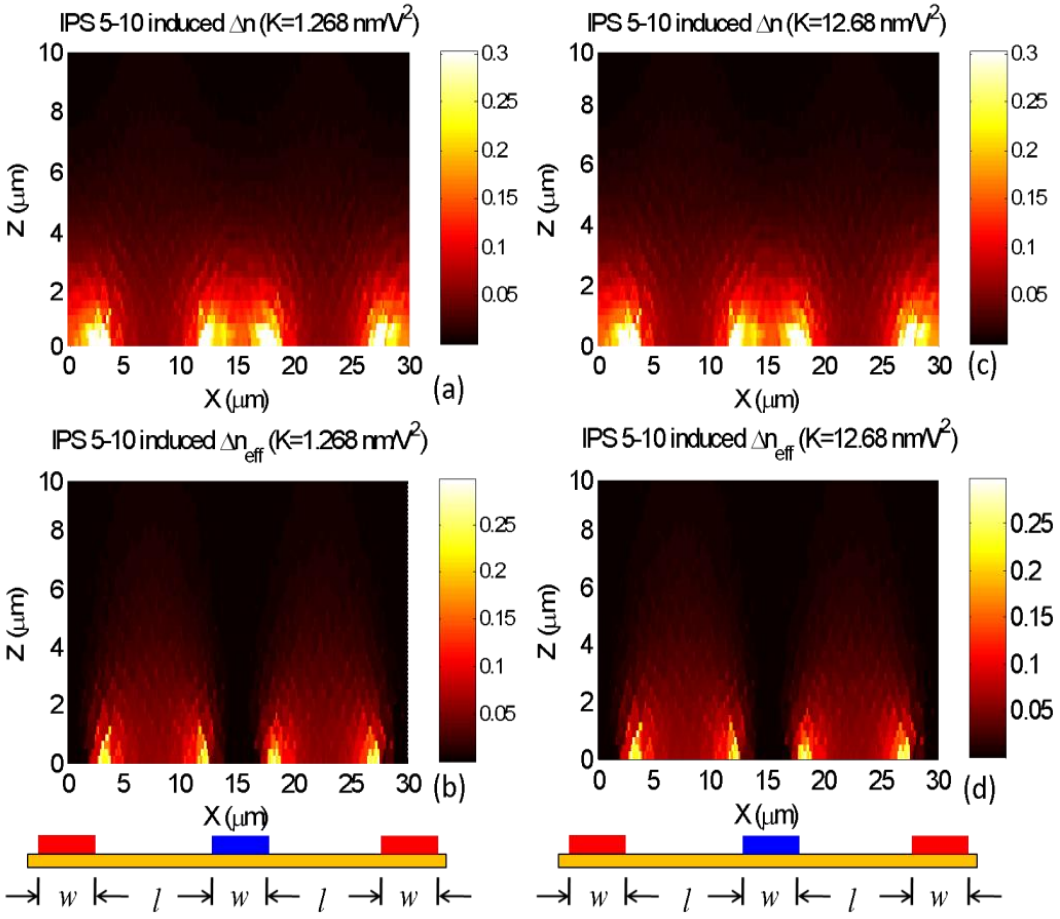

Figure 3.5 Spatial profiles of induced birefringence and effective birefringence in IPS cells: w is the electrode width, l is the spacing width. (a) overall induced Δn of IPS 5-10 at K_a, (b) induced Δn_{eff} of IPS 5-10 at K_a, (c) overall induced Δn of IPS 5-10 at K_b, (d) induced Δn_{eff} of IPS 5-10 at K_b. (K_b=10 K_a =12.68 nm/V^2)

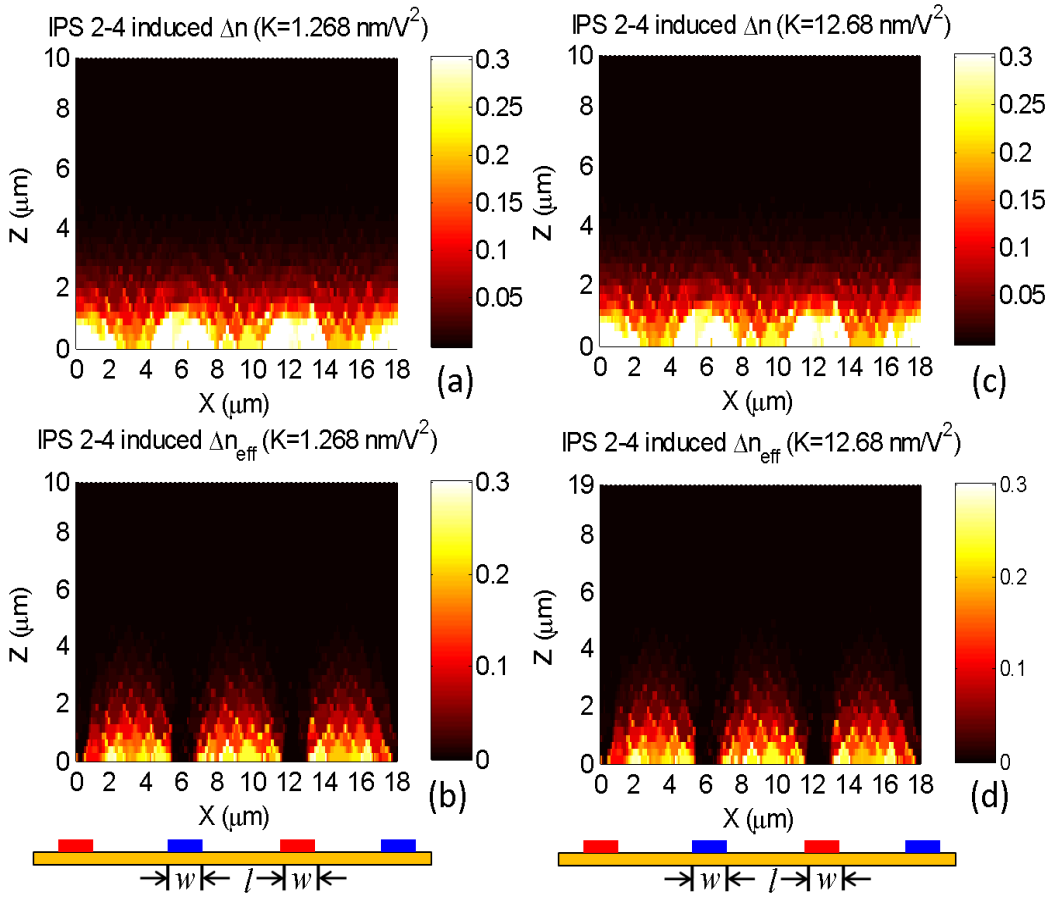

Figure 3.6 Spatial profiles of induced birefringence and effective birefringence in IPS cells: w is the electrode width, l is the spacing width. (a) overall induced Δn of IPS 2-4 at K_a, (b) induced Δn_{eff} of IPS 2-4 at K_a, (c) overall induced Δn of IPS 2-4 at K_b, (d) induced Δn_{eff} of IPS 2-4 at K_b. (K_b=10 K_a=12.68 nm/V^2)

From Figures 3.5(a), 3.5(c), 3.6(a) and 3.6(c), on top of the electrodes, although Δn is comparatively large and extended deep into the LC layer, it is induced by the vertical electric field which does not contribute to the transmittance. This is also verified that in Figures 3.5(b), 3.5(d), 3.6(b) and 3.6(d) where Δn_{eff} is almost zero on top of the electrodes. The induced birefringence at the spacing area is not only very small but also decays fast with the cell gap.

Thus, as long as the cell gap is larger than the penetrating depth in the vertical direction, the transmittance will be insensitive to the cell gap. The tiny difference between the 5-μm and 10-μm cells of IPS 5-10 structure in Figure 3.4 may come from the passivation layer. It has a much smaller dielectric constant than the LC composite, making the electric energy more concentrated in the LC layer of the 5-μm cell. If the cell gap is smaller than the effective penetrating thickness, for example, when the IPS 5-10 has a cell gap of d=2 μm, we find in Figure 3.4 that the on-state voltage is higher. In this case, a larger electric field is needed to gain the same phase change in a smaller cell gap. The feature of cell gap insensitivity provides a large tolerance to the large panel LCD fabrication since the uniformity of the cell gap is fairly difficult to control.

As shown in Figures 3.5 and 3.6, IPS 5-10 and IPS 2-4 differ in that the latter has a shorter penetrating depth, a faster decay in birefringence, and its amplitude near the electrode bottom is larger. This is actually the result of the electric field concentration difference, and again it explains why the IPS 2-4 structure yields a lower driving voltage and a slightly lower transmittance.

3.2.3 Operating Voltage and Kerr Constant

The operating voltage of a BPLCD is primarily governed by the induced birefringence which in turn is dependent on the Kerr constant of the LCs and the electric field strength. On one hand, investigation on the device structure unveils influence from the electric field to the driving voltage and the transmittance; on the other hand, from the material side the LC parameters directly affect the display performance. In this section, we analyze the Kerr constant effect.

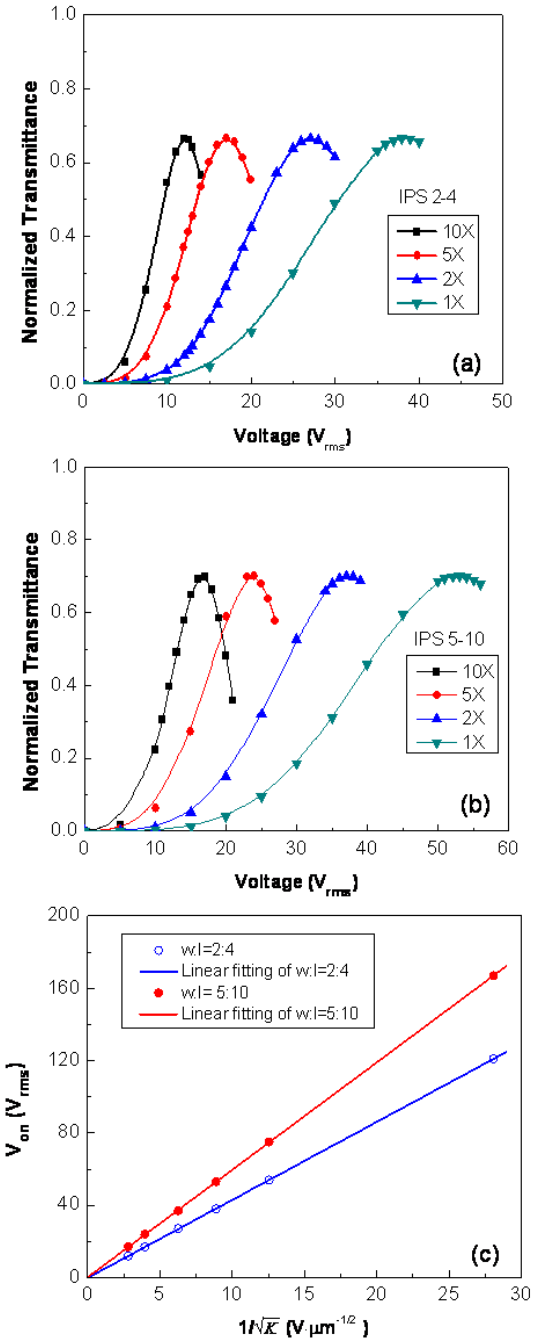

Figure 3.7 (a) VT curves with different Kerr constants for IPS 2-4, (b) VT curves with different Kerr constants for IPS 2-4, (c) linear plot between on-state voltage and $1/\sqrt{K}$.

Figures 3.7(a) and 3.7(b) are the plots of simulated voltage-transmittance curves with K_1=12.68 nm/V^2, K_2=2K_1, K_3=5K_1 and K_4=10K_1 for two IPS structures: w=2 μm, l=4 μm, and w=5 μm, l=10 μm. For both structures, the peak transmittance does not change with K. Figure 3.7(c) depicts the on-state voltages for the above four K values as well as K_5=0.1K_1 and K_6=0.2K_1. Surprisingly, the on-state voltages exhibit a linear relationship with $K^{-1/2}$, although the electric field is quite nonuniform. The red and blue lines are the linear fittings with the following equation:

$$V_{on} = A \cdot \frac{1}{\sqrt{K}}, \qquad (3.1)$$

The proportionality constant A for IPS 2-4 and IPS 5-10 is A_1=4.31 μm$^{1/2}$ and A_2=5.94 μm$^{1/2}$, respectively. With the same Kerr constant, the on-state voltage of IPS 2-4 is ~40% lower than that of IPS 5-10, but its transmittance is slightly (~3%) lower. As abovementioned, the Kerr constant represents the influence from the material side to the driving voltage, while A represents the effect from the device design. Larger Kerr constant and smaller A will lead to a lower operating voltage. For low power TFT-LCDs, it is highly desirable to have V_{on}<10 V_{rms}. To achieve this goal, from Figure 3.7 we need to continue to improve the Kerr constant of the BPLC material and optimize the electrode configuration.

As referred to Fig. 3.5, although the K value may not be the same, for a given electrode structure, the induced birefringence distribution at its corresponding on-state voltage is basically the same, and thus results in a same peak transmittance. According to Eq. (2.1), at a given wavelength the induced birefringence is directly related to KE^2. Then, we can conclude that for a given IPS electrode dimension operating at the on-state voltage, if the electric field E is uniform in the IPS cell, then KE^2 will be a constant. As $E=V/L$, KV^2 is also a constant, and Eq. (3.1) holds

for this straightforward case. However, in a real IPS structure, E is not uniform spatially. It is surprising to see that the linear relationship as shown in Eq. (3.1) is still valid according to our simulation results. In an IPS cell, the KE^2 value may differ at different areas because of the E distribution, but it remains a constant for the same area in the cell regardless of the variance of K. The voltage V is related to the electric field E as $E = \partial V / \partial L$ (∂L is the infinitesimal change in distance), as long as the cell is operated under the on-state voltage, the KV^2 value would stay constant for the same area of the cell despite of the K variation.

From Eq. (3.1), the operating voltage of a BPLC device is governed by material (thru K) and device configuration (thru A). We have also validated the assumption experimentally.

In Chapter 2, we have discussed the temperature effect and obtained the voltage dependent normalized transmittance curves of the IPS LC composite cell measured from 15 ^{o}C to 37.5 ^{o}C. From the experimental data shown in Figure 2.2, we obtain the on-state voltage at different temperatures. We then plot V_{on} against the inverse of the square root of Kerr constant. Results are shown in Figure 3.8. Indeed, a straight line passing through the origin is obtained. From the slope, we find A=6.07 μm$^{1/2}$ for our IPS structure.

Similarly, using the same IPS structure but with different BPLC material (Chissco material), we obtain the on-state voltage at different temperatures in Figure 2.5 and then plot V_{on} against $1/\sqrt{K}$ in Figure 3.9. From the slopes in Figure 3.9, we find A=5.92 μm$^{1/2}$. This result agrees well with the same IPS structure but with a low-K BPLC material in Figure 3.8, in which A=6.07 μm$^{1/2}$. From Eq. (3.1), both device configuration (thru A) and large K material play important roles for lowering the operating voltage. For the first time, the theoretical prediction of Eq. (3.1) is validated experimentally.

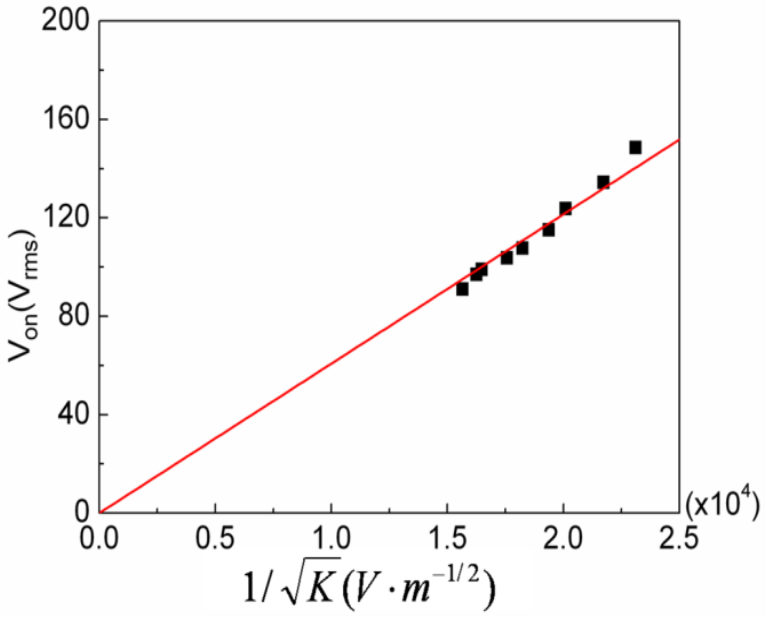

Figure 3.8 Linear fit of V_{on} vs. $K^{-1/2}$ according to Eq. (3.1) with A=6.07 μm$^{1/2}$.

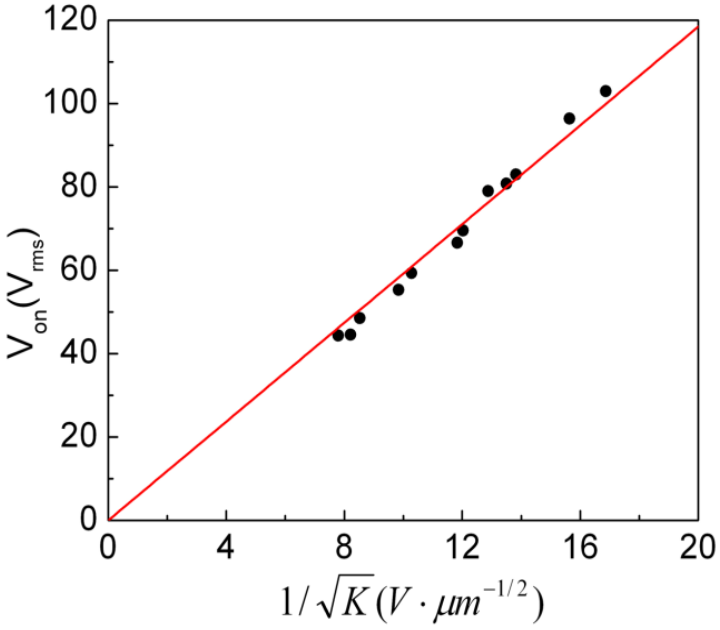

Figure 3.9 Linear fit of V_{on} vs. $1/\sqrt{K}$ according to Eq. (3.1) with A=5.92 μm$^{1/2}$.

3.2.4 Wavelength Dispersion

For BPLC, or more generally the optically isotropic liquid crystals, the Kerr constant K is wavelength dependent and can be described by the single-band model as [39, 57]

$$\lambda K \approx G \frac{\lambda^2 \lambda^{*2}}{\lambda^2 - \lambda^{*2}} \tag{3.2}$$

Here λ^* is the mean resonance wavelength and G is a proportionality constant. For E-7 type LC mixtures (Δn~0.22), λ^*~200-250 nm due to elongated π-electron conjugation [39]. In principle, from Eq. (3.2) we could obtain G and λ^* values by measuring the Kerr constant of the BPLC cell at two wavelengths.

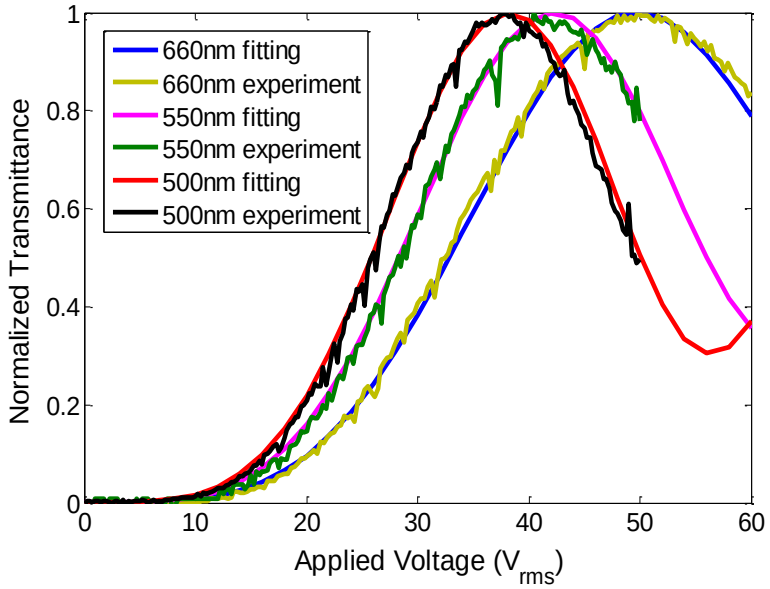

Figure 3.10 Measured VT curves and fittings of the BPLC in a 10-μm IPS cell with electrode width w=10 μm and spacing l=10 μm at different wavelengths.

In an experiment, we prepared a BPLC cell in the IPS structure using Chisso's JC-BP01M BPLC material. The IPS cell has an electrode width of 10 μm and gap width between the

electrodes is also 10μm. The cell gap is 10 μm. We have measured the voltage-dependent transmittance (VT) curves at room temperature (~22^{o}C) at 500nm, 550nm, and 650nm. The driving frequency is 100 Hz. By fitting the VT curves with the model we have established, we can obtain the parameters for the above three wavelengths. Figure 3.10 shows the measured VT curves and fittings of the BPLC at different wavelengths. From the parameters obtained, we have also deduced the parameters for other wavelengths in Table 3.1.

Table 3.1 Fitting parameters for BPLC at different wavelengths.

G (nm^{-2})	λ* (nm)	Es (V/μm)	λ (nm)	K (nm/V^2)	Δn_s
2.8	218	4.2	450	21.9	0.174
2.8	218	4.2	500	18.6	0.164
2.8	218	4.2	550	16.3	0.158
2.8	218	4.2	633	13.5	0.151
2.8	218	4.2	650	13.1	0.15
2.8	218	4.2	660	12.8	0.149

As we can see from the figure and the data table, the Kerr constant decreases when the wavelength increases. Compared to the nematic IPS or FFS cell, the IPS BPLC cell exhibits larger color dispersion. In a conventional nematic IPS or FFS cell, the on-state LC profile consists of two connected twist-nematic (TN) cells with reserve twist sense [58], thus there is a self-compensation for wavelength dispersion from this special two-TN-cell profile. However, in the IPS BPLC cell, the transmittance originates from pure phase retardation effect, similar to a vertical alignment (VA) cell. A shorter wavelength has a larger Kerr constant to get a larger $\Delta n/\lambda$

value, which will result in a lower on-state voltage. However, different from the nematic VA cell, the induced birefringence (bright state) of the IPS BPLC cell has multi-domain structure originating from the electric field profiles. In an IPS cell, horizontal fields dominate between electrode gaps, and vertical components dominate above the electrode surfaces. Because each local induced birefringence also aligns with the electric field, the electric field-induced refractive ellipsoids in the whole cell will gradually align from vertically to horizontally starting from the electrode center to the electrode gap region. This multi-domain profile leads to a more symmetric and wider viewing angle, as will be discussed later.

3.2.5 Viewing Angle

When no voltage is applied, the BPLC is macroscopically optically isotropic. The LC index ellipsoid is like an ideal sphere that has a very good dark state. As a result, the dark-state light leakage only occurs at an off-axis incidence that merely comes from the effective angle deviation between two crossed linear polarizers, i.e., two crossed linear polarizers at a normal incidence is no longer perpendicular to each other at an oblique incidence. At the voltage-on state, although electric field induces birefringence and the LC index ellipsoid is elongated, the overall cubic symmetry of the BPLC is not changed. This again leads to a symmetric view of the LCD. Due to these features which are different from conventional nematic liquid crystals, the iso-brightness contour of the IPS BPLC cell is more symmetric. Another advantage is that the liquid crystal alignment and rubbing which may cause light leakage for conventional LCDs do not exist here.

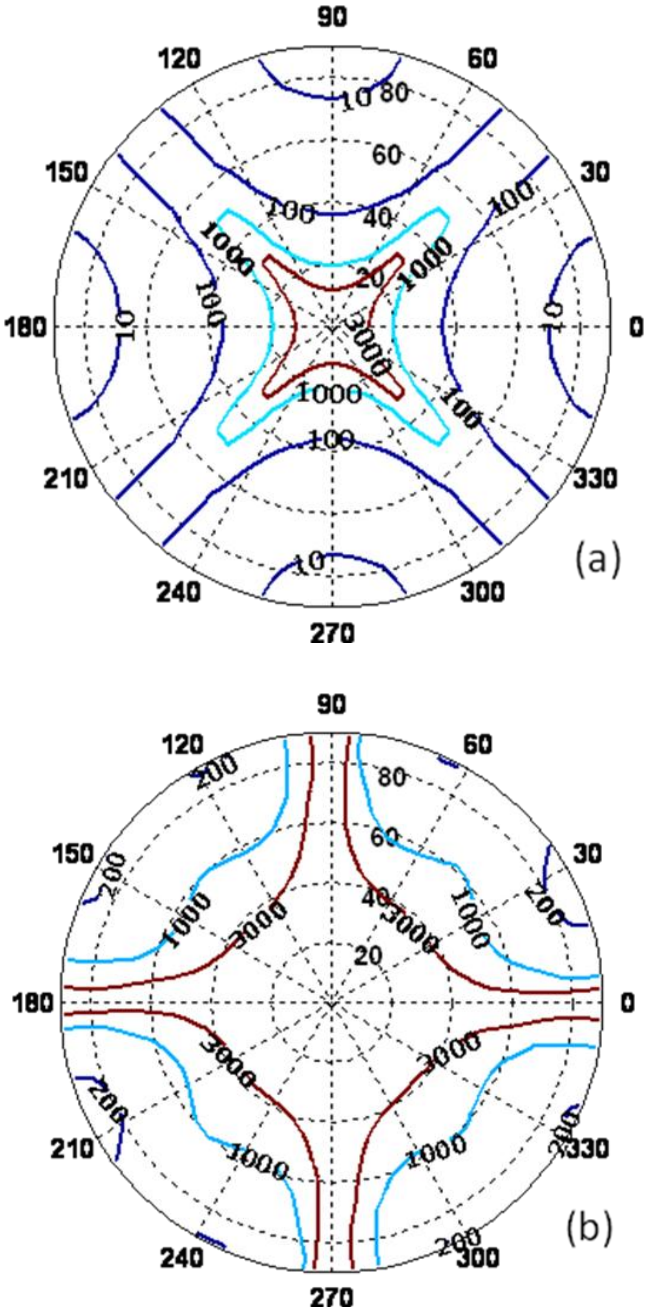

Figure 3.11 Simulated isocontrast plots of the IPS BPLC cell: (a) without compensation films, and (b) with a biaxial compensation film. The biaxial film parameters are: N_z =0.5, $R_0=(n_x-n_y)\cdot d=\lambda/2$. BPLC IPS cell parameters are: d=10 μm, w=5 μm, l=10 μm and λ=550 nm.

Figures 3.11(a) and 3.11(b) are the isocontrast plots of an IPS BPLC cell at λ=550 nm, with electrode width w=5 μm, spacing l=10 μm and cell gap d=10 μm. As expected, the viewing angle is more symmetric even using an IPS structure with merely 2D lengthwise strips. To compensate the viewing angle, both uniaxial films and biaxial films can be employed to suppress the light leakage at dark state and expand the viewing angle. The biaxial film compensated isocontrast plot is shown in Figure 3.11(b). The biaxial film employed has the following parameters: N_z =0.5 and $R_0 = (n_x - n_y)\cdot d = \lambda/2$ [59]. The cell dimensions used in simulation are: electrode width w=5 μm, spacing width l=10 μm, and λ=550 nm. We find that the contrast ratio over 1000:1 can be expanded to ~55^o-66^o with compensation films. The viewing angle of this simple IPS BPLCD is comparable to that of a conventional four-domain IPS structure with zigzag electrodes.

3.3 Summary

In this chapter, we have discussed the device physics of blue phase LCDs. For display applications, we have introduced an in-plane-switching (IPS) structure with lateral fields to induce the effective birefringence. The computational model was developed to characterizing the Kerr effect in BPLC cells. With this numerical calculation model, parameters affecting the electro-optics of BPLCDs in IPS structures, such as electric field effect, induced birefringence distribution, cell gap effect, operating voltage and Kerr constant effect, and wavelength dispersion are investigated. Viewing angle is also discussed. The study of the device physics can provide guidelines for future device optimization.

CHAPTER 4: DEVICE CONFIGURATION OPTIMIZATIONS OF BLUE PHASE LIQUID CRYSTAL DISPLAYS

Blue phase exhibits some great features of submillisecond response time, wide viewing angle, no alignment layer needed and cell gap insensitivity which opens a new window for display applications. However, there are still technical challenges to be overcome, among which high driving voltage is the most severe one since it increases the power consumption, and disables the a-Si TFT driving. Other issues include color shift, hysteresis, wavelength dispersion, long term stability, residual birefringence, and voltage holding ratio, etc. To solve these problems, developing new BPLC materials and optimizing device configurations are both very important. In this chapter, we will focus on the optimization of BPLCD through device configuration modification.

4.1 Low Voltage BPLCDs

To successfully drive blue phase LCs to realize different grayscales, a strong electric field along horizontal direction is desired. Therefore, the most effective driving electrodes currently available should be IPS switching electrodes. However, in a conventional IPS electrode configuration, the electric field is confined near the surface, and only the LC molecules in this shallow region contribute to the induced birefringence. As a result, the required voltage is high and transmittance is low. As shown in Figure 2.5 from Chapter 2, even with a large Kerr constant of 13.7 nm/V^2 (Chisso JC-BP01M), the on-state voltage is still as high as ~50 Volts at room temperature. 50 Volts is too high for amorphous-silicon thin-film transistors (a-Si TFTs) addressing. Therefore, there is an urgent need to address this critical issue of high driving voltage.

From material side, developing BPLC materials with larger Kerr constant can

significantly lower the operating voltage. In addition to material, device configuration also plays a significant role for reducing the operating voltage. There has been various electrode configurations proposed to generate strong and deep electric fields for lowering the operating voltage of BPLC devices, such as wall-shape electrode and corrugated electrode structure as shown in Figure 4.1 and Figure 4.2 [60, 61]. For both structures, the driving voltage can be lower because the incident light can experience a uniform electric field. However, their fabrication process is comparably complicated and difficult to realize.

In this chapter, we will discuss our proposed electrode configurations. With an optimized electrode structure, a larger horizontal electric field component and better uniformity across the horizontal direction are achieved. Therefore, the operating voltage can be dramatically reduced. Reducing operating voltage is critical to BPLC device as it will enable a-Si TFT addressing and save power consumption. In this way, it will effectively accelerate the emergence of BPLCD.

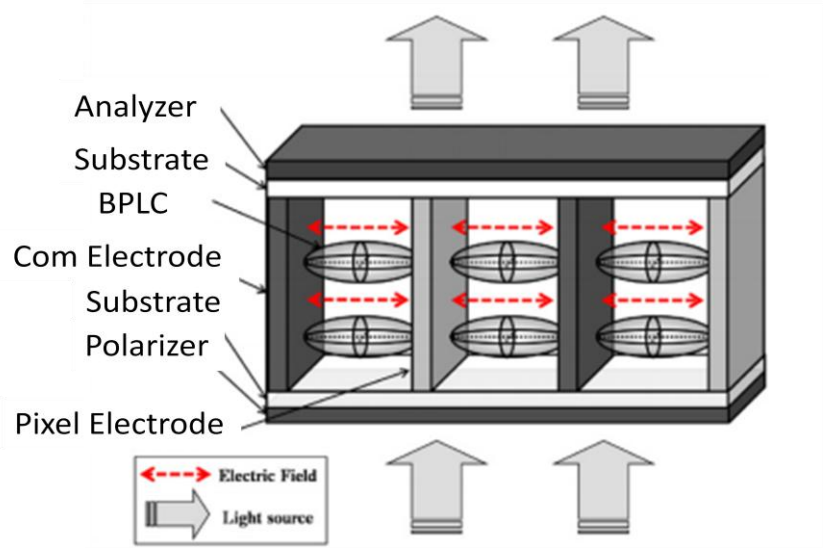

Figure 4.1 Cross-section view of BPLCD structure with wall-shape electrodes.

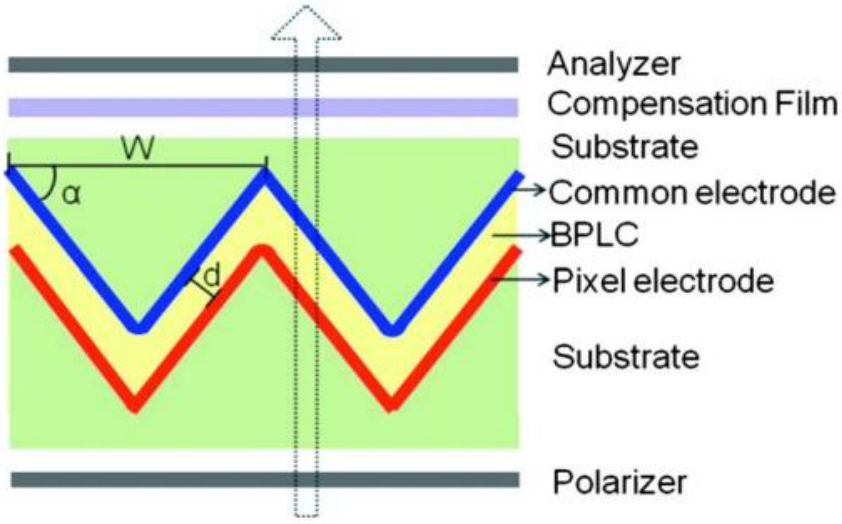

Figure 4.2 Cross-section view of BPLCD structure with corrugated driving electrodes.

4.1.1 BPLCDs with FFS Structure

Aside from IPS structure, fringing field switching (FFS) structure [55] is also widely employed in wide-view nematic LCDs. Figure 4.3(a) is the typical FFS electrode configuration. Electrode dimension in a FFS cell is distinguished by the electrode width *w* and the gap distance *g* between two electrodes in Figure 4.3(a). The basic structure of FFS is similar to IPS except for the much smaller electrode gap of *l*. In the FFS structure, both *w* and *g* are smaller than the cell gap. In IPS cell, horizontal electric field is dominant between the electrodes. However, in the FFS mode, when $l<d$, the fringing field exists above the electrodes. The fringing fields are able to reorient the LC directors above the electrodes. Therefore, for nematic LC with a FFS mode, the transmittance is higher.

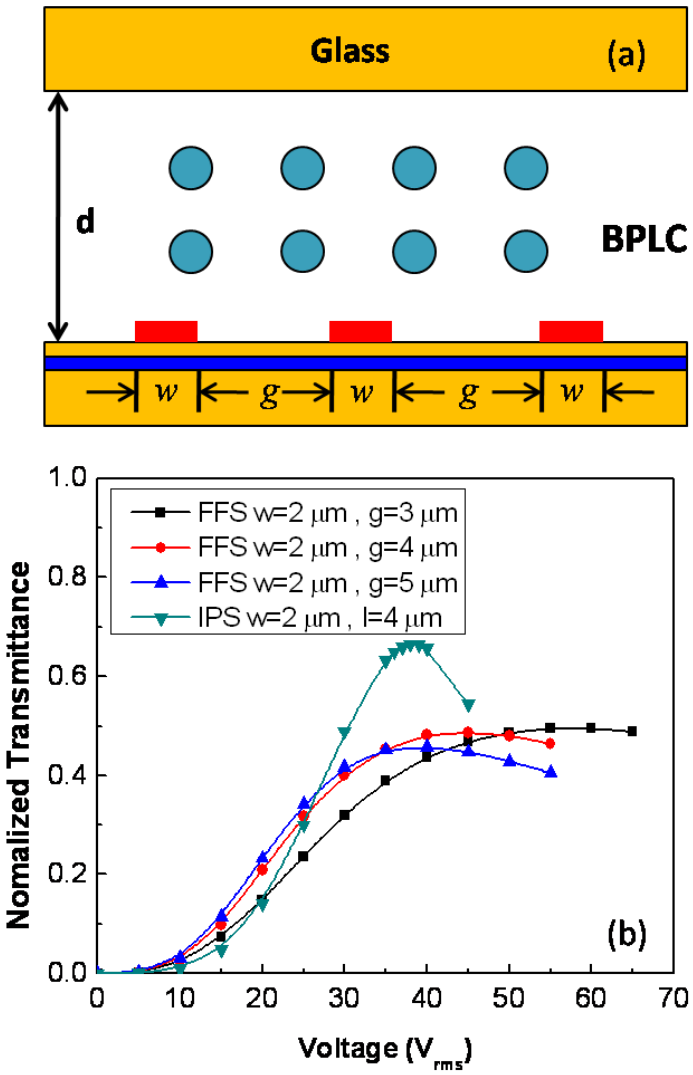

Figure 4.3 (a) A FFS cell structure, and (b) voltage-dependent transmittance curves for IPS and FFS cells with different electrode dimensions. Cell gap is 10 μm for all the curves.

We have simulated the BPLC with FFS electrode structure in Figure 4.3(b). If we compare the FFS structure with different *w*:*g* ratios under the same cell gap *d*=10 μm, curves in Figure 4.3(b) demonstrate the trend that the smaller the *w*:*g* ratio, the lower the on-state voltage and the faster the transmittance increases at a low voltage. This is because with the same

electrode width *w*, a larger gap *g* provides a deeper penetration of the electric field in the LC layer which helps to lower the operation voltage.

In Figure 4.3(b), IPS BPLC has much higher optical efficiency at the on-state voltage than the FFS structure. As introduced before, IPS provides more horizontal electric field in the spacing area, while FFS structure exerts a strong vertical field. In the FFS cell, the vertical field is in favor to the reorientation of nematic LCs on top of the electrodes for enhancing transmittance, but does not contribute to the birefringence we need in BPLCs. However, at low operating voltages, such as 10-25 V_{rms}, the transmittance of the FFS structure is higher and increases faster than that of the IPS structure. The strongest horizontal electric field is present at the edges of electrodes but decreases to minimum at the center of the gap between two electrodes. From the potential distribution in a FFS cell, the electric field at electrode edge is much stronger than that in an IPS cell. It can quickly rotate the LCs, so that the transmittance in FFS rises faster than that of IPS cell in the low voltage regime. As the voltage increases, the horizontal field in IPS cell becomes stronger than FFS cell so that FFS cannot compete with IPS cell for the peak transmittance. Therefore, FFS offers a steeper transmittance at low voltage but saturates at a much lower transmittance than IPS (Figure 4.3(b)). This phenomenon has been confirmed in our experiment. Current a-Si TFT technology can only carry a low voltage at ~15-20V_{rms}, in this case, compared to an IPS structure the FFS structure is in favor as it provides a higher transmittance at low voltage side.

4.1.2 BPLCDs with Double-Penetrating Fringing Fields

Figure 4.4(a) depicts a traditional planar IPS cell employed in BPLCDs; Figure 4.4(b) shows the proposed device structure with an etched bottom substrate. The glass substrate

between the electrodes is etched with a depth *h*. In this design, the fringe fields penetrate into both sides of the substrate. As a result, the BPLC molecules filled in the etched part of the substrate also contribute to phase retardation so that the driving voltage will be lowered [62].

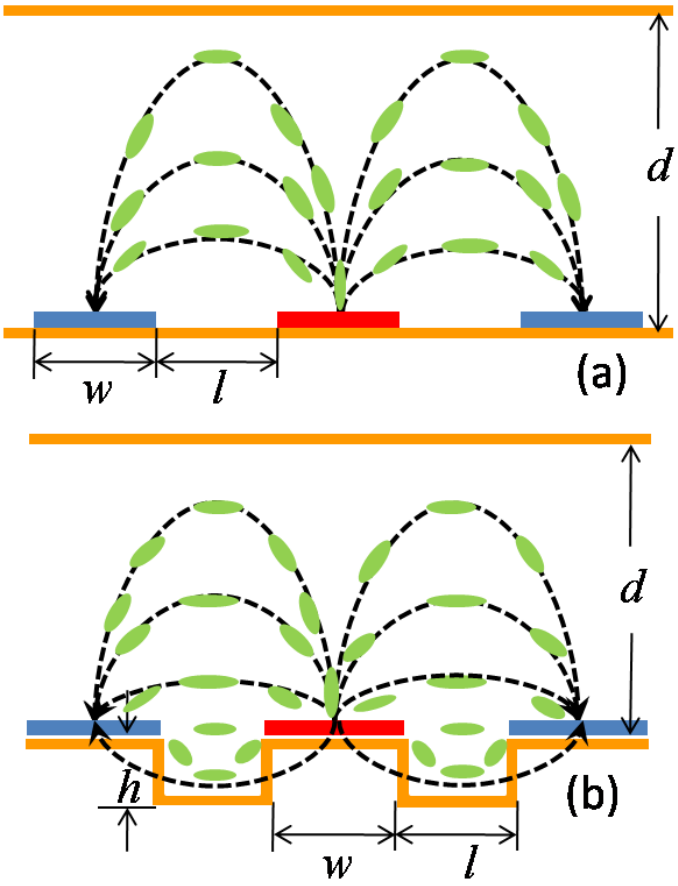

Figure 4.4 (a) BP LCD with conventional IPS structure and (b) BP LCD with double-penetrating fringe fields.

To evaluate the performance of the proposed structure, we calculate the voltage-dependent transmittance (VT) curves with the simulation described in Chapter 3. The Kerr constant is K=12.68 nm/V^2 (λ=550 nm) and the refractive index of the host LC is 1.5. The dielectric anisotropy is assumed to remain unchanged under different voltages. The transmittance is normalized to that of two parallel polarizers (34.83%).

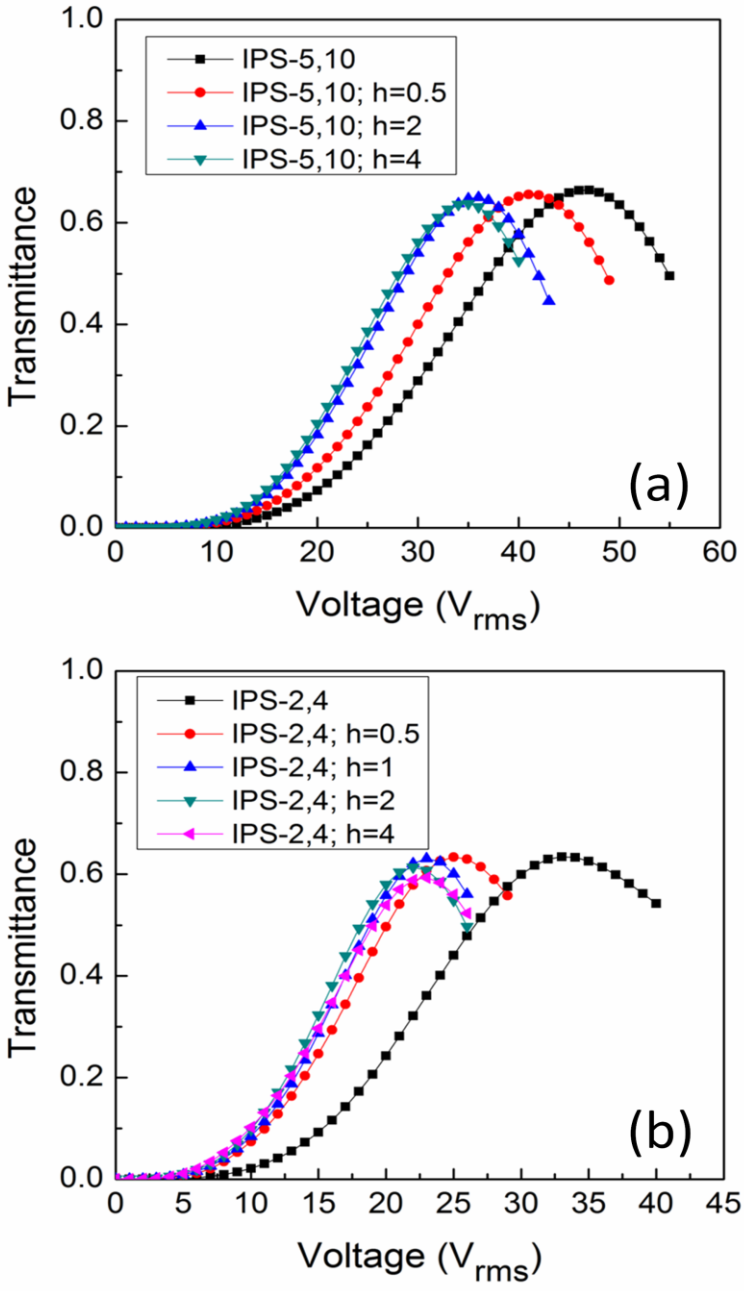

Figure 4.5. Simulated VT curves of the BPLC cell with etched (a) IPS 5-10 substrate and (b) IPS2-4 substrate. λ=550 nm; h (in μm) is the etching depth.

Figure 4.5 shows the simulated VT curves (λ=550 nm). Figure 4.5(a) is for IPS 5-10 (w=5 μm, l=10 μm, and d=10 μm). From previous studies, the operating voltage and

transmittance are insensitive to the cell gap, as long as d>3 μm. The line with the black squares is the planar IPS structure without etching; others are with a certain etching depth (h) on the substrate. The voltage at the peak transmittance (V_p) for the planar IPS 5-10 is ~47 V_{rms}. As the etching depth increases, V_p decreases. When the etching depth exceeds ~2 μm, V_p drops by ~26% and saturates at ~35 V_{rms}. The peak transmittance of the etched structure stays almost the same as that of planar IPS.

Similarly, Figure 4.5(b) shows the simulated VT curves at λ=550 nm for IPS2-4 (w=2 μm, l=4 μm, and d=10 μm). The line with black squares represents the planar IPS structure without etching; others are with a certain etching depth (h) on the bottom substrate. The operating voltage of the planar IPS 2-4 is V_p~33 V_{rms}. As the etching depth increases to h=0.5 μm, V_p decreases to ~25 V_{rms}. As h continues to increase to 1 μm and beyond, V_p saturates at ~23 V_{rms}, which means the on-state voltage is lowered by ~30.3%. Such a small etching depth can be easily achieved by the wet etching process.

The larger electrode spacing in IPS 5-10 (Figure 4.5(a)) than IPS 2-4 (Figure 4.5(b)) results in a weaker electric field intensity so that the driving voltage is higher. However, according to the typical Poisson problem in the form of $\nabla^2\Phi=0$, the penetrating depth of the electric fields into the LC medium strongly depends on the dimension (w+l). As a result, IPS 2-4 has a shallower electric field penetration depth than IPS 5-10 so that its maximum transmittance is ~5% lower. It is also because of this shallower electric field, in the etched IPS 2-4 cell only those LCs near the surface (above and below) can be activated. This explains why in Figure 4.5(a) (IPS 5-10) the etching depth saturates at ~2 μm, while it is only ~1 μm in Figure 4.5(b) (IPS 2-4).

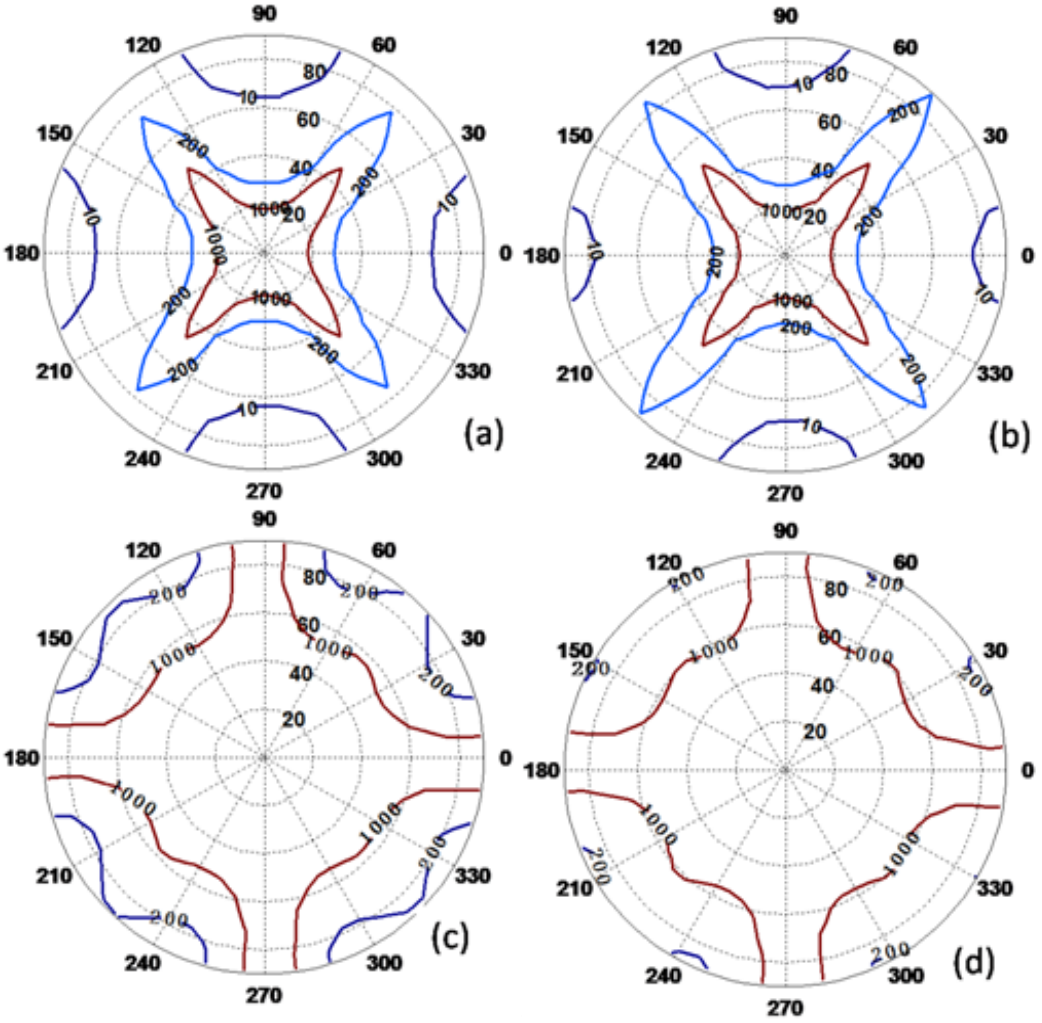

Figure 4.6 Simulated isocontrast plots of BPLC in traditional IPS [(a) and (c)] and etched IPS substrate [(b) and (d)]. (a) and (b) are without any compensation film, and (c) and (d) are with a biaxial film.

For this design, double-penetrating fringe fields can be generated and the operating voltage compared to the traditional planar IPS structure can be dramatically lowered. Besides, the small etching depth on the substrate can be easily achieved by the wet etching process.

We chose IPS 2-4 as an example for viewing angle comparison. The etching depth is set at 1 μm. Figure 4.6(a) and Figure 4.6(c) are the isocontrast plots of traditional IPS structure

without and with a biaxial compensation film. Similarly, Figure 4.6(b) and Figure 4.6(d) are the corresponding isocontrast plots for BPLCDs with etched IPS substrate. The biaxial film applied in Figure 4.6(c) and Figure 4.6(d) has following parameters: N_z =0.5 and $R_0 = (n_x\text{-}n_y)\cdot d = \lambda/2$ [63]. For both device configurations, the viewing angle is wide and symmetric. The viewing angle for the etched structure is somewhat wider than that of planar IPS cell. This is due to the additional symmetric domains formed in the etched areas.

In all, we proposed an IPS structure for lowering the operating voltage of BP-LCDs with a simple etching process. From simulations, the operating voltage can be reduced by ~30% in the IPS structure, if the etching depth is exceeds a certain small value. Moreover, the etched structure improves the viewing angle because of the generated symmetric domains in the etched areas.

4.1.3 BPLCDs with Protrusion Electrodes

To further reduce the operating voltage, deeper penetration into the LC bulk region is needed. In the conventional planar IPS structure, we could strengthen the horizontal electric field by reducing the electrode gap. However, as the electrode gap becomes narrower the penetration depth becomes shallower. The tradeoff is the reduced optical efficiency. Figure 4.7 is proposed protruded electrode design with trapezoid shape [31]. The BPLC layer is interposed between two glass substrates, which are further sandwiched between two crossed polarizers; pixel and common electrodes are made with the trapezoid-shaped protrusion structure. The trapezoid dimension is defined as follows: w_1 is the bottom width, w_2 is the top width, h is the height, and l is the space between common and pixel electrodes. The protrusion structures have been widely used in multidomain vertical alignment (MVA) LCDs for obtaining wide viewing angle [32][33].

Besides, it can be made transparent with organic positive photoresist so the aperture ratio of the LC panel will not be sacrificed. In this design, the induced birefringence on top of the electrode does not contribute to the transmittance since the electric field is almost vertical. But compared with traditional IPS structure, stronger horizontal electric fields are generated between the pixel and common electrodes. Moreover, the field is able to penetrate deeply into the LC bulk region. The former plays a key role to reduce operating voltage while the latter helps to achieve high transmittance. This explains why a much lower on-state voltage is needed for the protruded electrode design.

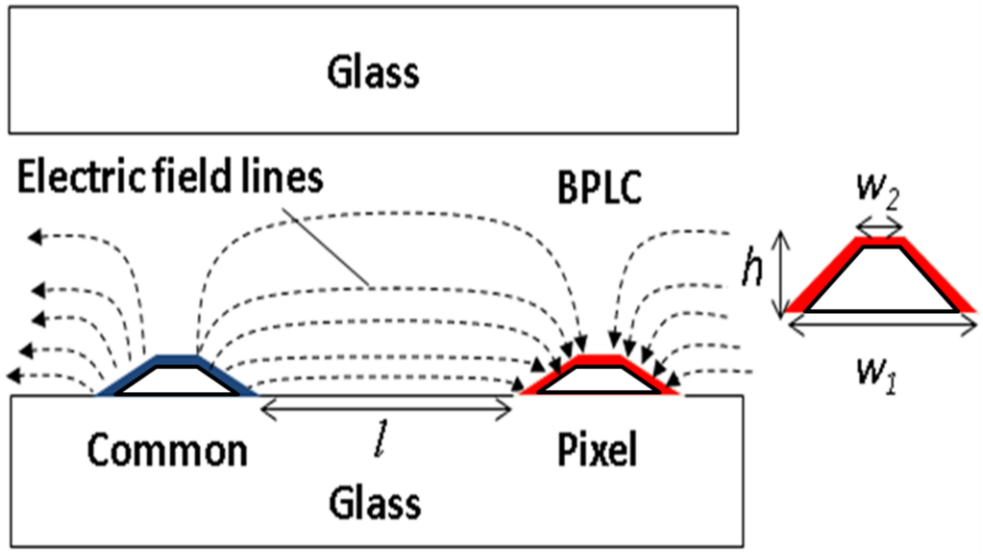

Figure 4.7 BPLCD structure with trapezoid-shaped protrusion electrodes and electric field lines.

For the protruded electrode with w_1=2 μm, w_2=1 μm, h=2 μm, and l=4 μm shown in Figure 4.8, the peak transmittance is ~71% (normalized to the transmittance of two parallel polarizers) at 17 V_{rms}. Compared to the conventional IPS structure with electrode width w=2 μm

and electrode gap l=4 μm (designated as IPS 2-4) with V_{on}~38 V_{rms} and peak transmittance ~66.5%, our protrusion electrode shows a significant reduction in driving voltage while maintaining a relatively high transmittance.

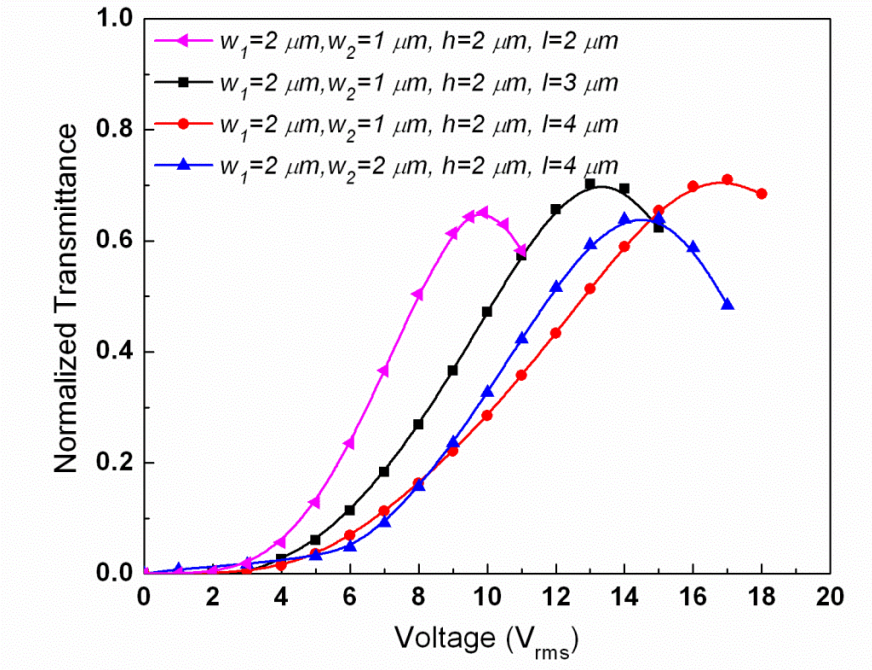

Figure 4.8 Normalized VT curves for protrusion electrodes with different dimensions.

To understand the underlying physics, we plot in Figure 4.9 the effective induced-birefringence (δn_{eff}) distribution for the protrusion electrode structure and IPS 2-4 structure. δn_{eff} is the effective birefringence that the normal incident light experiences. It is different from the induced birefringence Δn in Eq. (2.1), which is the overall induced-birefringence of the BPLC material regardless of the electric field direction and the effectiveness whether the Δn will contribute to the transmittance.

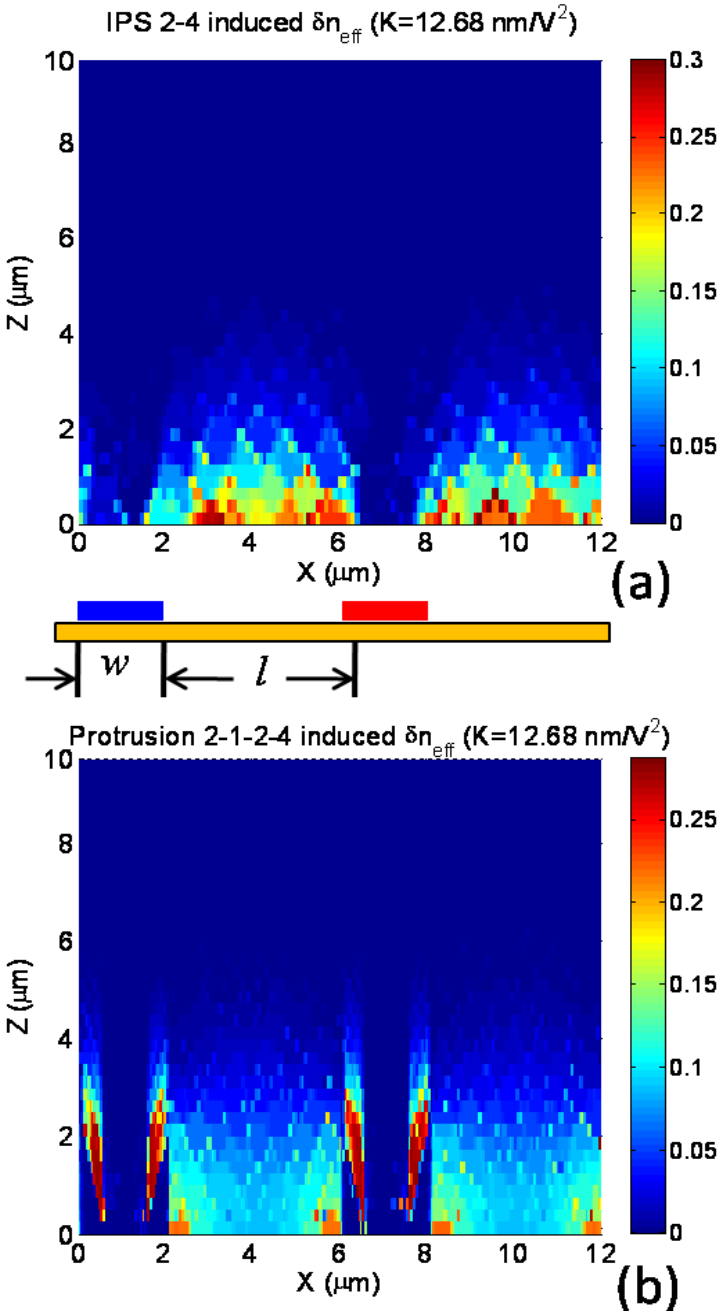

Figure 4.9 Induced effective birefringence (δn_{eff}) distribution for (a) conventional IPS cell with strip electrode with electrode width w=2 μm, spacing l=4 μm, and cell gap d=10 μm, and (b) protrusion electrode with w_1=2 μm, w_2=1 μm, h=4 μm and l=4 μm, cell gap d=10 μm.

From Figure 4.9, δn_{eff} is almost zero on top of the electrode for both structures since the electric field there is almost vertically distributed so that it does not provide phase change for the normal incident light. Nevertheless, the protrusion structure has a thicker penetrating depth and a larger δn_{eff} value in the effective region. This is the reason why a much lower on-state voltage is needed for the protrusion electrode design.

Figure 4.8 also shows the influence of electrode dimension on the voltage-dependent transmittance (VT) curve. Different electrode dimension generates different electric fields distribution in the BPLC cell. In comparison to the structure with parameters: w_1=2 μm, w_2=1 μm, h=2 μm, and l=4 μm, if the spacing width l is decreased to 3 μm or 2 μm, then the on-state voltage is lowered to 13 V_{rms} or 9.9 V_{rms}, respectively. This is attributed to the stronger electric field generated as the electrode gap gets smaller. However, the tradeoff is the lower transmittance. This is because the effective volume with horizontal electric field that accumulates the phase for the transmittance is smaller. If the size of w_2 is increased to 2 μm, the electric field near the bottom of the cell will be more uniformly distributed in horizontal direction. As a result, denoted by the black line in Figure 4.8, the operating voltage is reduced to 12 V_{rms}. Again, the tradeoff will be that the transmittance is lower since larger w_2 reduces the effective spacing area between the electrodes. If we increase the protrusion height h to 4 μm, the peak transmittance would increase to 74.2% at 13 V_{rms}. The electric field in this case is stronger and more uniform as compared to the one with a 2 μm height. Therefore, a lower driving voltage is needed. Meanwhile, the penetration of electric field gets deeper into the LC medium which enhances the transmittance. However, a 4 μm height protrusion electrode may be difficult to fabricate.

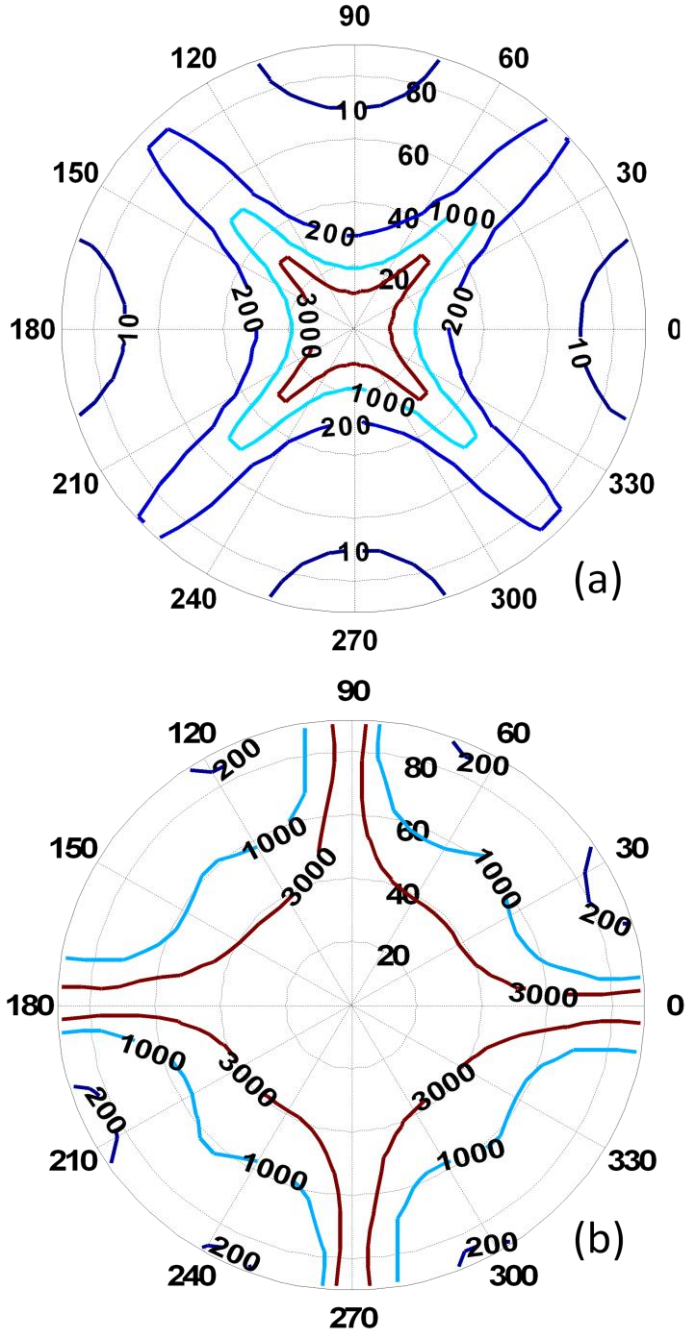

Figure 4.10 Isocontrast plots of the BPLC cell with protrusion: (a) without compensation films, and (b) with biaxial compensation films. The biaxial film parameters are: N_z=0.5, $R_0=(n_x-n_y)\cdot d=\lambda/2$.

In the voltage-off state, blue phase LC is optically isotropic so the dark state is very good. We have calculated the isocontrast contours for the protrusion electrode structure with dimensions of d=10 μm, w_1=2 μm, w_2=1 μm, h=2 μm, and l=4 μm and λ=550 nm. The contrast ratio (CR) of 200:1 is over 30^o without any compensation film in Figure 4.10(a). In Figure 4.10(b), adding a half-wave biaxial film greatly suppresses the off-axis light leakage of the two crossed polarizers, so that CR=1000:1 can reach about 60^o. This result is even better than that of the strip-electrode IPS BPLC cell we reported previously because the peak transmittance for the protrusion electrode is slightly higher. While blue phase liquid crystals have a really good dark state, the contrast ratio is mainly governed by the on-state transmittance.

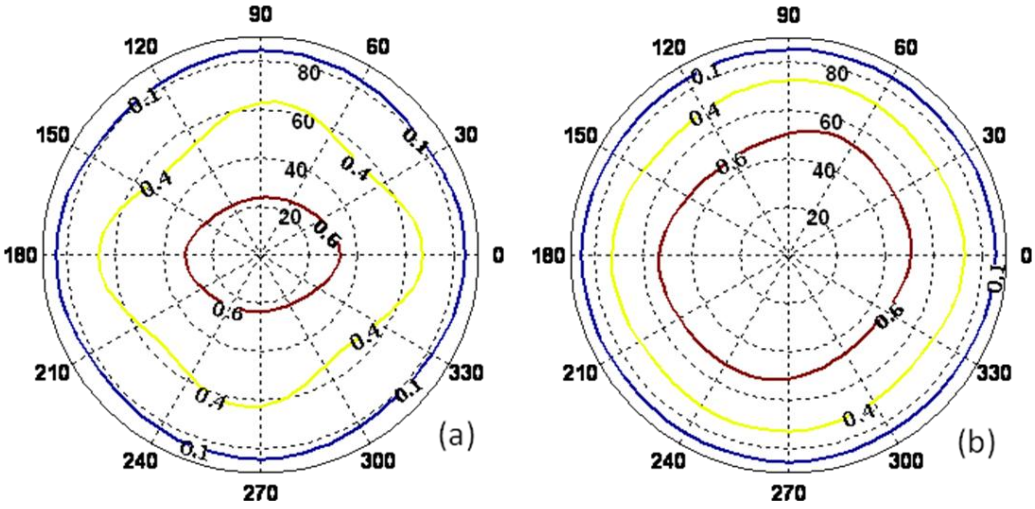

Figure 4.11 Angular dependent (azimuthal and polar) light transmittance for: (a) strip electrode (parameters: electrode width w=2 μm, and spacing l=4 μm), and (b) protrusion electrode (parameters: w_1=2 μm, w_2=1 μm, h=2 μm, and l=4 μm).

At off-angle incident, the vertical part of the field is no longer vertical to the incident light, so the curved electric field will compensate the transmittance. Figure 4.11 shows the angular dependent (azimuthal and polar) light transmittance for (a) strip electrode (parameters:

electrode width w=2 μm, and spacing width l=4 μm) and (b) protrusion electrode (parameters: w_1=2 μm, w_2=1 μm, h=2 μm, and l=4 μm). The polar angle of the protrusion structure with a transmittance of ~60% is over 50° while the strip electrode structure is only ~30°. The increasingly curved electric field in z-direction of protrusion electrode compensates more than the strip electrodes due to its deeper penetration layer into the LC bulk region. The iso-brightness contour plots in Figure 4.11 matches the induced effective birefringence distribution in Figure 4.9.

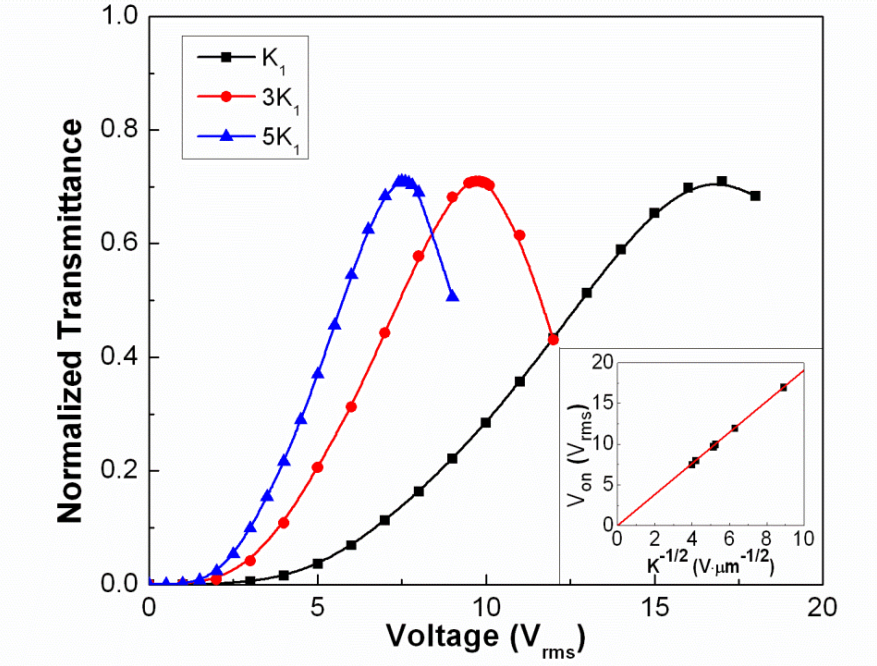

Figure 4.12 VT curves with different Kerr constants for protrusion electrode structure with w_1=2 μm, w_2=1 μm, h=4 μm and l=4 μm, cell gap d=10 μm, inset is the linear plot between on-state voltage and $1/\sqrt{K}$.

In addition to optimizing the device structure for generating strong and deep electric fields, it is equally important to develop LC materials with a larger Kerr constant. Figure 4.12

depicts the simulated VT curves at λ=550 nm under different Kerr constants (K_1=12.68 nm/V^2, K_2=3K_1, K_3=5K_1) for the protrusion electrode structure with dimensions of d=10 μm, w_1=2 μm, w_2=1 μm, h=2 μm, and l=4 μm. With the increased Kerr constant, the on-state voltage is reduced from 17V_{rms}, to 9.7V_{rms} and to 7.5V_{rms}. The low voltage operation would reduce the power consumption of the display devices. Amazingly, the on-state voltage is linearly proportional to $K^{-1/2}$, although the electric field generated from the protrusion electrodes is not uniform. Shown in the insert of Figure 4.12, the red line is the linear fitting for K_1, K_2, K_3, K_4=2K_1, and K_5=4.5K_1 with the linear equation as we proposed in Chapter 3, section 3.23:

$$V_{on} = A \cdot \frac{1}{\sqrt{K}}. \qquad (4.1)$$

Here, the device proportionality constant A=1.91 μm$^{1/2}$. We can conclude that for a given structure, while Kerr constant K represents the influence from the material side to the driving voltage, the device constant A represents the effect from the device design. Larger Kerr constant K and smaller device proportionality constant A will lead to a lower operating voltage.

To illustrate the importance of device structure, we compared the planar IPS electrodes with protrusion electrodes. From the experiment described in Chapter 2, section 2.2, and the analysis from Chapter 3, section 3.2.3, we have employed an IPS cell with a cell gap of 7.5 μm, and the ITO (indium tin oxide) electrode width of 10 μm and the electrode gap of 10 μm. We filled the same type of IPS cell with both the UCF BPLC material and Chisso BPLC material JC-BP01M. We find the device constant A is around 6 μm$^{1/2}$. Here, compared to the planar IPS cell, the protrusion electrode reported in Figure 4.12 has a device proportionality constant A=1.91 μm$^{1/2}$, which indeed indicates that a small A coefficient helps to lower the operating voltage.

In conclusion, the protrusion electrode structure is a feasible configuration for dramatically reducing the operating voltage of blue phase LCDs while keeping a reasonably high transmittance. There are already prototypes manufactured with this type of electrodes from leading LCD manufacturers such as Samsung and SEL lab [64, 65]. By optimizing the protrusion structure, the operating voltage can be successfully reduced to ~10 V_{rms}. This is an important milestone because the device can be driven by a-Si TFTs. With continuous development of large Kerr constant BPLC materials, the voltage can be reduced further.

4.1.4 BPLCDs with Extra Guiding Fields

In this section, the electrode configuration with extra guiding fields is proposed. The cross-section schematic view of the LC cell configuration is shown in Figure 4.13.

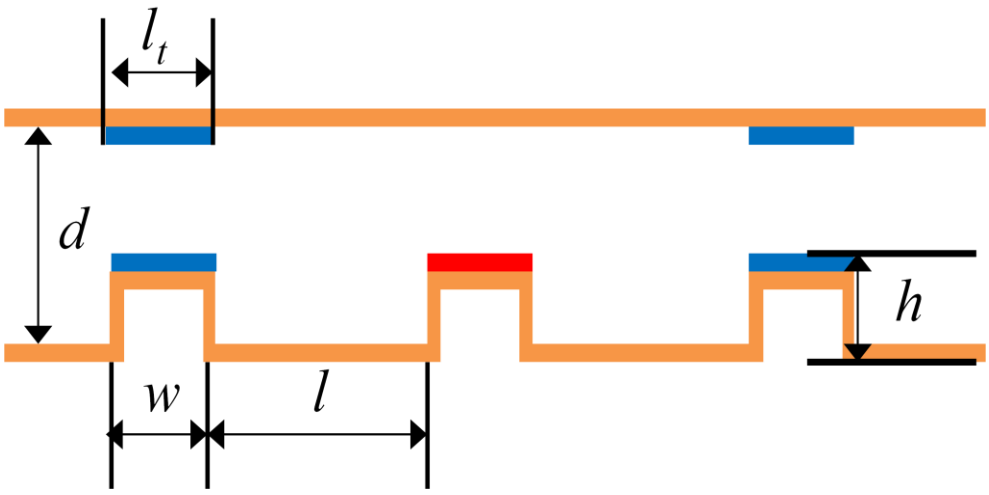

Figure 4.13 BPLCD configuration with extra guiding fields.

Different from the electrode structures proposed in the sections before, there is another common electrode formed on the inner surface of the top glass substrate providing the extra guiding fields, wherein these electrodes are further controlled by the driving TFT and switch unit.

Similarly, the LC layer is interposed between two glass substrates, which is further sandwiched between two crossed polarizers; the protruded part on the bottom substrate can be part of the bottom glass substrate and can be obtained by etching, photolithography, or the like methods on the glass substrate; the protruded part can also be an insulating layer on top of a flat glass substrate; a pixel electrode is formed on the surface of the protruded part; a common electrode is formed on the surface of adjacent protruded part. A retardation film, such as a biaxial film or uniaxial film, can be laminated between the bottom and the top polarizers to expand the viewing angle of the display. Electrodes may have the same width or different width. As shown the figure, l is the gap between adjacent electrodes on the bottom substrate, l_t is the gap between adjacent electrodes on the top substrate, w is the pixel electrode width, h is the etching depth for the undercut, and d is the cell gap.

Figure 4.14 shows the electric field lines distribution for the BPLCD structure in Figure 4.13. Usually, on top of the electrode, the electric field lines are perpendicular to the electrode. Therefore, very little phase retardation is accumulated and this part does not contribute much to the transmittance. For this proposed structure, both the common electrodes on the top and bottom substrates guide the electric field, so the electric field in the horizontal direction near the edge surface of the electrodes is stronger. BPLC in this area can contribute more to the overall performance. Besides, unlike the conventional IPS structure that the electric field is penetrated into only the LC region on top of the electrodes, the electrode on the protruded part enables a double-penetration electric field deep into the LC bulk area, that is, the electric field penetrates into the LC regions both above and below the electrodes. This adds to the overall transmittance while lowering the operating voltage.

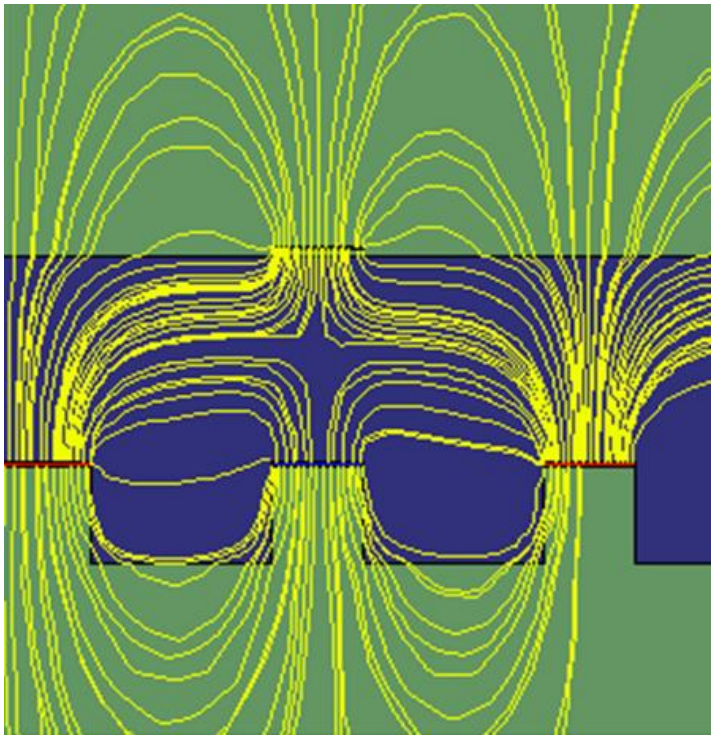

Figure 4.14 Electric field lines distribution for the BPLCD with extra guiding fields.

Different shapes of electrodes would result in different operating voltages and transmittance. Shown in Figure 4.15 are the examples of different electrodes structures with extra guiding fields. They all have extra electrodes on the top substrates. The electrodes can be common electrodes or floating electrodes. The sizes of the electrodes width and gap width between the electrodes can be optimized to the different structure accordingly.

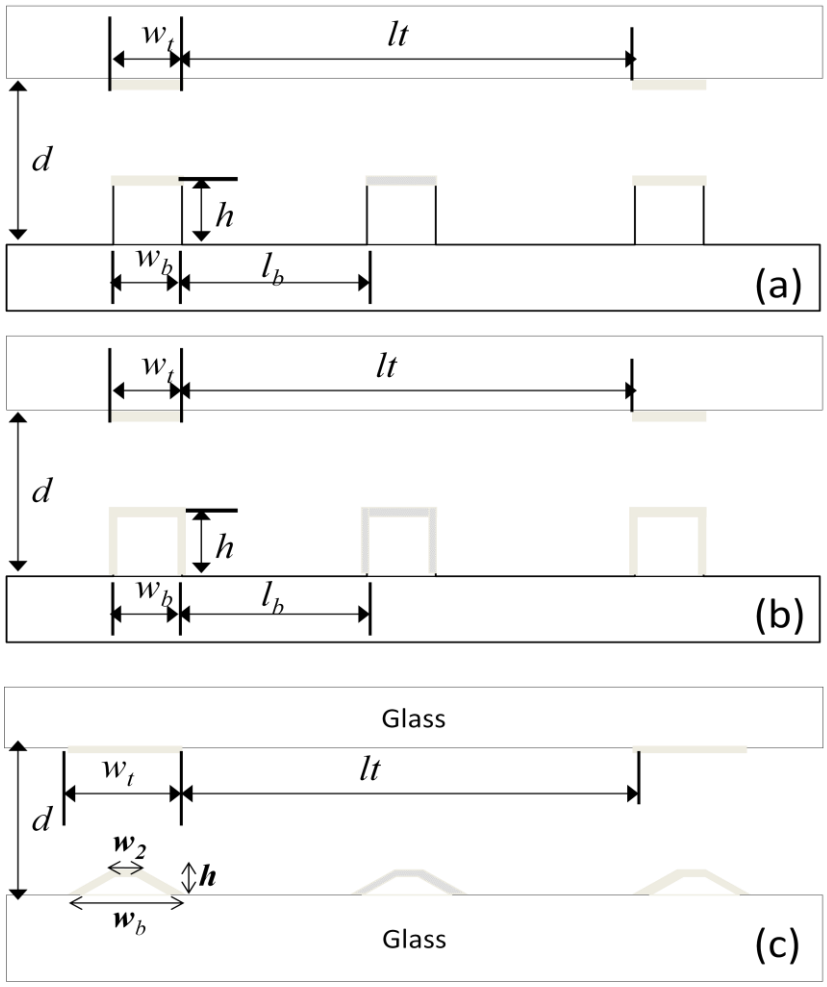

Figure 4.15 Proposed BPLCD electrode structures with extra guiding fields

Figure 4.16 shows the corresponding voltage-dependent transmittance curves with a Kerr constant K=1.268×10^{-8}m/V^2. For comparison, curve 1 is for the traditional IPS structure with the electrode width w=2μm, and spacing between electrodes l=4μm. The peak transmittance is 63.4% at 33V$_{rms}$. Curve 2 is one example of the structure in Figure 4.16(a), the top common electrode is aligned with the bottom common electrode, with w_t=w_b=2 μm, l_t=10 μm, l_b=4 μm, d=3 μm, h=1 μm. The operating voltage is 66% at 22 V$_{rms}$, which is ~30% lower than that in curve 1. For this configuration, to fully use the electric field generated, it is preferred that h to be higher than the sing-side penetration depth of the pixel electrodes. Curve 3 is one example of the structure in

Figure 4.16(b), the top common electrode is aligned with the bottom common electrode, with w_t=w_b=2 μm, l_t=10 μm, l_b=4 μm, d=5 μm, h=2 μm. The operating voltage is only 13 V_{rms}, much lower than that with curve 2. This is because the electric field is stronger since the two sides of the protruded part are also coated with ITO. Curve 4 is one example of the structure in Figure 4.16(c), the top common electrode is aligned with the bottom common electrode, with w_t=w_b=2 μm, w_2=1 μm, l_t=10 μm, l_b=4 μm, d=6 μm, h=2 μm. The peak transmittance is 72.5% at 16 V_{rms}. Compared with the rectangular bottom pixel electrode, the one with the trapezoid shape has higher efficiency since there is more effective LC region; but the operating voltage is also a little higher, the weaker electric field comes from the larger distance between the top of the protrusions. If the distance between the common electrodes l_b is smaller, the electric field will be stronger, and the operating voltage can be lowered to below 10 volts.

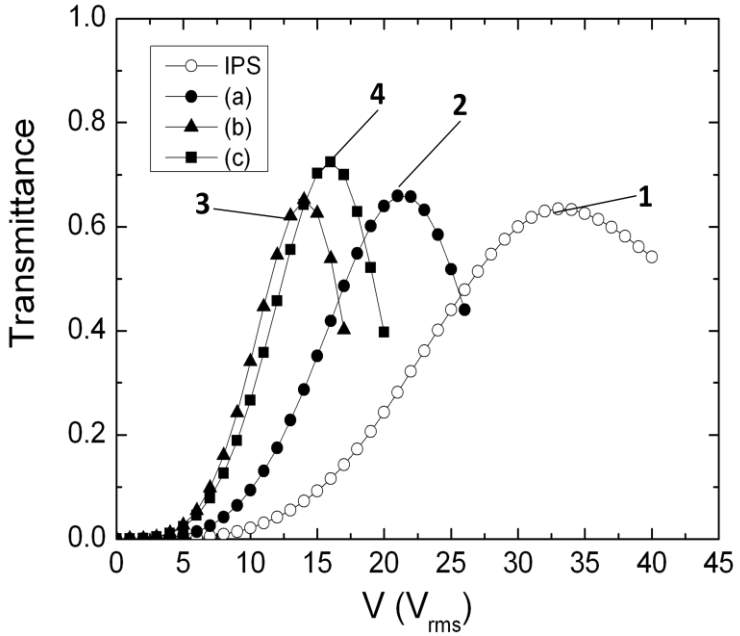

Figure 4.16 Voltage-Transmittance curves for different BPLCD electrode structures with extra guiding fields

Overall speaking, compared with the proposed electrode structures without extra guiding fields, the current design has both the common electrodes on the top and bottom substrates guiding the electric field, so the electric field in the horizontal direction near the edge surface of the electrodes is stronger. Therefore, BPLC in this area can contribute more to the overall performance. Thus, a lower driving voltage and higher transmittance can be achieved.

4.2 Low Wavelength Dispersion BPLCDs

As discussed in Chapter 3, Kerr constant decreases as the wavelength increases and gradually saturates. Therefore, the voltage-transmittance curves for red, blue and green colors do not overlap.

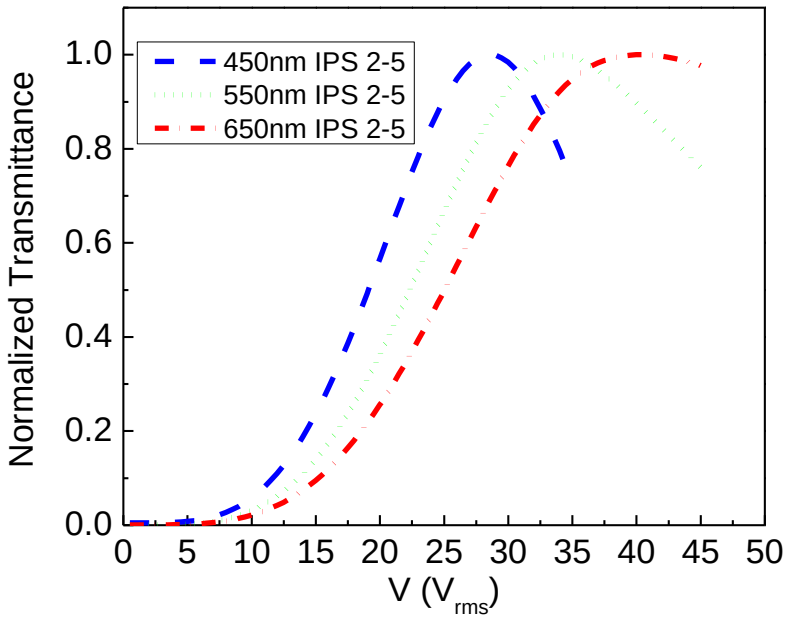

Figure 4.17 VT curve of IPS 2-5 BPLCD at 450nm, 550nm and 650nm.

According to the parameters in Table 3.1, we have simulated the VT curves of an IPS BPLCD at three different wavelengths, and results are shown in Figure 4.17. The IPS structure

has an electrode width of 2μm and electrode gap of 5μm. The dispersion of VT curves for R, G and B colors is quite severe. That means, each color has a different on-state voltage. To accurately control the gray levels, three gamma curves settings are needed for R, G and B colors separately. This adds a great burden to the electronics driving. In order to realize a single gamma curve driving, ideally the red, blue and green pixels should have the same VT curves. Therefore, the wavelength dispersion issue needs to be addressed.

In order to achieve the same on-state voltage for R, G and B pixels, the electric fields in the red, blue and green pixels should generate the same phase retardation profile at the same applied voltage. As the Kerr constant increases with decreasing wavelength, the average electric field in red pixel should be stronger than that of green pixel, and the average electric field in green pixel should be stronger than that of blue pixel.

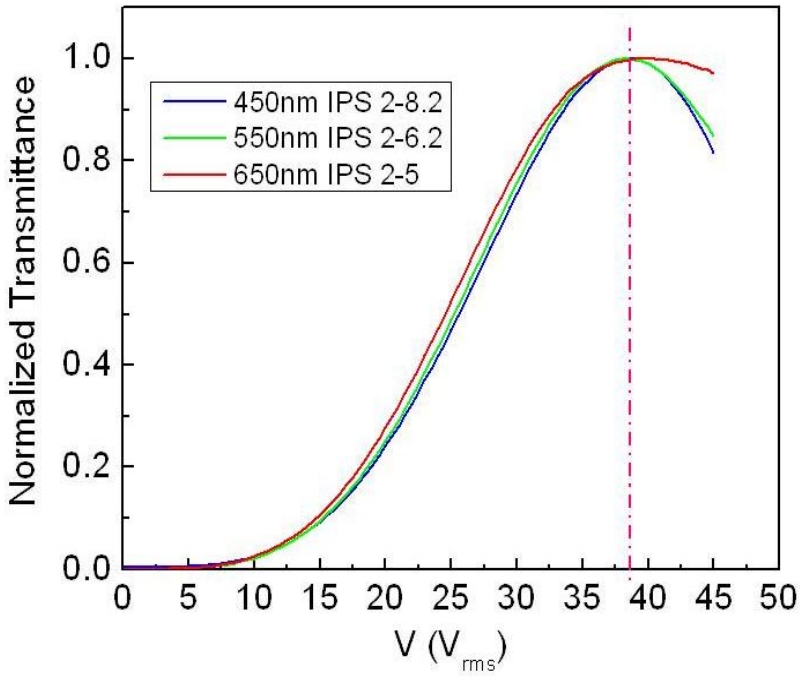

Figure 4.18 Simulated VT curve of IPS BPLCD at 450nm, 550nm and 650nm.

The *w*-*l* ratios are different for RGB pixels as indicated.

According to the guidelines mentioned above, we propose an approach that different electrode width *w* and gap width *l* ratios can be applied to R, G and B color pixels. Figure 4.18 shows the result of an exemplary configuration by changing the *w-l* ratios of the electrode width and gap. In this IPS structure, for red pixels the electrode width is 2μm and gap between electrodes is 5μm; for green pixels the electrode width is 2μm and gap between electrodes is 6.2μm; and for blue pixels the electrode width is 2μm and gap between electrodes is 8.2μm. The larger the gap width, the weaker the electric field at the same applied voltage. As a result, we can see in Figure 4.18 that the voltage dependent transmittance curves of red, green and blue pixels overlap very well with each other.

We also propose another approach that the shape of the electrodes can be different in each pixel. Figure 4.19 shows the result of the exemplary configuration by changing the protrusion electrode height. In this structure with protruded electrodes in a trapezoid shape as proposed in section 4.1.3, the bottom width of the trapezoid electrode is fixed at 2 μm, the top width of the trapezoid electrode is fixed at 1 μm, and gap between electrodes is fixed at 4 μm. A larger height of the trapezoid electrode will result in a stronger electric field. Therefore, for red pixels the height is 2.6 μm; for green pixels the height is 2 μm; and for blue pixels the height is 1.35 μm. Compared to the VT curves in Figure 4.17 that have the fixed electrode width 2μm and gap 5μm, the new configurations (Figures 4.18 and 4.19) have eliminated the wavelength dispersion. The elimination of the wavelength dispersion has therefore enabled single gamma driving for gray level control.

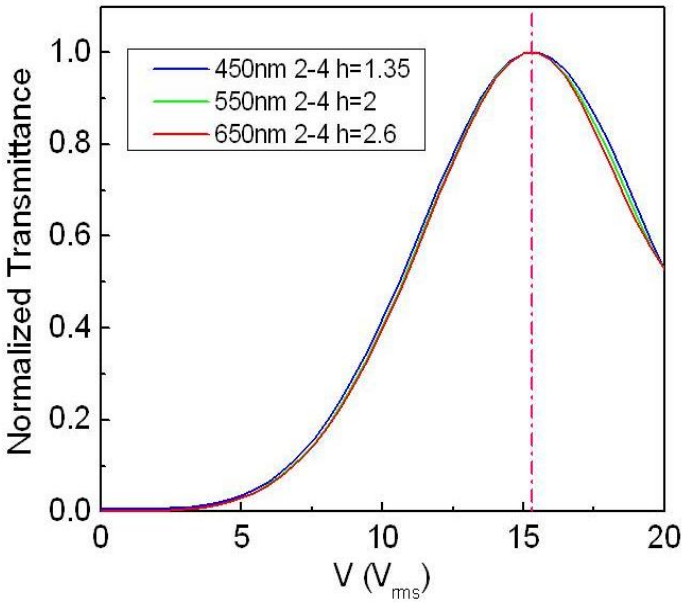

Figure 4.19 Simulated VT curves of BPLCD with trapezoid electrodes at 450nm, 550nm and 650nm. The heights of the trapezoid electrodes are different for RGB pixels as indicated.

4.3 Low Color Shift BPLCDs

Color shift is another important factor to determine the color uniformity of a display device at different viewing directions. For high-end LCD devices, small color shift is one of the major challenges. In this section, the modeling of color shift will be introduced. We will calculate the color shift of a conventional IPS blue phase LCD with stripe electrodes, and then propose device designs for suppressing color shift.

The CIE 1931 XYZ color space is one of the first mathematically defined color spaces. It was created by the International Commission on Illumination (CIE) in 1931. This three-valued (*X*, *Y*, *Z*) system can effectively model the appearance of the colors by human eyes, including the specifications from the observer, e.g., light source, devices and other aspects of the viewing

conditions.

The CIE color space defines all the colors in terms of three imaginary primaries X, Y, and Z based on the human visual system. The X, Y, Z tristimulus values of a color stimulus which represent the luminance of the colors are expressed as:

$$X = k \int_{380nm}^{780nm} I(\lambda)\bar{x}(\lambda)d\lambda$$

$$Y = k \int_{380nm}^{780nm} I(\lambda)\bar{y}(\lambda)d\lambda$$

$$Z = k \int_{380nm}^{780nm} I(\lambda)\bar{z}(\lambda)d\lambda \qquad (4.2)$$

where k is a constant, $I(\lambda)$ is the spectral power distribution at the given wavelength, $\bar{x}$, $\bar{y}$, and $\bar{z}$ are the color-matching functions that can be thought of as the spectral sensitivity curves of three linear light detectors that yield the CIE XYZ tristimulus values.

In this model, Y means luminance, Z is quasi-equal to blue stimulation, or the S cone response, and X is a mix (a linear combination) of cone response curves chosen to be orthogonal to luminance and nonnegative. Since the human eye has three types of color sensors that respond to different ranges of wavelengths, a full plot of all visible colors is a three-dimensional figure. However, the concept of color can be divided into two parts: brightness and chromaticity. The CIE XYZ color space was deliberately designed so that the Y parameter was a measure of the brightness or luminance of a color. The chromaticity of a color was then specified by the two derived parameters x and y, two of the three normalized values which are functions of all three tristimulus values X, Y, and Z:

$$x = \frac{X}{X + Y + Z}$$

$$y = \frac{Y}{X + Y + Z}$$

$$z = \frac{Z}{X + Y + Z} = 1 - x - y \,. \tag{4.3}$$

The CIE 1976 color space is a simple-to-compute transformation of the CIE 1931 color space. It is also called (*u'*,*v'*) diagram. The (*u'*,*v'*) coordinates are related to the (x, y) coordinates as:

$$u' = \frac{4X}{X + 15Y + 3Z} = \frac{4x}{-2x + 12y + 3}$$

$$v' = \frac{9Y}{X + 15Y + 3Z} = \frac{9y}{-2x + 12y + 3} \,. \tag{4.4}$$

The chromaticity coordinates (*u'*,*v'*) are usually measured by a spectro-radiometer in the visually most color deviating areas such as the horizontal and vertical directions of an LCD panel.

Based on Eq. (4.4), the color difference of any two points (1 and 2) can be calculated using the following formula:

$$\Delta u'v' = \sqrt{(u'_2 - u'_1)^2 + (v'_2 - v'_1)^2} \,. \tag{4.5}$$

The (u_1', v_1') coordinates is usually the value at normal viewing angle and the (u_2', v_2') values are the values at viewing angles with an oblique viewing angle.

Current research of BPLC for display applications is conducted under the traditional stripe electrode structure using IPS cells, as depicted in Figure 4.20(a). The cell is placed

between two crossed linear polarizers. The horizontal electric fields generated from IPS electrodes induce phase retardation for the incident light. Here, *w* represents the electrode width and *l* is the spacing between the electrodes. Figure 4.20(b) shows the zigzag electrode structure for blue phase LCDs, where *α* stands for the bending angle of the electrodes. In this section, the color shift, transmittance, and viewing angle between these two electrode configurations will be compared.

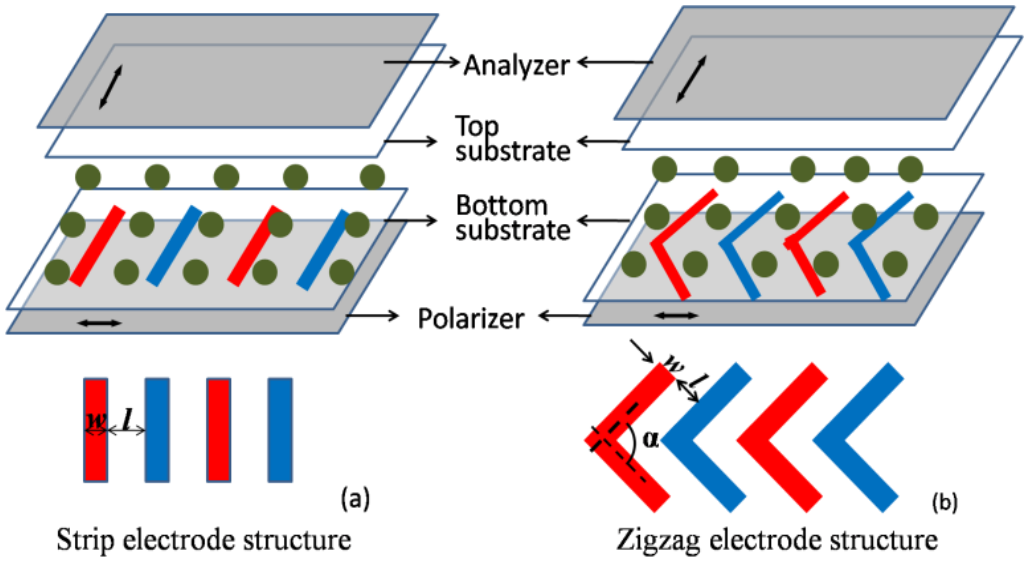

Figure 4.20 (a) Stripe electrode structure and (b) zigzag electrode structure for BPLC IPS cells.

During simulations, we calculated a blue phase LC cell with an electrode width w=5 μm, spacing between electrodes l=10 μm, Kerr constant K~12.7 nm/V^2 and wavelength λ=550 nm. Unlike conventional LCDs which are affected by the cell gaps, the transmittance does not change too much with cell gap variance in BPLCs. Therefore, all the simulations used throughout this section have a cell gap d=10 μm.

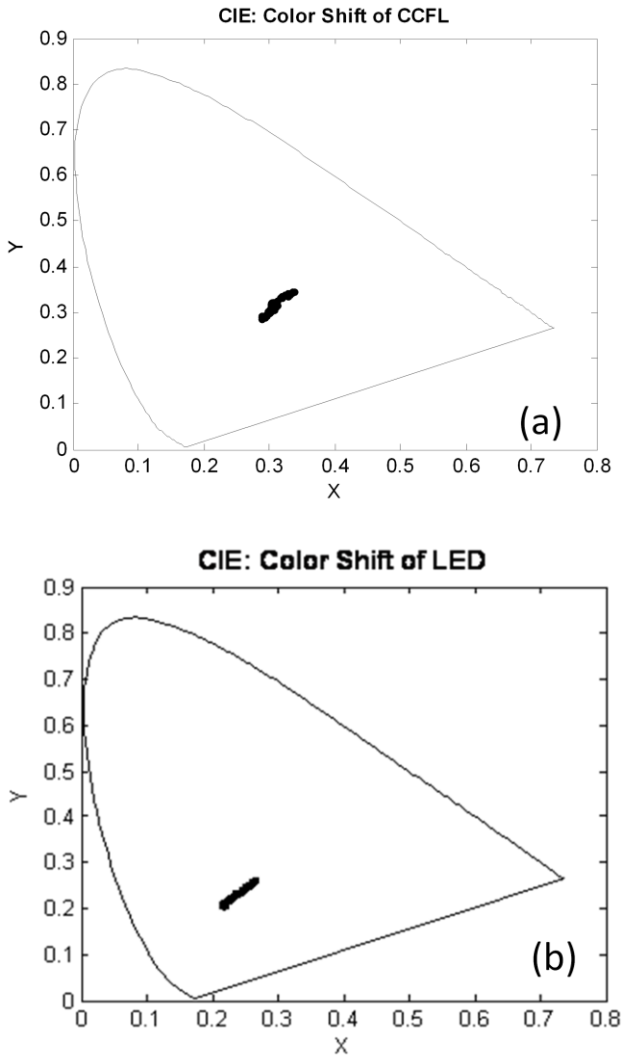

Figure 4.21 Simulated bright state color-shift of the IPS BPLC cell with strip electrode without compensation film: (a) with CCFL light source, and (b) with LED light source. IPS cell parameters are: d=10 μm, w=5 μm and l=10 μm.

We have calculated the color shift for the IPS BPLC cell with stripe electrodes. Figure 4.21(a) show the bright state color shift in CIE 1931 using a CCFL light source of the strip electrode structures, while Figure 4.21(b) is with the LED light source. The dots in the figures represent the color shift from the standard white point. We used the real data on light source,

polarizer, compensation film, and color filters in the calculations. The wavelength dependent Kerr constant is also taken into consideration as discussion before:

$$\lambda K \approx G\frac{\lambda^2\lambda^{*2}}{\lambda^2-\lambda^{*2}} \tag{4.6}$$

here, we use the parameter G~8.78×10^{-2} V^{-2} and λ*~250 nm under the assumption that K~12.7 nm/V^2 at λ=550 nm. [59] Under this circumstance, we can obtain the Kerr constants in the visible range by Eq. (4.6) for the color shift.

Due to the unique symmetric feature of blue phase liquid crystals, even with only the stripe electrode structure, a multi-domain-like distribution of induced Δn in the IPS structure could be produced to make the viewing angle symmetric. The color shift of the bright state is reasonably small; we obtained the $\Delta u'v'$= (0.0030, 0.0077, 0.0327) for CCFL backlight and $\Delta u'v'$= (0.0023, 0.0062, 0.0283) for LED backlight with RGB primaries, respectively.

Nevertheless, if we use 90^o zigzag electrodes instead of the stripes, more sub-domains will be created. Liquid crystal molecules are rotating into the complementary directions, resulting in an even better and more uniformly compensated bright state. With the same BPLC material, Figure 4.22(a) and Figure 4.22(b) are the calculated results for the bright state color shift based on CIE 1931 using a CCFL backlight and a LED backlight for the zigzag electrode structure. Compared with Figure 4.21(a) and Figure 4.21(b), the color shift with zigzag electrode structure is significantly suppressed. Quantitatively, the $\Delta u'v'$ values are reduced to (0.0019, 0.0028, 0.0161) for the employed CCFL light source and (0.0013, 0.0024, 0.0127) for the LED light source at RGB primaries.

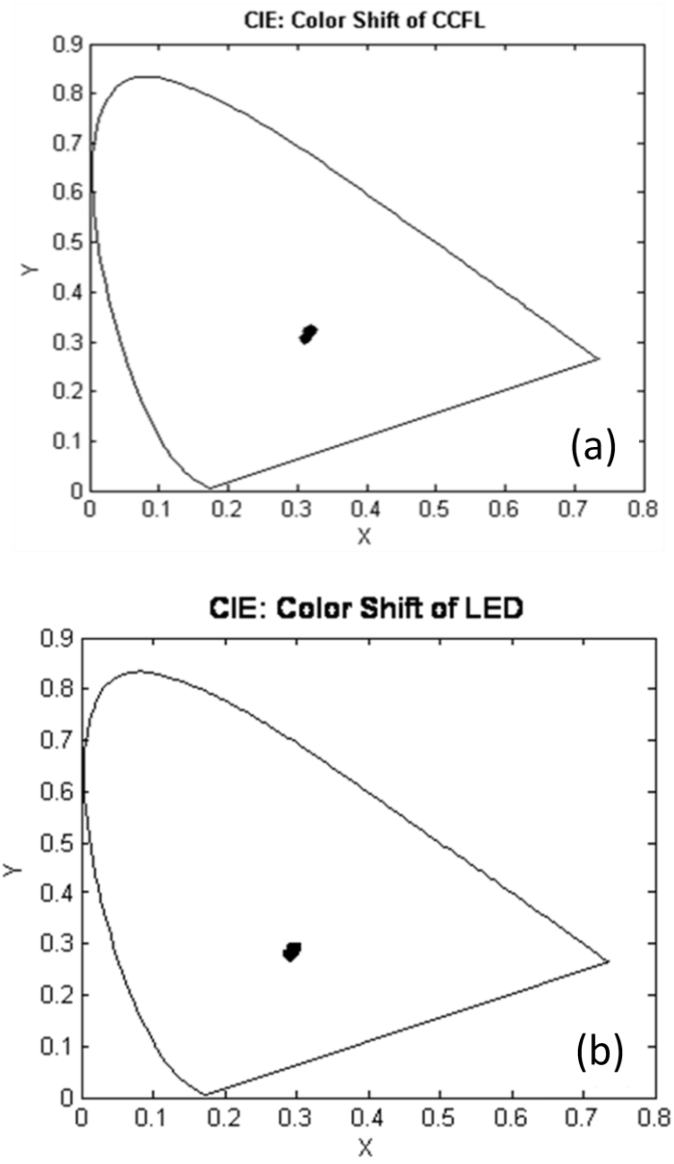

Figure 4.22 Simulated bright state color-shift of the IPS BPLC cell with zigzag electrode without compensation film: (a) with CCFL light source, and (b) with LED light source. IPS cell parameters are: d=10 μm, w=5 μm and l=10 μm.

We have also studied the bending angle effect and electrode structure effect of the zigzag electrodes. As shown in Figure 4.20(b), the zigzag electrode is bent at an angle α, which is the angle between the two arms of the electrode. A series of zigzag electrodes are alternatively

arranged to form inter-digital electrodes on the same substrate as the common electrode and the pixel electrode, respectively, which are connected to thin-film transistors (TFTs) in a practical LCD panel.

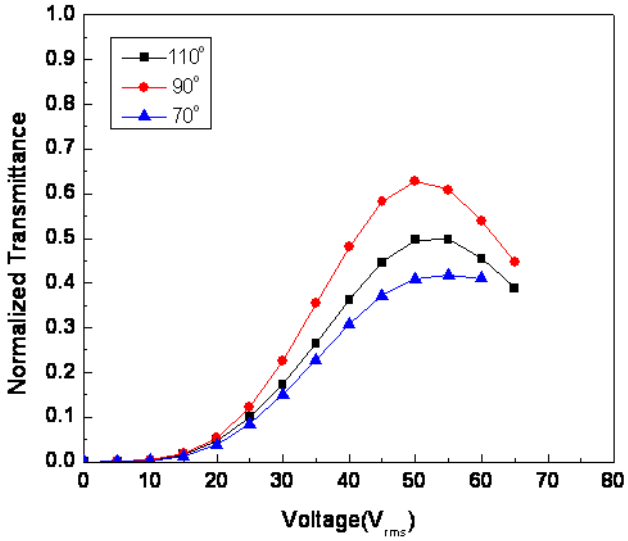

Figure 4.23 Simulated VT curves of the IPS BPLC cell with zigzag electrode structure for different bending angles at λ=550 nm

Voltage dependent transmittance curves for three different bending angles α=110^o, 90^o and 70^o are shown in Figure 4.23, respectively. The transmittance has been normalized to the maximum transmittance of two parallel polarizers. It has been reported by Lu, et al [66] that for conventional nematic liquid crystal in an IPS cell with zigzag electrode structures, the larger the bending angle, the lower the operating voltage and the higher the transmittance. As the bending angle of the zigzag electrode decreases, higher on-state voltage is needed for the required effective projected electric field to switch the LC directors. However, among the three zigzag structures of blue phase LC in the IPS cell described here, the 90^o bending angle has the highest transmittance. Their on-state voltage is roughly the same. The reason comes from the unique symmetric molecular structure of the blue phase LCs. The 90^o bending angle can always be an

optimal, because it provides a more symmetric electric field for BPLCs so that a larger maximum electric-induced birefringence can be obtained. In the previous calculation of the color shift, the bending angle is also set at 90^{o}.

Electrode dimension plays an important role in the electro-optic properties of the IPS BPLC cell. To better understand the zigzag electrode structure, we compared it with the strip structure in the following ways with different electrode dimensions as shown in Figure 4.24. The transmittance is normalized to the maximum value from two parallel polarizers (34.83%).

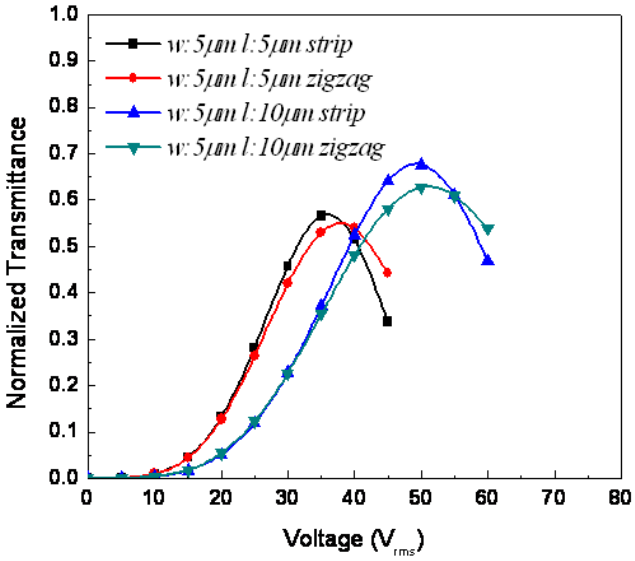

Figure 4.24 VT curves of the IPS BP cell with different electrode dimensions and structures at 550 nm.

In the strip-electrode IPS cell, transmittance mainly originates from the induced birefringence by Kerr effect in the electrode spacing area [53]. Smaller spacing width *l* will result in a stronger electric field intensity which in turn leads to a lower driving voltage V_{on}. The zigzag structure shows exactly the same trend. The VT curves of the zigzag structure with the electrode dimensions of [*w*=5 μm, *l*=5 μm] demonstrate lower driving voltages than those of [*w*=5 μm,

l=10 μm]. Considering that only the regions between electrodes contribute to the transmittance, a larger l/w ratio is in favor. As shown in Figure 4.24, both for strip electrode structure and zigzag electrode structure, the dimensions of [w=5 μm, l=10 μm] with l/w=2 have a higher transmittance than the dimension [w=5 μm, l=5 μm] with l/w=1.

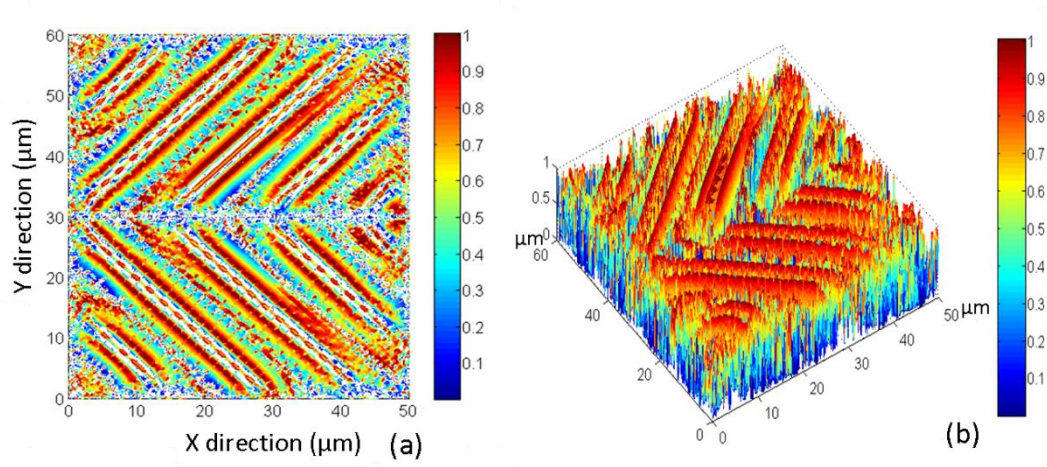

Figure 4.25 (a) 2D and (b) 3D views of the transmittance profile for the zigzag structure with w=5 μm, l=5 μm, α=90^{o}, legend bar shows the normalized transmittance.

If we compare the strip structure with the zigzag structure individually, we may find out that for the same electrode width and spacing width, zigzag structure exhibits a little lower transmittance. This is attributed to the dead zones at the turning corners of the zigzag electrodes shown in Figure 4.25. The dead zone forms a horizontal disclination line locating at the position of ~30 μm in y direction in Figure 4.25(a). The electric fields in the dead zones do not effectively induce birefringence for the LCs so that they make no contribution to the transmittance.

As introduced in Chapter 3 that the viewing angle of BPLCD is wide and symmetric. Here we compared the viewing angle of the IPS cell with strip electrodes and zigzag electrodes.

Figure 4.26(a) and Figure 4.26(b) are the isocontrast plots of the IPS BPLC cell with strip electrodes, while Figure 4.26(c) and Figure 4.26(d) are the plots with zigzag electrodes. The biaxial film compensated plots shown in Figure 4.26(b) and Figure 4.26(d) have the following parameters: N_z=0.5 and $R_0 = (n_x\text{-}n_y)\cdot d=\lambda/2$. The cell dimensions used in simulation are: cell gap d=10 μm, electrode width w=5 μm, spacing width l=10 μm, and λ=550 nm. We find that the contrast ratio over 1000:1 can be expanded to ~55^o-66^o with compensation films for both structures. The viewing angle for both strip and zigzag electrode structures is reasonably wide and comparable to a conventional four-domain nematic IPS LCD with zigzag structure.

It should be also noticed that although the plots for strip electrode and the zigzag electrode are very similar, the zigzag electrode has a slightly narrower viewing angle. This can be explained by their corresponding luminance polar contour plots shown in Figure 4.27(a) and 4.27(b). For BPLCs, the isotropic dark state is perfect and is affected only by the light leakage from the crossed polarizers at oblique incidence. The on-state transmittance of the zigzag electrode structure is a little lower than that of the strip electrode structure due to the presence of dead zones, so the contrast ratio is somewhat lower, too. This can be considered as one of the differences between BPLCDs and conventional LCDs. Despite of the a little lower luminance and contrast ratio, the brightness is more uniformly distributed in Figure 4.27(b). This is related to the four-domains formed by zigzag electrodes. The on-state brightness for the same electrode structure with and without compensation film is similar since compensation film is only used to compensate the light leakage induced by the crossed polarizers at oblique angle at dark state. Nevertheless, for both structures, the contrast ratio for the one with compensation film is larger than the one without.

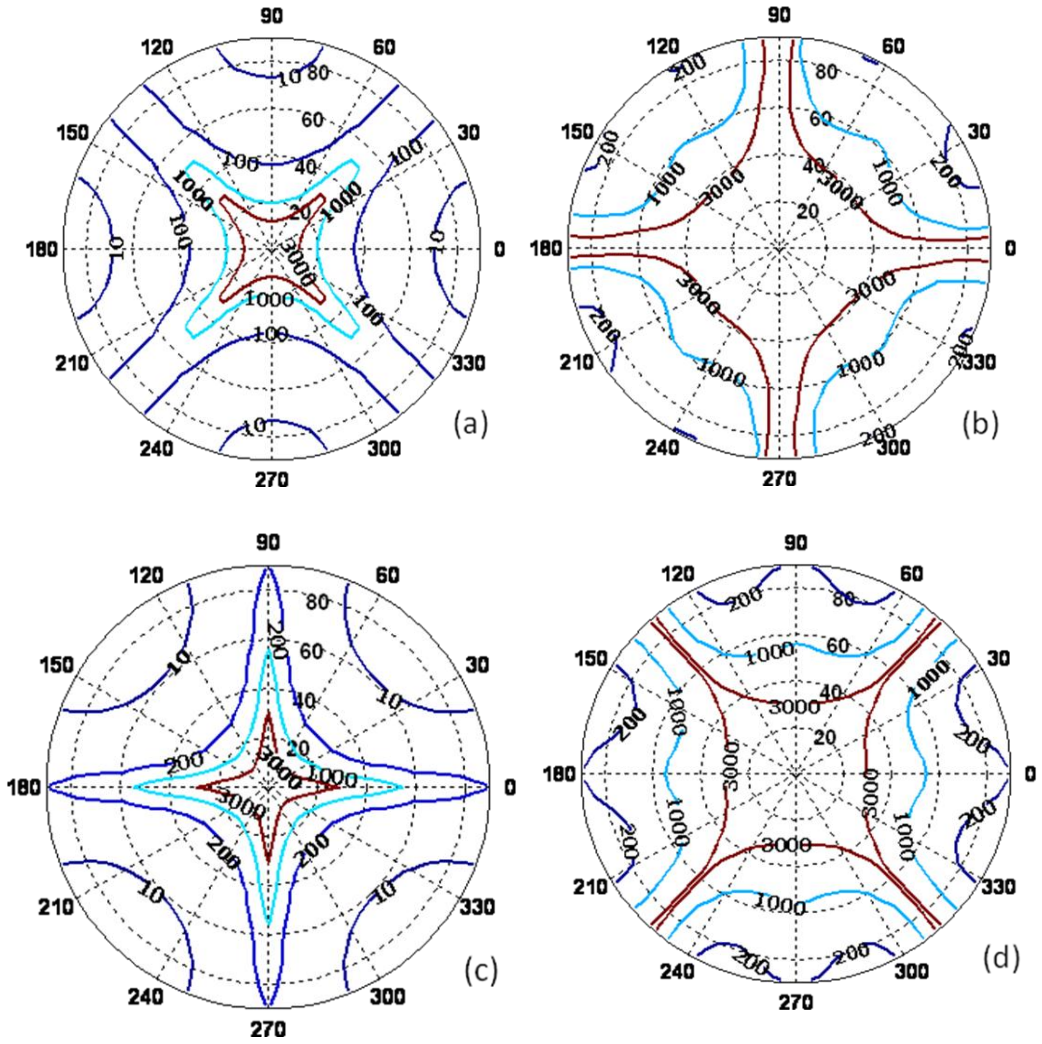

Figure 4.26 Isocontrast plots of the IPS BPLC cell: (a) (b) strip electrodes without and with compensation films, and (c) (d) zigzag electrodes without and with compensation films. Biaxial film parameters: Nz=0.5, R_0= $(n_x$-$n_y)\cdot d=\lambda/2$. IPS cell parameters: d=10 μm, w=5 μm, and l=10 μm and λ=550 nm.

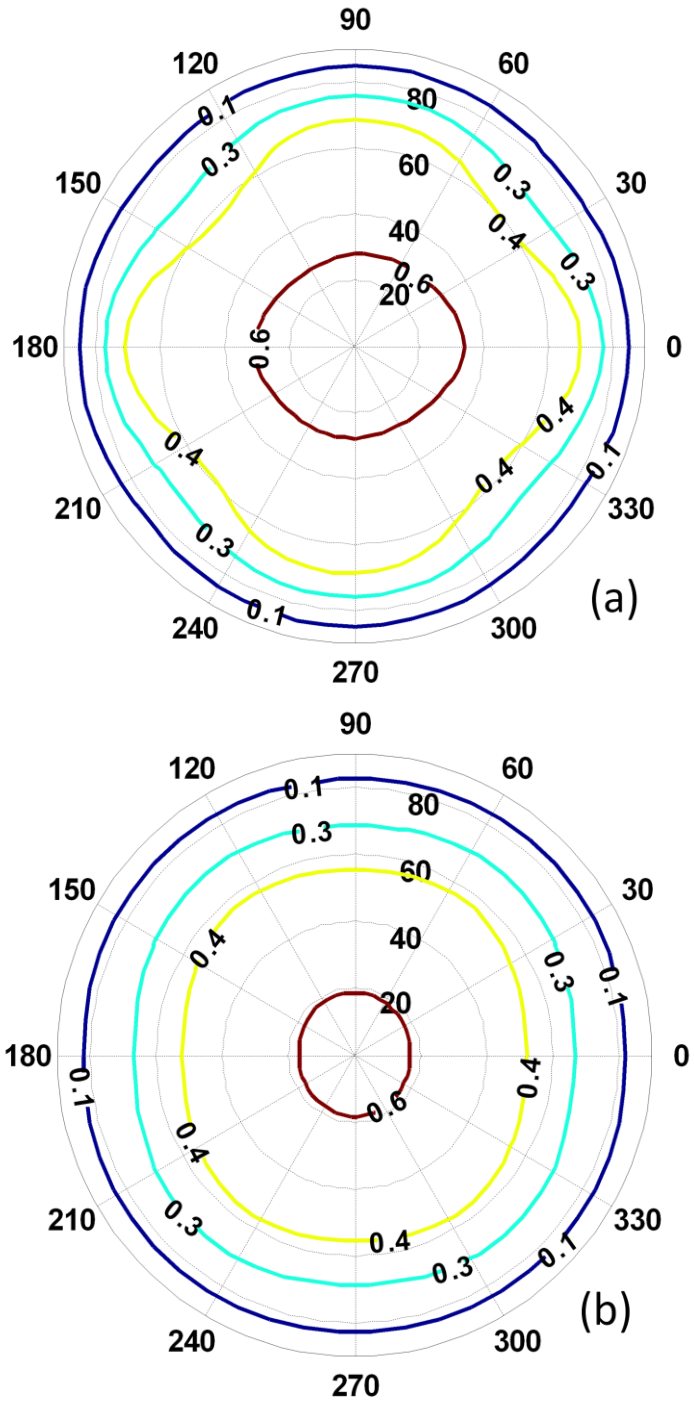

Figure 4.27 Illuminance polar charts for the IPS BPLC cells: (a) strip electrodes, and (b) zigzag electrodes. Cell parameters: d=10 μm, w=5 μm, and l=10 μm and λ=550 nm. (No compensation films are used).

We have studied the zigzag electrode structure for blue phase LCDs and compared its performances with the traditional strip electrode structure. The 90^o bending angle is found to be the best for zigzag structure in which the viewing angle is wide and symmetric, and the color shift is significantly suppressed. However, a tradeoff in slightly lower transmittance is found because of the presence of dead zones. This reduced transmittance also causes a slightly lower contrast ratio.

4.4 Low Hysteresis BPLCDs

Hysteresis is a common phenomenon in polymer-stabilized LCs [5] including polymer-stabilized BPLCs. Detailed mechanisms depend on the polymer concentration and composition [67], and UV curing conditions. Hysteresis affects the accuracy of gray-scale control and should be eliminated. There is an urgent need to develop hysteresis-free BPLC devices.

In this section, we correlate the hysteresis of a polymer- stabilized BPLC with the peak electric field of different IPS electrode dimensions. If the peak electric field is below a critical field (~5 V/μm), hysteresis is negligible. Based on this guideline, we propose elliptical protrusion electrodes with reduced peak electric field to achieve hysteresis-free BPLC devices.

We have prepared three BPLC samples with following IPS electrode width (w) and gap (l): 10-10, 5-5, and 2-4 (unit: μm). The BPLC material (JC-BP01M) has a Kerr constant of ~13.7 nm/V^2 at λ=633 nm. The IPS 10-10 device exhibits a fast response time (~1 ms), high contrast ratio (~1000:1), and hysteresis ~6%. The peak transmittance depends on the individual electrode width and gap, and is in the 60-80% range [68]. We measured the VT curves for two cycles of ascending and descending voltage scans at 25^oC. The transmittance was normalized to that when the BPLC cell was in an isotropic state and the two polarizers are in parallel position. Hysteresis

is defined as the voltage difference ΔV at half-maximum transmittance between voltage-up and -down scans devided by the on-state voltage (V_{on}) as

$$H = \frac{\Delta V}{V_{on}} \tag{4.7}$$

Table 4.1 lists the measured V_{on} and hysteresis of the three IPS BPLC cells. From Table 4.1, V_{on} varies according to the *w-l* ratio. At a given voltage, a smaller electrode gap results in a stronger electric field and thus the on-state voltage is lower.

Table 4.1 IPS test cell with different electrode dimensions.

Cell	V_{on} (V)	Hysteresis	E_{max} at V_{on} (V/μm)
10-10 (25°C)	56.7	6.4%	9.65
5-5 (25°C)	50.7	10.1%	17.53
2-4 (25°C)	40.0	10%	16.95

To investigate the electric field effects on hysteresis, we simulated the electric field distribution at on-state voltage for each cell and found that the peak electric field (E_p) is located near the edge of the electrodes. Results are also included in Table 4.1. Although the 10-10 IPS cell has the highest on-state voltage (V_{on}~56.7V at 25°C), its E_p is the lowest among the three compared because of its large electrode gap. The E_p of the 5-5 and 2-4 IPS cells is almost twice as large as that of the 10-10 cell. From Table 4.1, the measured hysteresis is strongly correlated to the electric field strength. The stronger the peak electric field, the larger the hysteresis.

To further investigate the correlation between electric field and hysteresis, we did another experiment using the same BPLC material with a 10-10 IPS cell. We measured the voltage-

dependent transmittance (VT) curves at room temperature (~23°C) with a He-Ne laser (λ=633 nm). A root-mean-square voltage of 100 Hz was used to drive the cell. For the full transmittance cycle, we ascended the voltage to the peak transmittance and then descended the voltage. It is known that Kerr constant decreases as the temperature increases [36]. Therefore, at 23°C the on-state voltage occurs at V_{on}= 52.8V. A hysteresis of ~6.5% is found. We then drove the cell to the 80%, 55% and 25% of the peak transmittance with the corresponding voltage of 42.4V, 36.0V and 28.6V, respectively. Results are plotted in Figure 4.28. We notice that the hysteresis is vanished if the applied voltage is limited to 28.6V. According to the electric field distribution calculation, the peak electric field is E_p~5 V/μm, which is the critical electric field for achieving hysteresis-free operation with this polymer-stabilized BPLC (JC-BP01M). This critical field could vary depending on the polymers employed and their concentrations.

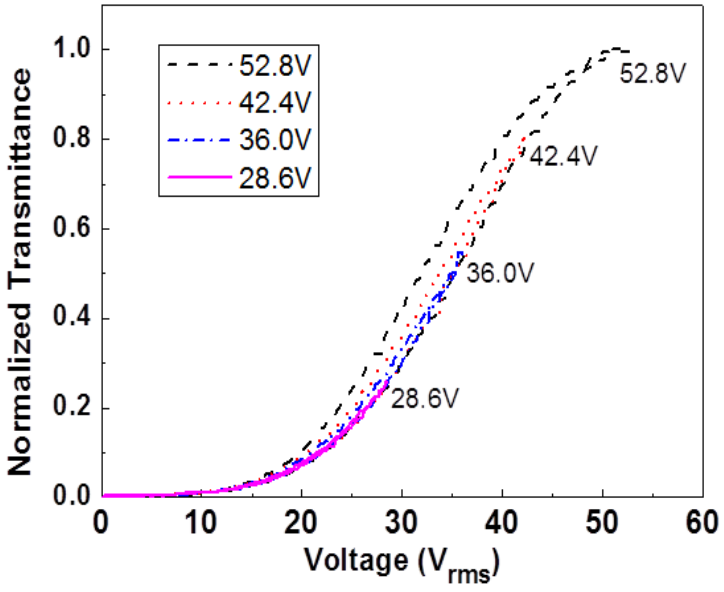

Figure 4.28 Measured hysteresis of the IPS 10-10 cell at room temperature (23°C). λ=633 nm.

As the electric field intensity increases, three distinct transformations in BPLCs could occur [69]: 1) local reorientation of molecules caused by Kerr effect: its response time is ~0.1 ms; 2) lattice distortion in BP-I: its response time is ~10 ms; and 3) phase transition to a lower-symmetry phase, i.e., switching from BP-I to BP-II: its response time is more than a few seconds. The local LC director reorientation in the double twist cylinder is the main reason for the submillisecond fast response time. However, the induced lattice distortion and phase transition by the increased electric field not only have slow response time but also cause hysteresis and ultimately irreversible structural damage. The induced lattice distortion and phase transition will induce residual birefringence. In the voltage descending process, it would lead to a higher transmittance when compared at the same voltage in the ascending process, which leads to the occurrence of the hysteresis. This coincides with our polarized optical microscope (POM) observation in Figure 4.29, the higher transmittance takes place at the edges of the electrodes where the electric field is stronger. In all, to eliminate hysteresis, the induced lattice distortion and phase transition should be avoided.

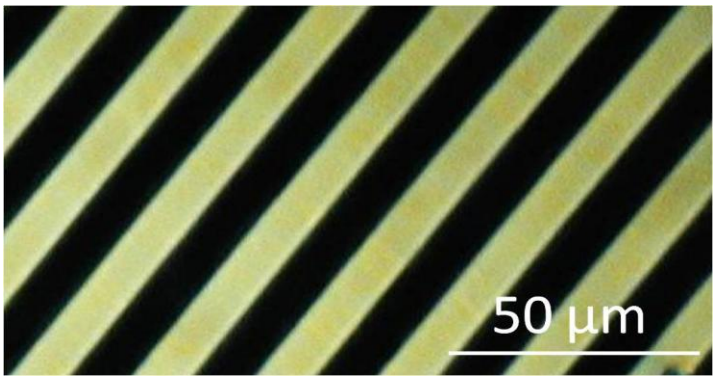

Figure 4.29 POM image of the 10-10 IPS BPLC cell at V_{on}.

From the above analysis, we should operate the device below the critical field so that the electrostriction effect will not take place. For this BPLC sample, the critical field for hysteresis-

free operation is ~5 V/μm. Once we have determined the critical field, in the following Section, we could modify the device structure, e.g., changing the protrusion shape and depth, so that the peak electric field is kept below critical field for eliminating hysteresis. Meanwhile, the transmittance and contrast ratio can be maximized.

We have compared several device structures and calculated the electric field distribution at on-state voltage with the same BPLC material used in the previous IPS test cells. For a 2-4 IPS cell, the measured on-state voltage is 40V and the peak electric field at the edge of the electrode (E_p) is 16.95 V/μm. The calculated horizontal (E_x) and vertical (E_z) electric field distributions are shown in Figure 4.30(a). When an electric field is applied, macroscopically, the blue phase LC index ellipsoid elongates along the direction of the electric field for the material with positive dielectric anisotropy. That is, the anisotropy appears with the optical axis along the field direction. The electric field has two components: E_x and E_z, but only the horizontal component contributes to the overall transmittance. We can see from Fig. 2(a) that vertical fields are strong on top of the common or pixel electrodes because electric fields are perpendicular to the electrodes, while the horizontal component (E_x) is strong in the gap area between the electrodes. The total electric field at each point is calculated as $E = \sqrt{E_x^2 + E_z^2}$. Through the calculation, the peak values for E_x, E_z and E may not be at exactly the same point, as shown in Figure 4.30, but they are all around the edges of the electrodes and are strongly related to the shape of the electrodes. If we use the 2-4 trapezoid structure with protrusion height of 2 μm in Figure 4.30(b), V_{on} is decreased to 17 V and the electric field at the edge of the electrode is substantially reduced as compared to the planar IPS structure, while the field in the gap area is still large. However, due to the sharp taper angle of the protrusion, the field is still strong, especially at the edge of the electrodes.

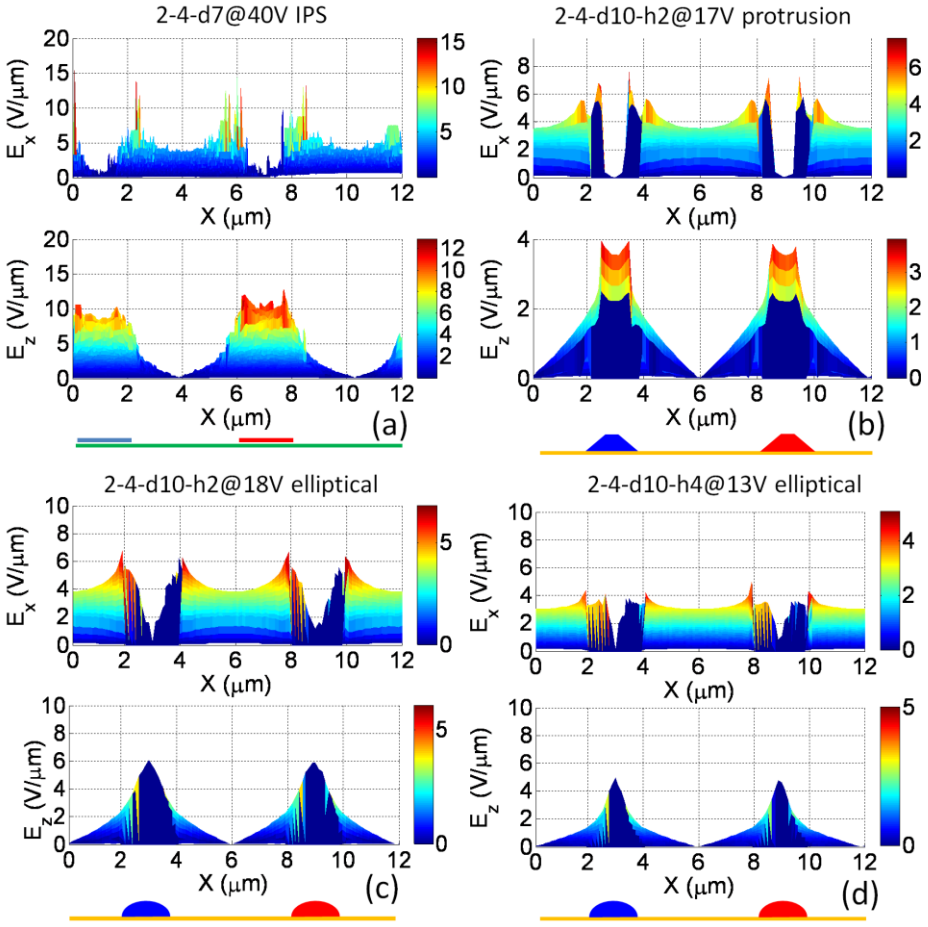

Figure 4.30 Simulated horizontal (E_x) and vertical (E_z) electric field distribution for the specified device configurations: (a) planar IPS electrode with width w=2 μm and gap l= 4 μm. Cell gap d=7 μm and V=40 V_{rms}; (b) trapezoid protrusion electrode with w=2 μm, l= 4 μm, and height h= 4 μm. Cell gap d=10 μm and V=17 V_{rms}; (c) elliptical protrusion electrode with w=2 μm, l= 4 μm, and h= 2 μm. Cell gap d=10 μm and V=18V_{rms}; and (d) elliptical protrusion electrode with w=2 μm, l= 4 μm, and h= 4 μm. Cell gap d=10 μm and V=13 V_{rms}.

To further decrease the peak electric field, we changed the trapezoid protrusion to elliptical shape, and the sharp taper angle is now smooth. From Table 4.2, the peak electric field

is reduced from 8.65 V/μm for the trapezoid protrusion to 6.85 V/μm for the elliptical protrusion. If the height of the elliptical shape electrode is increased to 4 μm, the peak field is further reduced to 5 V/μm. As depicted in Figure 4.30 with such a low peak electric field the device would be free from hysteresis.

Table 4.2 Electric field distribution for different cell configurations

Cell	V_{on} (V)	E_{x_max} (V/μm)	E_{z_max} (V/μm)	E_{max} (V/μm)
2-4 IPS (d=7μm)	40	15.53	12.92	16.95
2-4 protrusion (d=10μm, h=2μm)	17	7.68	3.97	8.65
2-4 elliptical (d=10μm, h=2μm)	18	6.84	6.09	6.85
2-4 elliptical (d=10μm, h=4μm)	13	5.08	5.00	5.08

In this section, we have explored the physical mechanism for hysteresis and found that hysteresis effect is directly related to the electric field strength generated from the electrodes. Through experiment, we also found that the critical electric field for hysteresis-free operation is ~5 V/μm. To reach this goal, we proposed an elliptical protrusion electrode structure for BPLC devices. In comparison to the planar IPS electrode structure, the protruded elliptical electrode exhibits a 3 times lower on-state voltage. Compared with trapezoid electrode, the elliptical shape is more realistic to the actual fabrication profile. Moreover, its peak electric field is weaker which is favorable for hysteresis-free device operation. The established guidelines are useful for optimizing BPLC devices in order to eliminate hysteresis while keeping high contrast ratio and maximum transmittance.

4.5 Summary

In this chapter, we have discussed various device optimization methods to improve the overall performance of blue phase liquid crystal displays. The low voltage BPLCDs are presented. The traditionally IPS structure is simple but the driving voltage is too high. The FFS structure keeps the simplicity in fabrication and provides a higher efficiency at low voltage side. The structure with double-penetrating fields lowers ~30% of the driving voltage and can be easily achieved by the etching process. The protrusion electrodes substantially lower the operating voltage; however, its fabrication complexity is increased. The structure with extra guiding fields adds to the effective region around the electrode edge area that lowers the voltage. What's more, low wavelength dispersion BPLCDs are realized by different pixel electrode designs that can generate different electric fields in RGB pixels; low color shift BPLCDs are obtained by employing zigzag electrode structure; and, low hysteresis BPLCDs are optimized by control the peak electric field to be lower than the critical fields. In all, the low voltage, low wavelength dispersion, low color shift, and low hysteresis BPLCDs can be achieved. The optimization methods from the device side will largely improve the performance of BPLCDs and can largely accelerate the emergence of blue phase LCDs.

CHAPTER 5: PHOTONICS APPLICATIONS OF BLUE PHASE LIQUID CRYSTATLS

In addition to displays, BPLCs are promising candidates for photonic applications as well. Based on the Kerr effect, birefringence can be induced according to the electric field. Therefore, blue phase liquid crystals can serve as a fast switching light modulator, such as a high efficiency tunable phase grating [70], polarization independent adaptive microlens [71], polarization independent gradient-index (GRIN) lens and cylindrical lens [72], etc.

In this chapter, the application of blue phase liquid crystal as a modulator to control the viewing angle of a liquid crystal display will be introduced. As we all know, wide viewing angle is a critical requirement for high-end LCDs. To realize wide-view, various LC modes such as in-plane switching (IPS), fringe-field switching (FFS), multi-domain vertical alignment (MVA) [73] and patterned vertical alignment (PVA) [74] have been developed. With proper phase compensation, the light leakage at oblique angles is dramatically suppressed, resulting in a wide viewing angle. In the meantime, the protection of privacy is becoming more important nowadays and thus an on-demand controllable viewing angle is highly desirable. Several approaches have already been proposed to control the viewing angle by using dual backlight system [75], or pixel division method [76].

The method we proposed of using a blue phase liquid crystal (BPLC) layer to control the viewing angle is applicable to all the LCD modes without affecting the on-state transmittance. The viewing angle can be tuned continuously with a fast response time.

As introduced before in Chapter 2, section 2.1, in blue phase, the induced birefringence (Δn) by the Kerr effect is directly proportional to the wavelength, Kerr constant, and square of the electric field amplitude. Consequently, the isotropic sphere will appear as an elongated

(Figure 2.1(b)) or a flattened (Figure 2.1(c)) ellipsoid, depending on whether the host LC has a positive or negative dielectric anisotropy ($\Delta\varepsilon$).

Therefore, the viewing angle can be tuned continuously by adjusting the applied voltage of the BPLC layer. Depicted in Figure 5.1 is the proposed device structure for the viewing angle controllable display with a BPLC layer. In Figure 5.1(a), the LCD panel is originally well-compensated and can be of any modes, such as IPS, and MVA, etc. The BPLC layer can be sandwiched above or below the initially wide-view LCD. When there is no external electric field, the BPLC cell is optically isotropic and will not affect the viewing angle of the display. With a voltage, the BPLC cell will act as an additional positive or negative C-film to disturb the well-compensated wide-view LCD. The actual viewing angle will depend on the applied voltage.

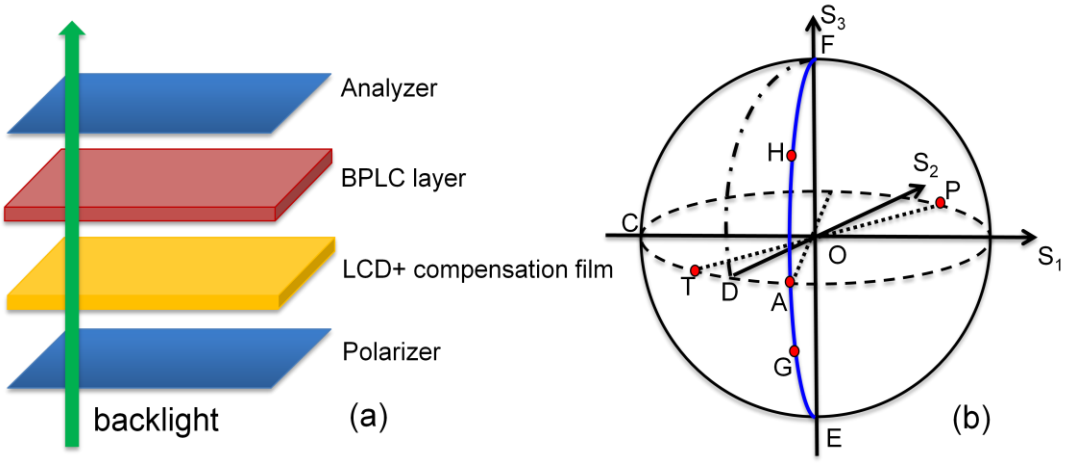

Figure 5.1 (a) Device configuration for a viewing angle controllable liquid crystal display; (b) Poincaré sphere representation.

Compared to other dual cell approaches, such as homogenous cell [77], the blue phase cell exhibits two major advantages: 1) simple fabrication: The blue phase LC cell does not require any surface alignment layer and, moreover, the electric fields are in longitudinal direction.

This can be achieved easily by planar ITO electrodes on both substrates. Such an electrode configuration is much simpler than that used in a blue phase LCD, in which lateral fields are needed and the IPS electrodes are more complicated to fabricate. 2) Blue phase LC exhibits submillisecond gray-to-gray response time, which is at least 10 times faster than the corresponding homogeneous cell.

Poincaré sphere representation is an elegant geometrical means for solving problems involving the propagation of polarized light through birefringent and optically active media [78]. The mechanism of the proposed device can be explained by the Poincaré sphere depicted in Figure 5.1(b). The unpolarized light from backlight unit passing through the bottom polarizer (point **P**) will become linearly polarized with its polarization state locating at point **T**. At oblique view, the absorption axes of polarizer (point **P**) and analyzer (point **A**) do not locate on the S_2 axis. For an uncompensated LCD panel, point **T** deviates from point **A,** but a well-compensated LC layer will then move the polarization state **T** to the absorption axis of the analyzer (point **A**), so a good dark state is achieved. When the light hits the positive $\Delta\varepsilon$ BPLC layer, it will act like a positive C-film and rotate point **A** clockwise around the CO axis to point **G**. On the other hand, if the BPLC has a negative $\Delta\varepsilon$ it will act like a negative C-film and rotate point **A** counterclockwise around the CO axis to point **H**. As a result, point **G** or **H** deviates again from the absorption axis of the analyzer (point **A**). The well-compensated wide-view LCD can be switched gradually to be narrow-view according to the voltage applied. Because the BPLC layer is an isotropic medium at V=0, so the light remains in point **A** and the good dark state will not be affected. This method works equally well for all the display modes. In addition, BPLCs have a sub-millisecond response time that enables a rapid transition between wide view and narrow view. Moreover, the fabrication of the BPLC cell is also simple because no alignment layer is needed.

To prove this concept, we conducted device simulations using a nematic IPS cell as an example. The cell parameters are listed as follows: cell gap d_{IPS}=4 μm, electrode width w=5 μm, electrode spacing l=10 μm, LC Δn=0.096 and wavelength λ=550 nm. The BPLC cell is comprised of plane ITO electrode on both substrates with a cell gap d_{BP}=5 μm. The electric field is in the longitudinal direction. The BPLC material we used has a Kerr constant K= 12.68 nm/V^2 at λ=550 nm.

Figure 5.2(a) shows the isocontrast plot for an IPS cell without any compensation film. The viewing angle is relatively poor; the 10:1 contrast ratio (CR) only extends to ~65^o polar angle. This is due to the large dark-state light leakage along the bisectors. Figure 5.2(b) is the isocontrast plot of a well-compensated IPS-LCD by a biaxial film with $d(n_x-n_y)= \lambda/2$, and N_z=0.5. The BPLC layer is optically isotropic at V=0. The CR of the well-compensated IPS-LCD is high. The display is in the wide-view mode. When the voltage is gradually increased from 0 V_{rms} (Figure 5.2(b)), 5 V_{rms} (Figure 5.2(c)), 8 V_{rms} (Figure 5.2(d)), 10 V_{rms} (Figure 5.2(e)), to 20 V_{rms} (Figure 5.2(f)), the viewing angle gets narrower. Comparing Figure 5.2(b) with Figure 5.2(f), we find that the viewing angle can go far below the original display without compensation film. However, as shown in Figure 5.2 (f), although the privacy protection is still imperfect along the horizontal and vertical directions, the region is getting smaller as the voltage increases.

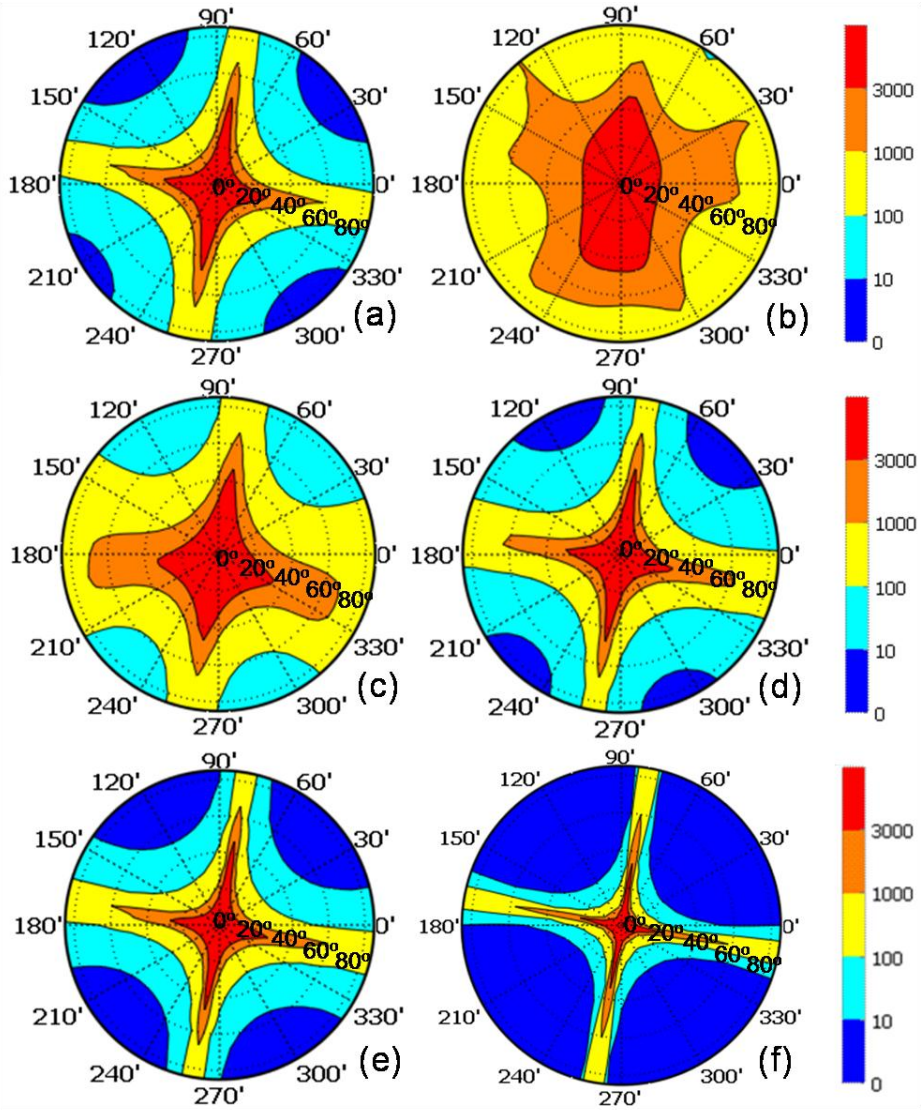

Figure 5.2 Isocontrast plots of (a) an IPS LCD without compensation film, and viewing angle controllable IPS with a biaxial film and a positive BPLC layer at (b) V=0, (c) V=5 V_{rms}, (d) V=8 V_{rms}, (e) V=10 V_{rms}, and (f) V=20 V_{rms}. λ=550 nm.

Depicted in Figure 5.3 are the isocontrast ratio plots for a viewing angle controllable display with a negative BPLC layer. This BPLC layer functions like a negative C-film. When the voltage is gradually increased from 5 V_{rms} (Figure 5.3(a)) to 8 V_{rms} (Figure 5.3(b)), 10 V_{rms} (Figure 5.3(c)) and 20 V_{rms} (Figure 5.3(d)), the polar angles for CR=100:1 decrease from 60^o to

40^o, 30^o and then 15^o. And for CR=10:1, in Figure 5.3(b), 5.3(c) and 5.3(d), the polar angles are 60^o, 50^o and 25^o. This again demonstrates the outstanding performance of the proposed viewing angle controllable displays. Besides, the symmetry of the contrast ratio contour is also remarkable.

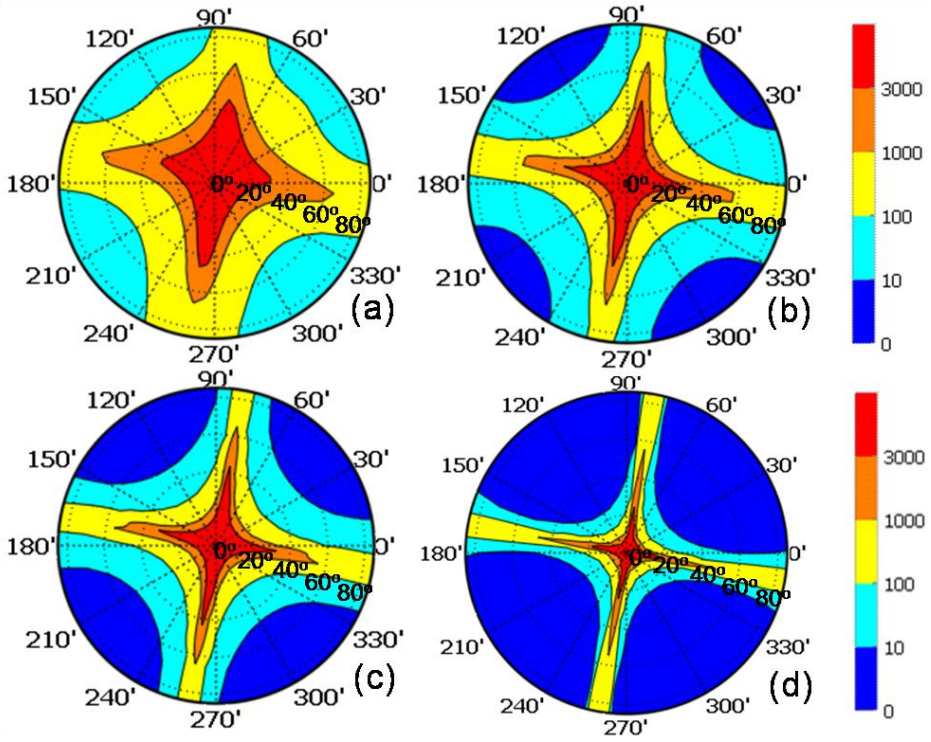

Figure 5.3 Isocontrast plots of viewing angle controllable IPS cell with a negative BPLC layer at (a) V=5 V_{rms}, (b) V=8 V_{rms}, (c) V=10 V_{rms}, and (d) V=20 V_{rms}. λ=550 nm.

According to Eq. (2.1), if we define V_{BP} as the applied voltage to BPLC layer and d_{BP} as the thickness of the BPLC layer, and if we replace the electric field E with V_{BP}/d_{BP}, we will have the following expression for the C-film like BPLC layer:

$$d_{BP}\Delta n = d_{BP}\lambda KE^2 = d_{BP}\lambda K(\frac{V_{BP}}{d_{BP}})^2 = \lambda K\frac{V_{BP}^{\ 2}}{d_{BP}} \qquad (5.1)$$

On one hand, if we keep on increasing the voltage V_{BP}, the induced birefringence will be larger and the resulted viewing angle will become narrower. Although there is saturation on the induced the birefringence, new blue phase material can always be developed to match the design requirement. On the other hand, by adjusting the thickness of the BP layer d_{BP}, the operation voltage needed to change the viewing angles can be modified. That is, a thinner BPLC cell will experience a stronger vertical electric field and thus a lower voltage is needed. To further lower the operation voltage V_{BP}, we can use a blue phase material with a larger Kerr constant K.

From Eq. (5.1), the induced birefringence can be tuned continuously by the voltage. Therefore, to obtain a specific view angel for the display, we just need to find out the induced birefringence needed, and then simply apply the corresponding voltage. The induced birefringence is uniformly distributed all over the BPLC cell, which adds to the accurateness of the control. Moreover, the overall transmittance of the original panel will not be affected by the uniform BPLC layer. A tradeoff is the increased panel thickness and weight.

Aside from the IPS example we discussed above, the proposed configuration in Figure 5.1(a) works equally well for other display modes, such as FFS, MVA and PVA, in which different compensation schemes with uniaxial or biaxial films have been proposed [79]. Therefore, as long as the LCD is initially well-compensated, the viewing angle can always be controlled by the applied voltage of the inserted BPLC layer.

In this chapter, we have demonstrated a method to control the display viewing angles using an inserted blue phase liquid crystal cell. This method works well for all the LCD panels originally compensated by uniaxial or biaxial films. The viewing angle can be tuned continuously by electronically controlling the induced birefringence of the blue phase LC layer. Moreover, the BPLC layer has a simple fabrication process without alignment layer and

submillisecond response time. The transmittance of the original LCD panel will not be affected by the BPLC cell. It is believed that this approach will have a strong potential for future display applications.

CHAPTER 6: SUMMARY

In this dissertation, we investigate blue phase liquid crystal displays based on Kerr effect. Compared to conventional nematic LCDs, the polymer-stabilized blue phase LCD exhibits several very attractive features that it does not require any alignment layer, the dark state of a blue phase LCD is optically isotropic, it is insensitive to the cell gap with IPS type electrodes, and most importantly, it demonstrates submillisecond response time. However, there are still technical challenges to overcome, such as high driving voltage, color shift issue, hysteresis issue, wavelength dispersion, long term stability, residual birefringence, and voltage holding ratio, etc. To solve these problems, material development and new device configuration are both important.

The basic properties of blue phase liquid crystals are introduced in Chapter 1, following which the electro-optic properties of BPLCs are discussed in Chapter 2. Based on Kerr effect, the optically isotropic blue phase LC can become anisotropic with the electric fields. The temperature effects are studied theoretically and experimentally. It is found that as the temperature increases, both Kerr constant, induced birefringence, and response time decrease except at different rates. The theoretical simulated relation between the on-state voltage, Kerr constant and device factor is experimental validated. Moreover, the temperature dependency on response time is validated through experiment and model. In all aspects, good agreement between experiment and physical model is found. These proposed models will undoubtedly provide the guidance to optimize the material system design and the device performances.

To further study the electro-optics and the underlying operation mechanism of the polymer-stabilized blue phase liquid crystal displays, a numerical computational model based on Kerr effect is developed. Parameters affecting the electro-optics of BPLCDs in in-plane-

switching (IPS) structures, such as electric dimension, induced birefringence, cell gap, and wavelength dispersion are investigated. In addition, we also find the origins for symmetric viewing angle of IPS BPLC structures even using a 2D electrode structure. This numerical model provides a useful tool to understand the underlying physics and optics of BPLCDs, and also to improve the performance by optimizing the display structures.

We have discussed various device optimization methods to improve the overall performance of blue phase liquid crystal displays. The high driving voltage is one of the most severe issues since it hinders the a-Si TFT driving. In Chapter 4, the low voltage BPLCDs designs are presented. The traditionally IPS structure is simple but the tradeoff is the high operating voltage which is a burden for the current a-Si TFT driving. The FFS structure keeps the simplicity in fabrication and provides a higher efficiency at low voltage side. The structure with double-penetrating fields lowers ~30% of the driving voltage and can be easily achieved by the etching process. The protrusion electrodes design substantially lower the operating voltage from 50 volts to below 10 volts; however, its fabrication complexity is increased. To further lower the voltage, the approach with extra guiding fields is proposed to enlarge the effective region around the electrode edge area. These designs can dramatically reduce the operating voltage to below 10 volts and for the first time a-Si TFT driving is enabled. Aside from low voltage designs, low wavelength dispersion BPLCDs are realized by different pixel electrode designs so that different electric fields are generated in RGB pixels; low color shift BPLCDs are obtained by employing zigzag electrode structure to create four domains; what's more, low hysteresis BPLCDs are optimized by controlling the peak electric field to be lower than the critical field. In all, the low voltage, low wavelength dispersion, low color shift, and low hysteresis BPLCDs can be achieved. The optimization methods from the device side will effectively improve the performance of

BPLCDs and can largely accelerate the emergence of blue phase LCDs.

Last but not least, blue phase liquid crystals exhibit a uniform optically isotropic to anisotropic transition with fast response time, and a simple fabrication process without alignment layer which are in favor to many photonic applications, such as phase grating and lens designs. Chapter 5 mainly focuses on the application of viewing angle controllable display by a BPLC layer. With this approach, the viewing angle can be tuned fast and continuously by electronically controlling the induced birefringence of the BPLC layer. Further research is undergoing to take advantage of the unique properties of BPLCs.

In conclusion, the fast-response blue phase liquid crystal displays are explored systematically in this dissertation. Optimizations on device configurations are conducted to improve the overall performance of the blue phase liquid crystal displays. One of the most severe issues for a-Si TFT driving is solved with low voltage blue phase liquid crystal displays. We believe this work will make an important impact to the development of blue phase LCDs.

LIST OF REFERENCES

[1] I. C. Khoo and S. T. Wu, *Optics and nonlinear optics of liquid crystals*. Singapore ; River Edge, NJ: World Scientific, 1993.

[2] P. Yeh and C. Gu, *Optics of liquid crystal displays*. New York: Wiley, 1999.

[3] P. G. d. Gennes, *The physics of liquid crystals*. Oxford Eng.: Clarendon Press, 1974.

[4] S. Chandrasekhar, *Liquid crystals*, 2nd ed. Cambridge England ; New York, NY, USA: Cambridge University Press, 1992.

[5] D. K. Yang and S. T. Wu, *Fundamentals of liquid crystal devices*. Hoboken, NJ: John Wiley, 2006.

[6] J. Goodby, "The Nanoscale Engineering of Nematic Liquid Crystals for Displays," *Liquid Crystals,* vol. 38, 1363–1387, 2011.

[7] W. Helfrich and M. Schadt, "Birefringence of Nematogenic Liquids Caused by Electrical Conduction," *Physical Review Letters,* vol. 27, 561-564, 1971.

[8] M. Schadt and W. Helfrich, "Voltage-Dependent Optical Activity of a Twisted Nematic Liquid Crystal," *Applied Physics Letters,* vol. 18, 127-128, 1971.

[9] T. J. Scheffer and J. Nehring, "A New, Highly Multiplexable Liquid-Crystal Display," *Applied Physics Letters,* vol. 45, 1021-1023, 1984.

[10] R. A. Soref, "Transverse Field Effects in Nematic Liquid-Crystals," *Applied Physics Letters,* vol. 22, 165-166, 1973.

[11] M. F. Schiekel and K. Fahrensc, "Deformation of Nematic Liquid Crystals with Vertical Orientation in Electrical Fields," *Applied Physics Letters,* vol. 19, 391-393, 1971.

[12] H. Hasebe and S. Kobayashi, "A Full-Color Field Sequential LCD Using Modulated Backlight," *SID Int. Symp. Digest Tech. Papers*, vol. 16, 81-84, 1985.

[13] F. Yamada, *et al.*, "Sequential-Color LCD Based on OCB with an LED Backlight," *Journal of the Society for Information Display,* vol. 10, 81-85, 2002.

[14] S. Gauza, *et al.*, "Fast Switching Liquid Crystals for Color-Sequential LCDs," *Journal of Display Technology,* vol. 3, 250-252, 2007.

[15] F. C. Lin, *et al.*, "Color-Breakup Suppression and Low-Power Consumption by Using the Stencil-FSC Method in Field-Sequential LCDs," *Journal of the Society for Information*

Display, vol. 17, 221-228, 2009.

[16] S. T. Wu and U. Efron, "Optical-Properties of Thin Nematic Liquid-Crystal Cells," *Applied Physics Letters,* vol. 48, 624-626, 1986.

[17] M. Z. Jiao, *et al.*, "Alignment Layer Effects on Thin Liquid Crystal Cells," *Applied Physics Letters,* vol. 92, 061102, 2008.

[18] S. T. Wu and C. S. Wu, "High-Speed Liquid-Crystal Modulators Using Transient Nematic Effect," *Journal of Applied Physics,* vol. 65, 527-532, 1989.

[19] S. T. Wu, "Nematic Liquid-Crystal Modulator with Response-Time Less Than 100 μs at Room Temperature," *Applied Physics Letters,* vol. 57, 986-988, 1990.

[20] P. J. Bos and K. R. Beran, "The Pi-Cell, A Fast Liquid-Crystal Optical-Switching Device," *Molecular Crystals and Liquid Crystals,* vol. 113, 329-339, 1984.

[21] T. Miyashita, *et al.*, "Wide-Viewing-Angle Display Mode Using Bend-Alignment Liquid-Crystal Cell," *Japanese Journal of Applied Physics Part 2-Letters,* vol. 34, L177-L179, 1995.

[22] F. S. Yeung, *et al.*, "Pi-cell Liquid Crystal Displays at Arbitrary Pretilt Angles," *Applied Physics Letters,* vol. 88, 041108, 2006.

[23] M. Schadt, "Liquid Crystal Materials and Liquid Crystal Displays," *Annu. Rev. Mater. Sci.,* vol. 27, 305-379, 1997.

[24] L. H. Rao, *et al.*, "Emerging Liquid Crystal Displays Based on the Kerr Effect," *Molecular Crystals and Liquid Crystals,* vol. 527, 30-42, 2010.

[25] P. P. Crooker, "Blue Phases," in *Chirality in liquid crystals*, H. S. Kitzerow and C. Bahr, Eds., New York: Springer, 2001.

[26] Y. Chen, *et al.*, "A Microsecond-Response Polymer-Stabilized Blue Phase Liquid Crystal," *Applied Physics Letters,* vol. 99, 201105, 2011.

[27] S. Meiboom, *et al.*, "Theory of the Blue Phase of Cholesteric Liquid-Crystals," *Physical Review Letters,* vol. 46, 1216-1219, 1981.

[28] H. Kikuchi, *et al.*, "Polymer-Stabilized Liquid Crystal Blue Phases," *Nature Materials,* vol. 1, 64-68, 2002.

[29] H. Kikuchi, "Liquid Crystalline Blue Phases," *Liquid Crystalline Functional Assemblies and Their Supramolecular Structures,* vol. 128, 99-117, 2008.

[30] J. Yan and S. T. Wu, "Polymer-Stabilized Blue Phase Liquid Crystals: A Tutorial," *Optical Materials Express,* vol. 1, 1527-1535, 2011.

[31] J. Kerr, "A New Relation between Electricity and Light: Dielectrified Media Birefringent," *Philos. Mag.,* vol. 50, 337-348, 1875.

[32] L. H. Rao, *et al.,* "Viewing Angle Controllable Displays with A Blue-Phase Liquid Crystal Cell," *Optics Express,* vol. 18, 3143-3148, 2010.

[33] J. Yan, *et al.,* "Extended Kerr Effect of Polymer-Stabilized Blue Phase Liquid Crystals," *Applied Physics Letters,* vol. 96, 071105, 2010.

[34] H. Kikuchi, *et al.,* "Optically Isotropic Nano-Structured Liquid Crystal Composites for Display Applications," *SID Int. Symp. Digest Tech. Papers,* vol. 40, 578-581, 2009.

[35] Y. Haseba, *et al.,* "Large Electro-Optic Kerr Effect in Nanostructured Chiral Liquid-Crystal Composites over A Wide Temperature Range," *Advanced Materials,* vol. 17, 2311-2315, 2005.

[36] L. H. Rao, *et al.,* "Prospects of Emerging Polymer-Stabilized Blue-Phase Liquid-Crystal Displays," *Journal of the Society for Information Display,* vol. 18, 954-959, 2010.

[37] Y. H. Fan, *et al.,* "Fast-Response and Scattering-Free Polymer Network Liquid Crystals for Infrared Light Modulators," *Applied Physics Letters,* vol. 84, 1233-1235, 2004.

[38] P. R. Gerber, "Electro-Optical Effects of A Small-Pitch Blue-Phase System," *Molecular Crystals and Liquid Crystals,* vol. 116, 197-206, 1985.

[39] S. T. Wu, "Birefringence Dispersions of Liquid-Crystals," *Physical Review A,* vol. 33, 1270-1274, 1986.

[40] W. Maier and A. Saupe, "Eine Einfache Molecular-Statistische Theorie Der Nematischen Kristallinflüssigen phase," *Z. Naturforsch, Teil A,* vol. 15, 287–292, 1960.

[41] F. Zhang and D. K. Yang, "Temperature Dependence of Pitch and Twist Elastic Constant in a Cholesteric to Smectic A Phase Transition," *Liquid Crystals,* vol. 29, 1497-1501, 2002.

[42] W. M. Gelbart and A. Benshaul, "Molecular Theory of Curvature Elasticity in Nematic Liquids," *Journal of Chemical Physics,* vol. 77, 916-933, 1982.

[43] L. H. Rao, *et al.,* "Low Temperature Effects on the Response Time of Liquid Crystal Displays," *Applied Physics Letters,* vol. 94, 071112, 2009.

[44] I. Haller, "Thermodynamic and Static Properties of Liquid Crystals," *Progress in Solid State Chemistry,* vol. 10, 103-118, 1975.

[45] S. T. Wu, *et al.,* "Optimal Operation Temperature of Liquid-Crystal Modulators," *Applied Optics,* vol. 26, 3441-3445, 1987.

[46] J. Li, *et al.*, "Temperature Effect on Liquid Crystal Refractive Indices," *Journal of Applied Physics,* vol. 96, 19-24, 2004.

[47] L. H. Rao, *et al.*, "A Large Kerr Constant Polymer-Stabilized Blue phase Liquid Crystal," *Applied Physics Letters,* vol. 98, 081109, 2011.

[48] K. M. Chen, *et al.*, "Submillisecond Gray-Level Response Time of a Polymer-Stabilized Blue-Phase Liquid Crystal," *Journal of Display Technology,* vol. 6, 49-51, 2010.

[49] H. F. Gleeson and H. J. Coles, "Dynamic Properties of Blue-Phase Mixtures," *Liquid Crystals,* vol. 5, 917-926, 1989.

[50] S. T. Wu and C. S. Wu, "Experimental Confirmation of the Osipov-Terentjev Theory on the Viscosity of Nematic Liquid-Crystals," *Physical Review A,* vol. 42, 2219-2227, 1990.

[51] S. T. Wu and C. S. Wu, "Rotational Viscosity of Nematic Liquid Crystals: a Critical Examination of Existing Models," *Liquid Crystals,* vol. 8, 171-182, 1990.

[52] M. Schadt and F. Muller, "Physical Properties of New Liquid Crystal Mixtures and Electrooptical Performance in Twisted Nematic Displays," *IEEE Transactions on Electron Devices,* vol. 25, 1125-1137, 1978.

[53] Z. B. Ge, *et al.*, "Modeling of Blue Phase Liquid Crystal Displays," *Journal of Display Technology,* vol. 5, 250-256, 2009.

[54] Z. B. Ge, *et al.*, "Electro-Optics of Polymer-Stabilized Blue Phase Liquid Crystal Displays," *Applied Physics Letters,* vol. 94, 101104, 2009.

[55] S. H. Lee, *et al.*, "Electro-Optic Characteristics and Switching Principle of A Nematic Liquid Crystal Cell Controlled by Fringe-Field Switching," *Applied Physics Letters,* vol. 73, 2881-2883, 1998.

[56] Z. B. Ge, *et al.*, "Reflective Liquid-Crystal Displays with Asymmetric Incident and Exit Angles," *Journal of the Optical Society of America A-Optics Image Science and Vision,* vol. 22, 966-977, 2005.

[57] S. T. Wu, *et al.*, "Refractive-Index Dispersions of Liquid-Crystals," *Optical Engineering,* vol. 32, 1775-1780, 1993.

[58] Z. B. Ge, *et al.*, "Thin Cell f Fringe-Field-Switching Liquid Crystal Display with A Chiral Dopant," *Applied Physics Letters,* vol. 92, 181109, 2008.

[59] L. H. Rao, *et al.*, "Zigzag Electrodes for Suppressing the Color Shift of Kerr Effect-Based Liquid Crystal Displays," *Journal of Display Technology,* vol. 6, 115-120, 2010.

[60] M. Z. Jiao, *et al.*, "Low Voltage and High Transmittance Blue-Phase Liquid Crystal Displays with Corrugated Electrodes," *Applied Physics Letters,* vol. 96, 011102, 2010.

[61] M. Kim, *et al.*, "Wall-Shaped Electrodes for Reducing the Operation Voltage of Polymer-Stabilized Blue Phase Liquid Crystal Displays," *Journal of Physics D-Applied Physics*, vol. 42, 235502, 2009.

[62] L. H. Rao, *et al.*, "Low Voltage Blue-Phase LCDs with Double-Penetrating Fringe Fields," *Journal of Display Technology*, vol. 6, 287-289, 2010.

[63] X. Y. Zhu, *et al.*, "Analytical Solutions for Uniaxial-Film-Compensated Wide-View Liquid Crystal Displays," *Journal of Display Technology*, vol. 2, 312-312, 2006.

[64] D. Kubota, *et al.*, "A New Process for Manufacture of Low Voltage, Polymer-Stabilized Blue Phase LCDs," *SID Int. Symp. Digest Tech. Papers*, vol. 42, 125-128, 2011.

[65] H. Lee, *et al.*, "The World's First Blue Phase Liquid Crystal Display ", *SID Int. Symp. Digest Tech. Papers*, vol. 42, 121-124, 2011.

[66] R. B. Lu, *et al.*, "Bending Angle Effects on the Multi-Domain In-Plane-Switching Liquid Crystal Displays," *Journal of Display Technology*, vol. 1, 207-216, 2005.

[67] J. Yan and S. T. Wu, "Effect of Polymer Concentration and Composition on Blue Phase Liquid Crystals," *Journal of Display Technology*, vol. 7, 490-493, 2011.

[68] K. M. Chen, *et al.*, "Electrode Dimension Effects on Blue-Phase Liquid Crystal Displays," *Journal of Display Technology*, vol. 7, 362-364, 2011.

[69] H. S. Kitzerow, "The Effect of Electric Fields on Blue Phases," *Molecular Crystals and Liquid Crystals*, vol. 202, 51-83, 1991.

[70] J. Yan, *et al.*, "High-Efficiency and Fast-Response Tunable Phase Grating Using A Blue Phase Liquid Crystal," *Optics Letters*, vol. 36, 1404-1406, 2011.

[71] Y. Li and S. T. Wu, "Polarization Independent Adaptive Microlens With A Blue-Phase Liquid Crystal," *Optics Express*, vol. 19, 8045-8050, 2011.

[72] Y. Li, *et al.*, "Polarization Independent Blue-Phase Liquid Crystal Cylindrical Lens with A Resistive Film," *Applied Optics*, vol. 51, 2568-2572, 2012.

[73] A. Takeda, *et al.*, "A Super-High Image Quality Multi-Domain Vertical Alignment LCD by New Rubbing-Less Technology," *SID Int. Symp. Digest Tech. Papers*, vol. 29, 1077-1080, 1998.

[74] K. H. Kim, *et al.*, "Domain Divided Vertical Alignment Mode with Optimized Fringe Field Effect," *Proc. 18th Int'l Display Research Conference*, 383-386, 1998.

[75] K. W. Chien, *et al.*, "Dual Light Source For Backlight Systems For Smart Viewing-Adjustable LCDs," *SID Int. Symp. Digest Tech. Papers*, vol. 37, 1425-1427, 2006.

[76] K. Takatoh, *et al.*, "New Peeping Prevention Technology To Control Viewing Angle Properties of TFT-LCDs," *SID Int. Symp. Digest Tech. Papers*, vol. 37, 1340-1343, 2006.

[77] E. Jeong, *et al.*, "Viewing Angle Switching of Vertical Alignment Liquid Crystal Displays by Controlling Birefringence of Homogenously Aligned Liquid Crystal Layer," *Applied Physics Letters*, vol. 90, 051116, 2007.

[78] J. E. Bigelow and R. A. Kashnow, "Poincare Sphere Analysis of Liquid-Crystal Optics," *Applied Optics*, vol. 16, 2090-2096, 1977.

[79] X. Y. Zhu, *et al.*, "Analytical Solutions for Uniaxial-Film-Compensated Wide-View Liquid Crystal Displays," *Journal of Display Technology*, vol. 2, 2-20, 2006.

LIST OF STUDENT'S PUBLICATIONS

JOURNAL PUBLICATIONS:

1. Y. Liu, H. Ren, S. Xu, Y. Chen, L. Rao, T. Ishinabe, and S. T. Wu, "Adaptive focus integral image system design based on Fast-response liquid crystal microlens," IEEE/OSA J. Display Technol. **7**, 674-678 (Dec. 2011).

2. L. Rao, J. Yan, S. T. Wu, Y. H. Chiu, H. Y. Chen, C. C. Liang, C. M. Wu, P. J. Hsieh, S. H. Liu, and K. L. Cheng, "Critical field for a hysteresis-free BPLC device," IEEE/OSA J. Display Technol. **7**, 627-629 (Dec. 2011).

3. J. Yan, L. Rao, M. Jiao, Y. Li, H. C. Cheng, and S. T. Wu, "Polymer-stabilized optically isotropic liquid crystals for next-generation display and photonics applications," J. Materials Chem. **21**, 7870-7877 (Mar. 2011).

4. L. Rao, J. Yan, and S. T. Wu, "A large Kerr constant polymer-stabilized blue phase liquid crystal," Appl. Phys. Lett. **98**, 081109(Feb. 2011).

5. L. Rao, J. Yan, and S. T. Wu, "Prospects of emerging polymer-stabilized blue-phase liquid crystal displays," J. Soc. Info. Disp. **18**, 954-959 (Nov. 2010).

6. L. Rao, H. C. Cheng, and S. T. Wu, "Low Voltage Blue-Phase LCDs with Double-Penetrating Fringe Fields," IEEE/OSA J. Display Technol. **6**, issue 8, 287-289 (Aug. 2010).

7. L. Rao, Z. Ge, S. Gauza, K. M Chen, and S. T. Wu, "Emerging liquid crystal displays based on the Kerr effect," Mol. Cryst. Liq. Cryst. **526**, 185–197 (Jul. 2010).

8. J. Yan, M. Jiao, L. Rao, and S. T. Wu, "Direct measurement of electric-field-induced birefringence in a polymer-stabilized blue-phase liquid crystal composite," Optics Express **18**, 11450-11455 (May. 2010).

9. H. C. Cheng, L. Rao, and S. T. Wu, "Color Breakup Suppression in Field-Sequential Five-Primary-Color LCDs," IEEE/OSA J. Display Technol. **6**, 229-234 (Apr. 2010).

10. L. Rao, Z. Ge, and S. T. Wu, "Zigzag electrodes for suppressing the color shift of Kerr effect-based Liquid Crystal Displays," IEEE/OSA J. Display Technol. **6**, issue 4, 115-120 (Apr. 2010).

11. S. Yoon, M. Kim, M. S. Kim, B. G. Kang, M. K. Kim, A. K. Srivastava, S. H. Lee, Z. Ge, L. Rao, S. Gauza, and S. T. Wu, "Optimization of Electrode Structure to Improve the Electro-Optic Characteristics of Liquid Crystal Display Based on Kerr Effect," Liq. Cryst. **37**, 201-208 (Feb. 2010).

12. L. Rao, Z. Ge, and S. T. Wu, "Viewing angle controllable displays with a blue-phase liquid crystal cell," Opt. Express **18**, 3143-3148 (Feb. 2010).

13. J. Yan, H. C. Cheng, S. Gauza, Y. Li, M. Jiao, L. Rao, and S. T. Wu, "Extended Kerr effect in polymer-stabilized blue-phase liquid crystals," Appl. Phys. Lett. **96**, 071105. (Feb. 2010)

14. L. Rao, Z. Ge, S. T. Wu, and S. H. Lee, "Low driving voltage blue phase liquid crystal displays," Appl. Phys. Lett. **95**, 231101 (Dec. 2009).

15. M. Kim, M. S. Kim, B. G. Kang, M. K. Kim, S. Yoon, S. H. Lee, Z. Ge, L. Rao, S. Gauza and S. T. Wu, "Wall-shaped electrodes for reducing the operation voltage of polymer-stabilized blue phase liquid crystal displays," J. Phys. D: Appl. Phys. **42**, 235502 (Nov. 2009).

16. Z. Ge, L. Rao, S. Gauza, and S. T. Wu, "Modeling of blue phase liquid crystal displays," IEEE/OSA J. Display Technology **5**, 250-256 (Jul. 2009).

17. L. Rao, S. Gauza, and S. T. Wu, "Low temperature effects on the response time of liquid crystal displays," Appl. Phys. Lett. **94**, 071112 (Feb. 2009).

CONFERENCE PROCEEDINGS:

1. L. Rao, J. Yan, S. T. Wu, S. Yamamoto, and Y. Haseba, "Hysteresis-free blue-phase LCDs," SID Int. Symp. Digest Tech. Papers, vol. 43, 199-200, 2012.

2. L. Rao, J. Yan, and S. T. Wu "Temperature effect on polymer-stabilized blue-phase LCDs," SID Int. Symp. Digest Tech. Papers, vol. 42, 129-131, 2011.

3. L. Rao, Z. Ge, and S. T. Wu "Emerging blue phase liquid crystal displays," SPIE Optics + Photonics: Liquid Crystals XIV, Proc. of SPIE, vol. 7775, 77750Y, 2010. *(Invited Talk)*

4. L. Rao, Z. Ge, and S. T. Wu, "Low voltage blue phase LCDs with patterned electrodes," SID Int. Symp. Digest Tech. Papers, vol. 41, 77-79, 2010. *(Distinguished Student Paper Award)*

5. L. Rao, Z. Ge and S. T. Wu, "Viewing angle controllable displays using a blue phase liquid crystal cell," SID Int. Symp. Digest Tech. Papers, vol. 41, 177-179, 2010.

6. L. Rao, S. Gauza, S. T. Wu and X. Liang, "Low-temperature effect on the liquid-crystal response time of mobile displays," SID Int. Symp. Digest Tech. Papers, vol. 40, 1000-1002, 2009.

7. J. Yan, M. Jiao, L. Rao, and S. T. Wu, "Recent advances in optically isotropic liquid crystals for emerging display applications," SPIE Photonics West, Proc. of SPIE, vol. 7955, 79550F, 2011. *(Invited paper)*

8. J. Yan, H. C. Cheng, S. Gauza, Y. Li, M. Jiao, L. Rao, and S. T. Wu, "Extended Kerr effect in a polymer-stabilized blue-phase liquid crystal composite," SID Int. Symp. Digest Tech. Papers, vol. 41, 87-89, 2010.

MAGAZINE PUBLICATIONS:

1. L. Rao, Z. Ge, S. Gauza, K. M. Chen, S. T. Wu and S. H. Lee, "Emerging LCDs based on the Kerr effect," Information Display, 14-18, Nov. 2009

US PATENTS PENDING:

1. S. Gauza, S. T. Wu, Z. Ge, L. Rao, H. K. Hsu, and C. L. Chin, "Liquid crystals composition and liquid crystal display with patterned electrodes," U.S. patent application pending, Pub. No.: US 2011/0075074 A1 (Sep. 2009).